Combined performance studies for electrons at the 2004 ATLAS combined test-beam

2010 JINST 5 P11006

(http://iopscience.iop.org/1748-0221/5/11/P11006)

PUBLISHED BY IOP PUBLISHING FOR SISSA

RECEIVED: *September 6, 2010*
ACCEPTED: *November 1, 2010*
PUBLISHED: *November 25, 2010*

Combined performance studies for electrons at the 2004 ATLAS combined test-beam

E. Abat,[k,1] **J.M. Abdallah,**[f] **T.N. Addy,**[ag] **P. Adragna,**[cc] **M. Aharrouche,**[ba] **A. Ahmad,**[cm,2] **T.P.A. Akesson,**[ay] **M. Aleksa,**[s] **C. Alexa,**[n] **K. Anderson,**[t] **A. Andreazza,**[be,bf] **F. Anghinolfi,**[s] **A. Antonaki,**[e] **G. Arabidze,**[e] **E. Arik,**[k] **T. Atkinson,**[bd] **J. Baines,**[cf] **O.K. Baker,**[dd] **D. Banfi,**[be,bf] **S. Baron,**[s] **A.J. Barr,**[bs] **R. Beccherle,**[aj] **H.P. Beck,**[i] **B. Belhorma,**[aw] **P.J. Bell,**[bb,3] **D. Benchekroun,**[q] **D.P. Benjamin,**[ac] **K. Benslama,**[cg] **E. Bergeaas Kuutmann,**[cp,4] **J. Bernabeu,**[cz] **H. Bertelsen,**[v] **S. Binet,**[bq] **C. Biscarat,**[ad] **V. Boldea,**[n] **V.G. Bondarenko,**[bk] **M. Boonekamp,**[cj] **M. Bosman,**[f] **C. Bourdarios,**[bq] **Z. Broklova,**[ca] **D. Burckhart Chromek,**[s] **V. Bychkov,**[an] **J. Callahan,**[ai] **D. Calvet,**[u] **M. Canneri,**[bw] **M. Capeáns Garrido,**[s] **M. Caprini,**[n] **L. Cardiel Sas,**[s] **T. Carli,**[s] **L. Carminati,**[be,bf] **J. Carvalho,**[p,by] **M. Cascella,**[bw] **M.V. Castillo,**[cz] **A. Catinaccio,**[s] **D. Cauz,**[ak] **D. Cavalli,**[be] **M. Cavalli Sforza,**[f] **V. Cavasinni,**[bw] **S.A. Cetin,**[k] **H. Chen,**[j] **R. Cherkaoui,**[cd] **L. Chevalier,**[cj] **F. Chevallier,**[aw] **S. Chouridou,**[cx] **M. Ciobotaru,**[cv] **M. Citterio,**[be] **A. Clark,**[ae] **B. Cleland,**[bx] **M. Cobal,**[ak] **E. Cogneras,**[i] **P. Conde Muino,**[by] **M. Consonni,**[be,bf] **S. Constantinescu,**[n] **T. Cornelissen,**[s,5] **S. Correard,**[w] **A. Corso Radu,**[s] **G. Costa,**[be] **M.J. Costa,**[cz] **D. Costanzo,**[cl] **S. Cuneo,**[aj] **P. Cwetanski,**[ai] **D. Da Silva,**[ch] **M. Dam,**[v] **M. Dameri,**[aj] **H.O. Danielsson,**[s] **D. Dannheim,**[s] **G. Darbo,**[aj] **T. Davidek,**[ca] **K. De,**[d] **P.O. Defay,**[u] **B. Dekhissi,**[ax] **J. Del Peso,**[az] **T. Del Prete,**[bw] **M. Delmastro,**[s] **F. Derue,**[av] **L. Di Ciaccio,**[ar] **B. Di Girolamo,**[s] **S. Dita,**[n] **F. Dittus,**[s] **F. Djama,**[w] **T. Djobava,**[cs] **D. Dobos,**[aa,6] **M. Dobson,**[s] **B.A. Dolgoshein,**[bk] **A. Dotti,**[bw] **G. Drake,**[b] **Z. Drasal,**[ca] **N. Dressnandt,**[bu] **C. Driouchi,**[v] **J. Drohan,**[cw] **W.L. Ebenstein,**[ac] **P. Eerola,**[ay,7] **I. Efthymiopoulos,**[s] **K. Egorov,**[ai] **T.F. Eifert,**[s] **K. Einsweiler,**[h] **M. El Kacimi,**[as] **M. Elsing,**[s] **D. Emelyanov,**[cf,8] **C. Escobar,**[cz] **A.I. Etienvre,**[cj] **A. Fabich,**[s]

[1] Deceased
[2] Now at SUNY, Stony Brook, United States of America
[3] Now at Université de Genève, Switzerland
[4] Now at DESY, Zeuthen, Germany
[5] Now at INFN Genova and Università di Genova, Italy
[6] Now at CERN
[7] Now at University of Helsinki, Finland
[8] Now at Joint Institute for Nuclear Research, Dubna, Russia

doi:10.1088/1748-0221/5/11/P11006

2010 JINST 5 P11006

K. Facius,[v] **A.I. Fakhr-Edine,**[o] **M. Fanti,**[be,bf] **A. Farbin,**[d] **P. Farthouat,**[s]
D. Fassouliotis,[e] **L. Fayard,**[bq] **R. Febbraro,**[u] **O.L. Fedin,**[bv] **A. Fenyuk,**[cb]
D. Fergusson,[h] **P. Ferrari,**[s,9] **R. Ferrari,**[bt] **B.C. Ferreira,**[ch] **A. Ferrer,**[cz] **D. Ferrere,**[ae]
G. Filippini,[u] **T. Flick,**[dc] **D. Fournier,**[bq] **P. Francavilla,**[bw] **D. Francis,**[s] **R. Froeschl,**[s,10]
D. Froidevaux,[s] **E. Fullana,**[b] **S. Gadomski,**[ae] **G. Gagliardi,**[aj] **P. Gagnon,**[ai] **M. Gallas,**[s]
B.J. Gallop,[cf] **S. Gameiro,**[s] **K.K. Gan,**[bp] **R. Garcia,**[az] **C. Garcia,**[cz] **I.L. Gavrilenko,**[bj]
C. Gemme,[aj] **P. Gerlach,**[dc] **N. Ghodbane,**[u] **V. Giakoumopoulou,**[e] **V. Giangiobbe,**[bw]
N. Giokaris,[e] **G. Glonti,**[an] **T. Goettfert,**[bm] **T. Golling,**[h,11] **N. Gollub,**[s] **A. Gomes,**[at,au,by]
M.D. Gomez,[ae] **S. Gonzalez-Sevilla,**[cz,12] **M.J. Goodrick,**[r] **G. Gorfine,**[bo] **B. Gorini,**[s]
D. Goujdami,[o] **K-J. Grahn,**[aq] **P. Grenier,**[u,13] **N. Grigalashvili,**[an] **Y. Grishkevich,**[bl]
J. Grosse-Knetter,[l,14] **M. Gruwe,**[s] **C. Guicheney,**[u] **A. Gupta,**[t] **C. Haeberli,**[i]
R. Haertel,[bm,15] **Z. Hajduk,**[y] **H. Hakobyan,**[de] **M. Hance,**[bu] **J.D. Hansen,**[v] **P.H. Hansen,**[v]
K. Hara,[cu] **A. Harvey Jr.,**[ag] **R.J. Hawkings,**[s] **F.E.W. Heinemann,**[bs]
A. Henriques Correia,[s] **T. Henss,**[dc] **L. Hervas,**[s] **E. Higon,**[cz] **J.C. Hill,**[r] **J. Hoffman,**[z]
J.Y. Hostachy,[aw] **I. Hruska,**[ca] **F. Hubaut,**[w] **F. Huegging,**[l] **W. Hulsbergen,**[s,16]
M. Hurwitz,[t] **L. Iconomidou-Fayard,**[bq] **E. Jansen,**[ce] **I. Jen-La Plante,**[t]
P.D.C. Johansson,[cl] **K. Jon-And,**[cp] **M. Joos,**[s] **S. Jorgensen,**[f] **J. Joseph,**[h]
A. Kaczmarska,[y,17] **M. Kado,**[bq] **A. Karyukhin,**[cb] **M. Kataoka,**[s,18] **F. Kayumov,**[bj]
A. Kazarov,[bv] **P.T. Keener,**[bu] **G.D. Kekelidze,**[an] **N. Kerschen,**[cl] **S. Kersten,**[dc]
A. Khomich,[bc] **G. Khoriauli,**[an] **E. Khramov,**[an] **A. Khristachev,**[bv] **J. Khubua,**[an]
T.H. Kittelmann,[v,19] **R. Klingenberg,**[aa] **E.B. Klinkby,**[ac] **P. Kodys,**[ca] **T. Koffas,**[s]
S. Kolos,[cv] **S.P. Konovalov,**[bj] **N. Konstantinidis,**[cw] **S. Kopikov,**[cb] **I. Korolkov,**[f]
V. Kostyukhin,[aj,20] **S. Kovalenko,**[bv] **T.Z. Kowalski,**[x] **K. Krüger,**[s,21] **V. Kramarenko,**[bl]
L.G. Kudin,[bv] **Y. Kulchitsky,**[bi] **C. Lacasta,**[cz] **R. Lafaye,**[ar] **B. Laforge,**[av] **W. Lampl,**[c]
F. Lanni,[j] **S. Laplace,**[ar] **T. Lari,**[be] **A-C. Le Bihan,**[s,22] **M. Lechowski,**[bq]
F. Ledroit-Guillon,[aw] **G. Lehmann,**[s] **R. Leitner,**[ca] **D. Lelas,**[bq] **C.G. Lester,**[r] **Z. Liang,**[z]
P. Lichard,[s] **W. Liebig,**[bo] **A. Lipniacka,**[g] **M. Lokajicek,**[bz] **L. Louchard,**[u] **K.F. Lourerio,**[bp]
A. Lucotte,[aw] **F. Luehring,**[ai] **B. Lund-Jensen,**[aq] **B. Lundberg,**[ay] **H. Ma,**[j]

[9]Now at Nikhef National Institute for Subatomic Physics, Amsterdam, Netherlands
[10]Corresponding author, robert.froeschl@cern.ch
[11]Now at Yale University, New Haven, U.S.A.
[12]Now at Université de Genève, Switzerland
[13]Now at SLAC, Stanford, U.S.A.
[14]Now at Georg-August-Universitaet, Goettingen, Germany
[15]Now at Versicherungskammer Bayern, Munich, Germany
[16]Now at Nikhef National Institute for Subatomic Physics, Amsterdam, Netherlands
[17]Now at Université Pierre et Marie Curie (Paris 6) and Université Denis Diderot (Paris-7), France
[18]Now at Laboratoire de Physique de Particules (LAPP), Annecy-le-Vieux, France
[19]Now at University of Pittsburgh, U.S.A.
[20]Now at Physikalisches Institut der Universitaet Bonn, Germany
[21]Now at Universität Heidelberg, Germany
[22]Now at IPHC, Universit'e de Strasbourg, CNRS/IN2P3, Strasbourg, France

2010 JINST 5 P11006

R. Mackeprang,[v] A. Maio,[at,au,by] V.P. Maleev,[bv] F. Malek,[aw] L. Mandelli,[be] J. Maneira,[by] M. Mangin-Brinet,[ae,23] A. Manousakis,[e] L. Mapelli,[s] C. Marques,[by] S.Marti i Garcia,[cz] F. Martin,[bu] M. Mathes,[l] M. Mazzanti,[be] K.W. McFarlane,[ag] R. McPherson,[da] G. Mchedlidze,[cs] S. Mehlhase,[ah] C. Meirosu,[s] Z. Meng,[ck] C. Meroni,[be] V. Mialkovski,[an] B. Mikulec,[ae,24] D. Milstead,[cp] I. Minashvili,[an] B. Mindur,[x] V.A. Mitsou,[cz] S. Moed,[ae,25] E. Monnier,[w] G. Moorhead,[bd] P. Morettini,[aj] S.V. Morozov,[bk] M. Mosidze,[cs] S.V. Mouraviev,[bj] E.W.J. Moyse,[s] A. Munar,[bu] A. Myagkov,[cb] A.V. Nadtochi,[bv] K. Nakamura,[cu,26] P. Nechaeva,[aj,27] A. Negri,[bt] S. Nemecek,[bz] M. Nessi,[s] S.Y. Nesterov,[bv] F.M. Newcomer,[bu] I. Nikitine,[cb] K. Nikolaev,[an] I. Nikolic-Audit,[av] H. Ogren,[ai] S.H. Oh,[ac] S.B. Oleshko,[bv] J. Olszowska,[y] A. Onofre,[bg,by] C. Padilla Aranda,[s] S. Paganis,[cl] D. Pallin,[u] D. Pantea,[n] V. Paolone,[bx] F. Parodi,[aj] J. Parsons,[bn] S. Parzhitskiy,[an] E. Pasqualucci,[ci] S.M. Passmored,[s] J. Pater,[bb] S. Patrichev,[bv] M. Peez,[az] V. Perez Reale,[bn] L. Perini,[be,bf] V.D. Peshekhonov,[an] J. Petersen,[s] T.C. Petersen,[v] R. Petti,[j,28] P.W. Phillips,[cf] J. Pina,[at,au,by] B. Pinto,[by] F. Podlyski,[u] L. Poggioli,[bq] A. Poppleton,[s] J. Poveda,[db] P. Pralavorio,[w] L. Pribyl,[s] M.J. Price,[s] D. Prieur,[cf] C. Puigdengoles,[f] P. Puzo,[bq] O. Røhne,[br] F. Ragusa,[be,bf] S. Rajagopalan,[j] K. Reeves,[dc,29] I. Reisinger,[aa] C. Rembser,[s] P.A. Bruckman de Renstrom,[bs] P. Reznicek,[ca] M. Ridel,[av] P. Risso,[aj] I. Riu,[ae,30] D. Robinson,[r] C. Roda,[bw] S. Roe,[s] O. Rohne,[br] A. Romaniouk,[bk] D. Rousseau,[bq] A. Rozanov,[w] A. Ruiz,[cz] N. Rusakovich,[an] D. Rust,[ai] Y.F. Ryabov,[bv] V. Ryjov,[s] O. Salto,[f] B. Salvachua,[b] A. Salzburger,[al,31] H. Sandaker,[g] C. Santamarina Rios,[s] L. Santi,[ak] C. Santoni,[u] J.G. Saraiva,[at,au,by] F. Sarri,[bw] G. Sauvage,[ar] L.P. Says,[u] M. Schaefer,[aw] V.A. Schegelsky,[bv] C. Schiavi,[aj] J. Schieck,[bm] G. Schlager,[s] J. Schlereth,[b] C. Schmitt,[ba] J. Schultes,[dc] P. Schwemling,[av] J. Schwindling,[cj] J.M. Seixas,[ch] D.M. Seliverstov,[bv] L. Serin,[bq] A. Sfyrla,[ae,32] N. Shalanda,[bh] C. Shaw,[af] T. Shin,[ag] A. Shmeleva,[bj] J. Silva,[by] S. Simion,[bq] M. Simonyan,[ar] J.E. Sloper,[s] S.Yu. Smirnov,[bk] L. Smirnova,[bl] C. Solans,[cz] A. Solodkov,[cb] O. Solovianov,[cb] I. Soloviev,[bv] V.V. Sosnovtsev,[bk] F. Spanò,[bn] P. Speckmayer,[s] S. Stancu,[cv] R. Stanek,[b] E. Starchenko,[cb] A. Straessner,[ab] S.I. Suchkov,[bk] M. Suk,[ca] R. Szczygiel,[x] F. Tarrade,[j] F. Tartarelli,[be] P. Tas,[ca] Y. Tayalati,[u] F. Tegenfeldt,[am] R. Teuscher,[ct] M. Thioye,[cq] V.O. Tikhomirov,[bj] C.J.W.P. Timmermans,[ce] S. Tisserant,[w] B. Toczek,[x]

[23]Now at Laboratoire de Physique Subatomique et de Cosmologie CNRS/IN2P3, Grenoble, France
[24]Now at CERN
[25]Now at Harvard University, Cambridge, U.S.A.
[26]Now at ICEPP, Tokyo, Japan
[27]Now at P.N. Lebedev Institute of Physics, Moscow, Russia
[28]Now at University of South Carolina, Columbia, U.S.A.
[29]Now at UT Dallas
[30]Now at IFAE, Barcelona, Spain
[31]Now at CERN
[32]Now at CERN

2010 JINST 5 P11006

L. Tremblet,[s] C. Troncon,[be] P. Tsiareshka,[bi] M. Tyndel,[cf] M.Karagoez. Unel,[bs] G. Unal,[s] G. Unel,[ai] G. Usai,[t] R. Van Berg,[bu] A. Valero,[cz] S. Valkar,[ca] J.A. Valls,[cz] W. Vandelli,[s] F. Vannucci,[av] A. Vartapetian,[d] V.I. Vassilakopoulos,[ag] L. Vasilyeva,[bj] F. Vazeille,[u] F. Vernocchi,[aj] Y. Vetter-Cole,[z] I. Vichou,[cy] V. Vinogradov,[an] J. Virzi,[h] I. Vivarelli,[bw] J.B.de. Vivie,[w,33] M. Volpi,[f] T. Vu Anh,[ae,34] C. Wang,[ac] M. Warren,[cw] J. Weber,[aa] M. Weber,[cf] A.R. Weidberg,[bs] J. Weingarten,[l,35] P.S. Wells,[s] P. Werner,[s] S. Wheeler,[a] M. Wiessmann,[bm] H. Wilkens,[s] H.H. Williams,[bu] I. Wingerter-Seez,[ar] Y. Yasu,[ap] A. Zaitsev,[cb] A. Zenin,[cb] T. Zenis,[m] Z. Zenonos,[bw] H. Zhang,[w] A. Zhelezko[bk] and N. Zhou[bn]

[a] *University of Alberta, Department of Physics, Centre for Particle Physics, Edmonton, AB T6G 2G7, Canada*

[b] *Argonne National Laboratory, High Energy Physics Division, 9700 S. Cass Avenue, Argonne IL 60439, United States of America*

[c] *University of Arizona, Department of Physics, Tucson, AZ 85721, United States of America*

[d] *University of Texas at Arlington, Department of Physics, Box 19059, Arlington, TX 76019, United States of America*

[e] *University of Athens, Nuclear & Particle Physics Department of Physics, Panepistimiopouli Zografou, GR 15771 Athens, Greece*

[f] *Institut de Fisica d'Altes Energies, IFAE, Universitat Autònoma de Barcelona, Edifici Cn, ES - 08193 Bellaterra (Barcelona) Spain*

[g] *University of Bergen, Department for Physics and Technology, Allegaten 55, NO - 5007 Bergen, Norway*

[h] *Lawrence Berkeley National Laboratory and University of California, Physics Division, MS50B-6227, 1 Cyclotron Road, Berkeley, CA 94720, United States of America*

[i] *University of Bern, Laboratory for High Energy Physics, Sidlerstrasse 5, CH - 3012 Bern, Switzerland*

[j] *Brookhaven National Laboratory, Physics Department, Bldg. 510A, Upton, NY 11973, United States of America*

[k] *Bogazici University, Faculty of Sciences, Department of Physics, TR - 80815 Bebek-Istanbul, Turkey*

[l] *Physikalisches Institut der Universitaet Bonn, Nussallee 12, D - 53115 Bonn, Germany*

[m] *Comenius University, Faculty of Mathematics Physics & Informatics, Mlynska dolina F2, SK - 84248 Bratislava, Slovak Republic*

[n] *National Institute of Physics and Nuclear Engineering (Bucharest -IFIN-HH), P.O. Box MG-6, R-077125 Bucharest, Romania*

[o] *Université Cadi Ayyad, Marrakech, Morocco*

[p] *Department of Physics, University of Coimbra, P-3004-516 Coimbra, Portugal*

[q] *Université Hassan II, Faculté des Sciences Ain Chock, B.P. 5366, MA - Casablanca, Morocco*

[r] *Cavendish Laboratory, University of Cambridge, J J Thomson Avenue, Cambridge CB3 0HE, United Kingdom*

[s] *European Laboratory for Particle Physics (CERN), CH-1211 Geneva 23, Switzerland*

[t] *University of Chicago, Enrico Fermi Institute, 5640 S. Ellis Avenue, Chicago, IL 60637, United States of America*

[33] Now at LAL-Orsay, France

[34] Now at Universität Mainz, Mainz, Germany

[35] Now at Georg-August-Universitaet, Goettingen, Germany

2010 JINST 5 P11006

[u] *Laboratoire de Physique Corpusculaire (LPC), IN2P3-CNRS, Université Blaise-Pascal Clermont-Ferrand, FR - 63177 Aubiere, France*

[v] *Niels Bohr Institute, University of Copenhagen, Blegdamsvej 17, DK - 2100 Kobenhavn 0, Denmark*

[w] *Université Méditerranée, Centre de Physique des Particules de Marseille, CNRS/IN2P3, F-13288 Marseille, France*

[x] *Faculty of Physics and Applied Computer Science of the AGH-University of Science and Technology, (FPACS, AGH-UST), al. Mickiewicza 30, PL-30059 Cracow, Poland*

[y] *The Henryk Niewodniczanski Institute of Nuclear Physics, Polish Academy of Sciences, ul. Radzikowskiego 152, PL - 31342 Krakow Poland*

[z] *Southern Methodist University, Physics Department, 106 Fondren Science Building, Dallas, TX 75275-0175, United States of America*

[aa] *Universitaet Dortmund, Experimentelle Physik IV, DE - 44221 Dortmund, Germany*

[ab] *Technical University Dresden, Institut fuer Kern- und Teilchenphysik, Zellescher Weg 19, D-01069 Dresden, Germany*

[ac] *Duke University, Department of Physics Durham, NC 27708, United States of America*

[ad] *Centre de Calcul CNRS/IN2P3, Lyon, France*

[ae] *Université de Genève, Section de Physique, 24 rue Ernest Ansermet, CH - 1211 Genève 4, Switzerland*

[af] *University of Glasgow, Department of Physics and Astronomy, UK - Glasgow G12 8QQ, United Kingdom*

[ag] *Hampton University, Department of Physics, Hampton, VA 23668, United States of America*

[ah] *Institute of Physics, Humboldt University, Berlin, Newtonstrasse 15, D-12489 Berlin, Germany*

[ai] *Indiana University, Department of Physics, Swain Hall West 117, Bloomington, IN 47405-7105, United States of America*

[aj] *INFN Genova and Università di Genova, Dipartimento di Fisica, via Dodecaneso 33, IT - 16146 Genova, Italy*

[ak] *INFN Gruppo Collegato di Udine and Università di Udine, Dipartimento di Fisica, via delle Scienze 208, IT - 33100 Udine;*
INFN Gruppo Collegato di Udine and ICTP, Strada Costiera 11, IT - 34014 Trieste, Italy

[al] *Institut fuer Astro- und Teilchenphysik, Technikerstrasse 25, A - 6020 Innsbruck, Austria*

[am] *Iowa State University, Department of Physics and Astronomy, Ames High Energy Physics Group, Ames, IA 50011-3160, United States of America*

[an] *Joint Institute for Nuclear Research, JINR Dubna, RU - 141 980 Moscow Region, Russia*

[ao] *Institut fuer Prozessdatenverarbeitung und Elektronik, Karlsruher Institut fuer Technologie, Campus Nord, Hermann-v.Helmholtz-Platz 1, D-76344 Eggenstein-Leopoldshafen*

[ap] *KEK, High Energy Accelerator Research Organization, 1-1 Oho Tsukuba-shi, Ibaraki-ken 305-0801, Japan*

[aq] *Royal Institute of Technology (KTH), Physics Department, SE - 106 91 Stockholm, Sweden*

[ar] *Laboratoire de Physique de Particules (LAPP), Université de Savoie, CNRS/IN2P3, Annecy-le-Vieux Cedex, France*

[as] *Laboratoire de Physique de Particules (LAPP), Université de Savoie, CNRS/IN2P3, Annecy-le-Vieux Cedex, France and Université Cadi Ayyad, Marrakech, Morocco*

[at] *Departamento de Fisica, Faculdade de Ciéncias, Universidade de Lisboa, P-1749-016 Lisboa, Portugal*

[au] *Centro de Física Nuclear da Universidade de Lisboa, P-1649-003 Lisboa, Portugal*

[av] *Université Pierre et Marie Curie (Paris 6) and Université Denis Diderot (Paris-7), Laboratoire de Physique Nucléaire et de Hautes Energies, CNRS/IN2P3, Tour 33 4 place Jussieu, FR - 75252 Paris Cedex 05, France*

2010 JINST 5 P11006

[aw] *Laboratoire de Physique Subatomique et de Cosmologie CNRS/IN2P3, Université Joseph Fourier INPG, 53 avenue des Martyrs, FR - 38026 Grenoble Cedex, France*

[ax] *Laboratoire de Physique Théorique et de Physique des Particules, Université Mohammed Premier, Oujda, Morocco*

[ay] *Lunds universitet, Naturvetenskapliga fakulteten, Fysiska institutionen, Box 118, SE - 221 00, Lund, Sweden*

[az] *Universidad Autonoma de Madrid, Facultad de Ciencias, Departamento de Fisica Teorica, ES - 28049 Madrid, Spain*

[ba] *Universität Mainz, Institut für Physik, Staudinger Weg 7, DE 55099, Germany*

[bb] *School of Physics and Astronomy, University of Manchester, UK - Manchester M13 9PL, United Kingdom*

[bc] *Universitaet Mannheim, Lehrstuhl fuer Informatik V, B6, 23-29, DE - 68131 Mannheim, Germany*

[bd] *School of Physics, University of Melbourne, AU - Parkvill, Victoria 3010, Australia*

[be] *INFN Sezione di Milano, via Celoria 16, IT - 20133 Milano, Italy*

[bf] *Università di Milano, Dipartimento di Fisica, via Celoria 16, IT - 20133 Milano, Italy*

[bg] *Departamento de Fisica, Universidade do Minho, P-4710-057 Braga, Portugal*

[bh] *B.I. Stepanov Institute of Physics, National Academy of Sciences of Belarus, Independence Avenue 68, Minsk 220072, Republic of Belarus*

[bi] *B.I. Stepanov Institute of Physics, National Academy of Sciences of Belarus, Independence Avenue 68, Minsk 220072, Republic of Belarus and Joint Institute for Nuclear Research, JINR Dubna, RU - 141 980 Moscow Region, Russia*

[bj] *P.N. Lebedev Institute of Physics, Academy of Sciences, Leninsky pr. 53, RU - 117 924, Moscow, Russia*

[bk] *Moscow Engineering & Physics Institute (MEPhI), Kashirskoe Shosse 31, RU - 115409 Moscow, Russia*

[bl] *Lomonosov Moscow State University, Skobeltsyn Institute of Nuclear Physics, RU - 119 991 GSP-1 Moscow Lenskiegory 1-2, Russia*

[bm] *Max-Planck-Institut für Physik, (Werner-Heisenberg-Institut), Föhringer Ring 6, 80805 München, Germany*

[bn] *Columbia University, Nevis Laboratory, 136 So. Broadway, Irvington, NY 10533, United States of America*

[bo] *Nikhef National Institute for Subatomic Physics, Kruislaan 409, P.O. Box 41882, NL - 1009 DB Amsterdam, Netherlands*

[bp] *Ohio State University, 191 West WoodruAve, Columbus, OH 43210-1117, United States of America*

[bq] *LAL, Université Paris-Sud, IN2P3/CNRS, Orsay, France*

[br] *University of Oslo, Department of Physics, P.O. Box 1048, Blindern T, NO - 0316 Oslo, Norway*

[bs] *Department of Physics, Oxford University, Denys Wilkinson Building, Keble Road, Oxford OX1 3RH, United Kingdom*

[bt] *Università di Pavia, Dipartimento di Fisica Nucleare e Teorica and INFN Pavia, Via Bassi 6 IT-27100 Pavia, Italy*

[bu] *University of Pennsylvania, Department of Physics, High Energy Physics, 209 S. 33rd Street Philadelphia, PA 19104, United States of America*

[bv] *Petersburg Nuclear Physics Institute, RU - 188 300 Gatchina, Russia*

[bw] *Universitadi Pisa, Dipartimento di Fisica E. Fermi and INFN Pisa, Largo B.Pontecorvo 3, IT - 56127 Pisa, Italy*

[bx] *University of Pittsburgh, Department of Physics and Astronomy, 3941 O'Hara Street, Pittsburgh, PA 15260, United States of America*

[by] *Laboratorio de Instrumentacao e Fisica Experimental de Particulas - LIP, and SIM/Univ. de Lisboa, Avenida Elias Garcia 14-1, PT - 1000-149, Lisboa, Portugal*

2010 JINST 5 P11006

[bz] *Academy of Sciences of the Czech Republic, Institute of Physics and Institute for Computer Science, Na Slovance 2, CZ - 18221 Praha 8, Czech Republic*

[ca] *Charles University in Prague, Faculty of Mathematics and Physics, Institute of Particle and Nuclear Physics, V Holesovickach 2, CZ - 18000 Praha 8, Czech Republic*

[cb] *Institute for High Energy Physics (IHEP), Federal Agency of Atom. Energy, Moscow Region, RU - 142 284 Protvino, Russia*

[cc] *Queen Mary, University of London, Mile End Road, E1 4NS, London, United Kingdom*

[cd] *Université Mohammed V, Faculté des Sciences, BP 1014, MO - Rabat, Morocco*

[ce] *Radboud University Nijmegen/NIKHEF, Dept. of Exp. High Energy Physics, Toernooiveld 1, NL - 6525 ED Nijmegen, Netherlands*

[cf] *Rutherford Appleton Laboratory, Science and Technology Facilities Council, Harwell Science and Innovation Campus, Didcot OX11 0QX, United Kingdom*

[cg] *University of Regina, Physics Department, Canada*

[ch] *Universidade Federal do Rio De Janeiro, Instituto de Fisica, Caixa Postal 68528, Ilha do Fundao, BR - 21945-970 Rio de Janeiro, Brazil*

[ci] *Università La Sapienza, Dipartimento di Fisica and INFN Roma I, Piazzale A. Moro 2, IT- 00185 Roma, Italy*

[cj] *Commissariàt a l'Enegie Atomique (CEA), DSM/DAPNIA, Centre d'Etudes de Saclay, 91191 Gif-sur-Yvette, France*

[ck] *Insitute of Physics, Academia Sinica, TW - Taipei 11529, Taiwan and Shandong University, School of Physics, Jinan, Shandong 250100, P. R. China*

[cl] *University of Sheffield, Department of Physics & Astronomy, Hounseld Road, Sheffield S3 7RH, United Kingdom*

[cm] *Insitute of Physics, Academia Sinica, TW - Taipei 11529, Taiwan*

[cn] *SLAC National Accelerator Laboratory, Stanford, California 94309, United States of America*

[co] *University of South Carolina, Columbia, United States of America*

[cp] *Stockholm University, Department of Physics and The Oskar Klein Centre, SE - 106 91 Stockholm, Sweden*

[cq] *Department of Physics and Astronomy, Stony Brook, NY 11794-3800, United States of America*

[cr] *Insitute of Physics, Academia Sinica, TW - Taipei 11529, Taiwan and Sun Yat-sen University, School of physics and engineering, Guangzhou 510275, P. R. China*

[cs] *Tbilisi State University, High Energy Physics Institute, University St. 9, GE - 380086 Tbilisi, Georgia*

[ct] *University of Toronto, Department of Physics, 60 Saint George Street, Toronto M5S 1A7, Ontario, Canada*

[cu] *University of Tsukuba, Institute of Pure and Applied Sciences, 1-1-1 Tennoudai, Tsukuba-shi, JP - Ibaraki 305-8571, Japan*

[cv] *University of California, Department of Physics & Astronomy, Irvine, CA 92697-4575, United States of America*

[cw] *University College London, Department of Physics and Astronomy, Gower Street, London WC1E 6BT, United Kingdom*

[cx] *University of California Santa Cruz, Santa Cruz Institute for Particle Physics (SCIPP), Santa Cruz, CA 95064, United States of America*

[cy] *University of Illinois, Department of Physics, 1110 West Green Street, Urbana, Illinois 61801 United States of America*

[cz] *Instituto de Física Corpuscular (IFIC), Centro Mixto UVEG-CSIC, Apdo. 22085, ES-46071 Valencia; Dept. Fïsica At., Mol. y Nuclear, Univ. of Valencia and Instituto de Microelectrónica de Barcelona (IMB-CNM-CSIC), 08193 Bellaterra, Barcelona, Spain*

2010 JINST 5 P11006

[da] *University of Victoria, Department of Physics and Astronomy,*
P.O. Box 3055, Victoria B.C., V8W 3P6, Canada
[db] *University of Wisconsin, Department of Physics,*
1150 University Avenue, WI 53706 Madison, Wisconsin, United States of America
[dc] *Bergische Universitaet, Fachbereich C, Physik,*
Postfach 100127, Gauss-Strasse 20, DE-42097 Wuppertal, Germany
[dd] *Yale University, Department of Physics,*
PO Box 208121, New Haven, CT06520-8121, United States of America
[de] *Yerevan Physics Institute, Alikhanian Brothers Street 2, AM - 375036 Yrevan, Armenia*

E-mail: robert.froeschl@cern.ch

ABSTRACT: In 2004 at the ATLAS (A Toroidal LHC ApparatuS) combined test beam, one slice of the ATLAS barrel detector (including an Inner Detector set-up and the Liquid Argon calorimeter) was exposed to particles from the H8 SPS beam line at CERN. It was the first occasion to test the combined electron performance of ATLAS. This paper presents results obtained for the momentum measurement p with the Inner Detector and for the performance of the electron measurement with the LAr calorimeter (energy E linearity and resolution) in the presence of a magnetic field in the Inner Detector for momenta ranging from 20 GeV/c to 100 GeV/c. Furthermore the particle identification capabilities of the Transition Radiation Tracker, Bremsstrahlungs-recovery algorithms relying on the LAr calorimeter and results obtained for the E/p ratio and a way how to extract scale parameters will be discussed.

KEYWORDS: Particle tracking detectors; Transition radiation detectors; Calorimeters; Large detector systems for particle and astroparticle physics

2010 JINST 5 P11006

Contents

2010 JINST 5 P11006

2010 JINST 5 P11006

1 Introduction

The Large Hadron Collider (LHC) collides 7 TeV proton beams, extending the available centre-of-mass energy by about an order of magnitude over that of existing colliders. Together with its high collision rate, corresponding to an expected integrated luminosity of 10–100 fb^{-1}/year, these energies will allow for the production of particles with high masses or high transverse momenta or other processes with low production cross-sections. The LHC will search for effects of new interactions at very short distances and for new particles beyond the Standard Model of particle physics (SM).

An excellent knowledge of the electron energy and momentum and of the photon energy in a large energy range is needed for precision measurements within and beyond the SM and to resolve possible narrow resonances of new particles over a large background. Therefore good energy resolution and linearity are needed for energies ranging from a few GeV up to a few TeV. An excellent and uniform measurement of the photon and electron energy is necessary for the potential discovery of the Higgs boson in the decay channels $H \rightarrow \gamma\gamma$ or $H \rightarrow ZZ^* \rightarrow 4e$. In addition good e/π separation capabilities are needed to suppress the background from QCD (quantum chromodynamics) jets[1] faking an electron signal by the required factor of 10^{-5}.

In order to test the performance of the ATLAS (A Toroidal LHC ApparatuS) subdetectors in conditions similar to those expected at LHC, a Combined Test-Beam (CTB) campaign was set up

[1] A jet is an ensemble of hadrons and other particles produced by the hadronization of a quark or gluon emitted in a narrow cone.

in 2004 where a full slice of the barrel detectors[2] was exposed to particles (electrons, pions, muons, protons and photons) of momenta ranging from 1 GeV/c to 350 GeV/c. The most important goals of this campaign were

- to test the detector performance in a combined set-up with final or close to final electronics and TDAQ (Trigger and Data Acquisition) infrastructure;
- to develop and test reconstruction and calibration software similar to that used by ATLAS;
- to validate the description of the data by Monte-Carlo (MC) simulations to prepare for the simulation of ATLAS data;
- to perform combined studies in a set-up very close to ATLAS (e.g. combined calorimetry, inner tracker and calorimetry).

This paper presents results combining the performance of various ATLAS subdetectors, namely the Pixel detector, the Semiconductor Tracker (SCT), the Transition Radiation Tracker (TRT) and the electromagnetic calorimeter.

The Pixel detector [1] is a silicon detector providing discrete spacepoints that are used for high resolution tracking. The SCT detector [2] consists of silicon strips providing stereo pairs to the tracking algorithms. The TRT [3–5] is a straw tube tracker with electron identification capabilities mainly through detection of transition radiation photons created in a radiator between the straws. In this way electrons can be distinguished from hadrons, mostly pions. The Pixel detector together with the SCT detector and the TRT compose the ATLAS Inner Detector.

The electromagnetic calorimeter of the ATLAS detector [6–9], is a lead and liquid argon (LAr) sampling calorimeter with accordion shaped absorbers, and has been designed to fulfill the above mentioned requirements [10, 11]. The used LAr calorimeter module will be described in more detail in section 2. Its performance has been measured in many test-beam campaigns, the results on linearity, uniformity and resolution for the LAr barrel calorimeter have been published in [12] and [13] for "close-to-ideal" conditions, with very little material upstream the calorimeter, with no other ATLAS detectors being operated simultaneously (potential sources of coherent noise) and without any magnetic field. The electron performance of the LAr barrel calorimeter at the CTB, including linearity, uniformity, and resolution with different amounts of material upstream the calorimeter and momenta ranging from 1 GeV to 250 GeV/c without magnetic field in the Inner Detector has been published in [14]. This paper presents results obtained for the electromagnetic performance of the LAr calorimeter (linearity and resolution) in the presence of a magnetic field in the Inner Detector.

After a description of the setup at the CTB (section 2), results obtained for the electromagnetic performance of the LAr calorimeter (linearity and resolution) in the presence of a magnetic field in the Inner Detector (section 3) and for the momentum measurement with the Inner Detector (section 4) are presented. Furthermore the e/π separation performance of the Transition Radiation Tracker is discussed in section 5. A bremstrahlungs-recovery algorithm relying on the LAr calorimeter is presented in section 6 and results obtained for the E/p ratio, i.e. the ratio of the

[2]The barrel detectors constitute the central part of the ATLAS detector, i.e. around the plane through the interaction point and perpendicular to the beam axis.

2010 JINST 5 P11006

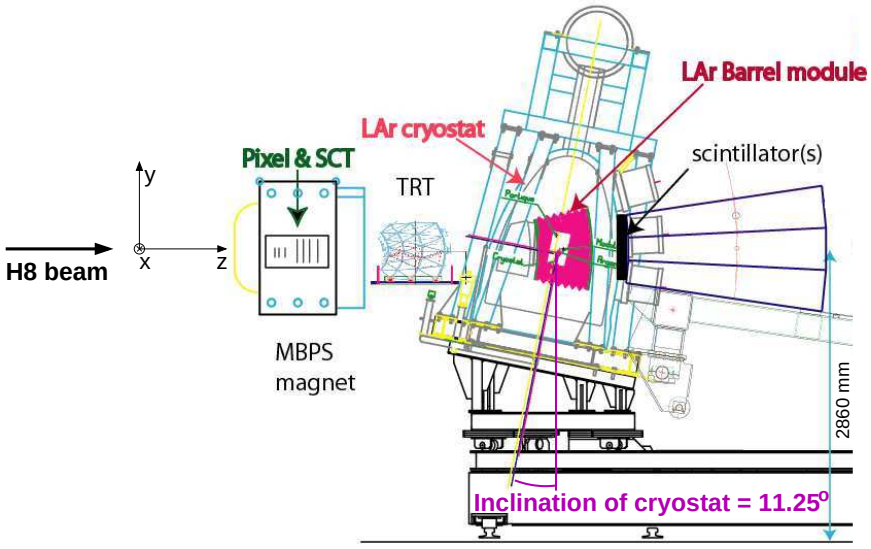

Figure 1. Schematic view of the H8 CTB set-up, including the inner detector components and the LAr and Tile calorimeters.

energy measured by the electromagnetic calorimeter and the momentum measured by the Inner Detector, and a way how to extract scale parameters are discussed in section 7.

2 Setup

During the 2004 CTB campaign all ATLAS sub-detectors (barrel wedge) collected data with parts of their detectors in the H8 beam line of the CERN Super Proton Synchrotron (SPS) (see section 2.3). The detectors were installed in the beam line with relative positions as close as technically possible to the real ATLAS geometry: the distance between sub-detectors, the pointing geometry, and the magnetic field orientation have been preserved where permitted, although the distance between the Inner Detector and the calorimeters is much larger than in ATLAS (figure 1, figure 2, length scale in figure 4). A detailed description of the whole set-up can be found in [15].

2.1 Sub-detectors geometry and granularity

The ATLAS combined set-up at the 2004 CTB included:

- Six modules of the Pixel detector (2 modules for each of the three pixel layers: B, 1 and 2 as defined for the ATLAS detector) [1];
- Eight modules of the Semiconductor Tracker (SCT) detector (2 modules per layer, as in the ATLAS detector) [2];
- Two barrel wedges of the Transition Radiation Tracker (TRT) [3] corresponding to $1/16$ of one barrel wheel;
- One module of the LAr electromagnetic barrel calorimeter (EMB) corresponding to $1/16$ of one barrel wheel [16];

2010 JINST 5 P11006

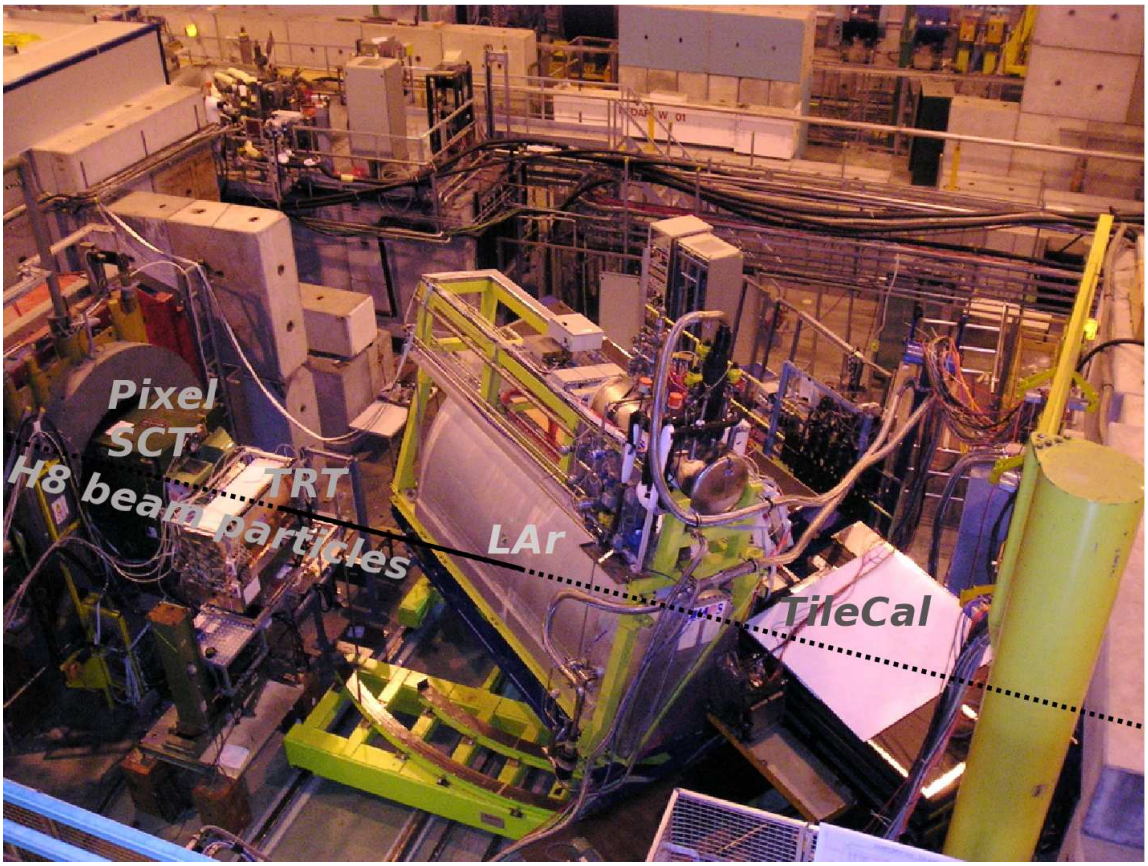

Figure 2. The ATLAS 2004 CTB set-up. The beam is coming from the left side. From left to right are located the inner detector components including a magnet, the LAr cryostat with the Tile Calorimeter modules right behind. The muon set-up is located on the right outside of the scope of the picture.

- Three long barrel modules and three extended barrel modules[3] of the hadronic Tile Calorimeter [17];
- Muon spectrometer: three stations of barrel Monitored Drift Tube (MDT) chambers and three stations of MDT endcap chambers[4] [18].

The Inner Detector (ID) consists of three different subdetectors, namely Pixel, SCT and TRT. The CTB coordinate system is chosen to be right-handed, with the Z-axis along the beam direction and the Y-axis pointing vertically towards the sky as depicted in figure 1. The Pixel and SCT modules were located inside a MBPS magnet (MBPSID). This magnet is one meter long, and is often used at CERN as bending magnet for the accelerators. It provided a field along the x direction, deviating the particles in ϕ (angle in the z-y plane), as in the ATLAS detector. It is mainly operated with a -850 A current, providing an integrated field of ~ 1.4 Tm. In such a field the deviation for a 10 GeV/c electron is about 4 cm at the exit of the magnet, and ~ 11 cm at the front face of the

[3]The three extended barrel modules were only present at the beginning of the data taking period.

[4]During parts of the test-beam campaign an additional barrel muon chamber was placed directly downstream of the Tile Calorimeter set-up (before the beam dump).

2010 JINST 5 P11006

electromagnetic barrel module; in ATLAS, a 10 GeV/c electron produced at the vertex is deviated by ~ 13 cm. Even though the set-up could not be identical as the ATLAS set-up, the configuration provided a good enough approximation for many studies. The TRT modules were located outside the magnet due to space limitations.[5] The origin of the global reference frame is located at the entrance of the MBPSID magnet.

A Pixel module consists of a single silicon wafer with an array of 50 μm$\times$400 μm pixels that are readout by 16 chips. In the CTB setup, six Pixel modules are used and distributed by pairs in three layers and two sectors. The distance along the beam axis between the different layers and the location of the modules within each layer coincides with the arrangement of the modules in ATLAS. The active area of each module is z$\times$y = 60.8$\times$16.4 mm^2. Each module is positioned at an angle of about 20^o with a superposition of the two modules in each layer of about 200 μm.

The SCT detector consists of silicon microstrip sensor modules with 80 μm pitch. Each module has two sets of sensors glued back-to-back around a central TPG (Thermo-Pyrolithic Graphite) spine with a relative rotation of 40 mrad with respect to each other to give the required capability for a 3D space point reconstruction. The SCT has a single module type design for the barrel region, plus three types for the end-caps (namely outer, middle and inner according to their position in the end-cap wheels). Though the CTB was meant to reproduce a slice of the ATLAS barrel, eight SCT end-cap outer modules were used in the final setup. As in the pixels case, two SCT modules are used in each of the four layers and distributed in two sectors. The SCT module location is similar to the one that may be encountered in ATLAS, but the modules were mounted perpendicular to the beam axis. The four SCT layers cover an area of z$\times$y = 120.0$\times$60.0 mm^2. There is a 4 mm overlap between the two modules in each layer. Because of hardware problems, the front side of the lower SCT module in the third layer was not functioning.

The TRT setup is made of two barrel wedges. Each wedge is equivalent to 1/16 of the circumference of a cylinder, with inner radius of 558 mm and outer radius of 1080 mm and overall length along the Z-axis of 1425.5 mm. For some of the runs, the Pixel and SCT detector were exposed to a magnetic field. The magnetic field profile has also been measured and its non uniformity has been also considered in the software and the track reconstruction has been carried out taking into account its effects.

The alignment of the Inner Detector components has been done with charged-hadron beams with beam momenta between 5 and 180 GeV/c [19]. The RMS for the residuals was 10 μm for the Pixel modules and 25 μm for the SCT modules.

The electromagnetic LAr calorimeter module was built for the ATLAS CTB, using absorbers, electrodes, motherboards, connectors and cables left from the production of the 32 ATLAS electromagnetic barrel modules. An extensive description of the electromagnetic barrel calorimeter and its modules can be found in [16]. The electromagnetic barrel is a lead/LAr sampling calorimeter and is longitudinally segmented into three layers[6] (strip, middle and back layer), each having different longitudinal thickness and transverse segmentation into read-out cells with the following granularity (see figure 3): the strip layer is finely segmented in pseudorapidity[7] η with a granularity of 0.025/8 η-units, but has only four subdivisions in ϕ per module and hence a granularity of 2π/64;

[5] In ATLAS, the TRT detector is inside the solenoidal field.

[6] These three layers are also called the accordion part of the calorimeter.

[7] The pseudorapidity η is defined as $\eta = -\ln\tan\frac{\theta}{2}$.

2010 JINST 5 P11006

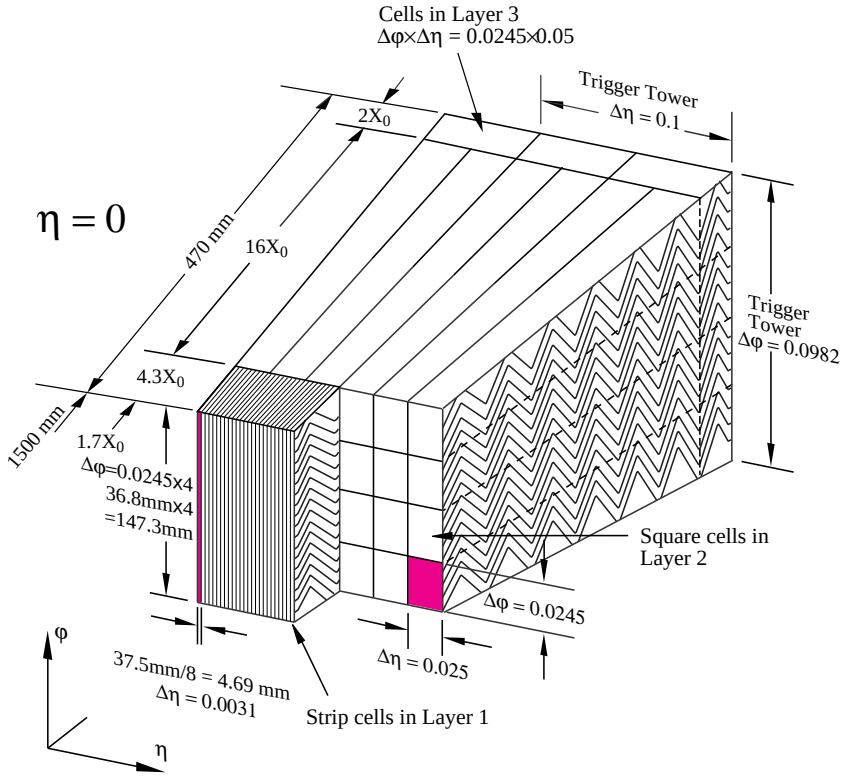

Figure 3. Sketch of a barrel module of the electromagnetic LAr calorimeter. The accordion structure and the granularity in η and φ of the cells of each of the three layers is shown.

the middle layer has a segmentation of 0.025 in η and $2\pi/256$ in ϕ; the back layer has the same ϕ granularity as the middle one, but is twice as coarse in η (0.05). A thin presampler (PS) detector is mounted in front of the LAr calorimeter module: the PS is segmented in η with a granularity of ~ 0.025 (as the middle layer), and has a granularity of $2\pi/64$ in ϕ (as the strip layer). Between the PS and the strip layer readout-out cables and signal collection boards are installed.

The cryostat containing the module of the electromagnetic calorimeter is installed on a movable support table which can rotate in θ (angle in the x-z plane) and translate in x. It was therefore possible to move different pseudorapidity regions into the particle beam, but it was not possible to rotate in azimuth ϕ.

2.2 Read-out electronics, data acquisition and reconstruction software

The Front-End Boards (FEB) and back-end electronics used for the CTB campaign were the final prototypes of the boards built to equip the LAr calorimeters installed in ATLAS. A detailed description of these boards is available in dedicated publications for the front-end board [20], calibration board [21], controller and tower builder boards [22], and the Read-Out Driver (ROD) and back-end system [23]. Further explanations on the LAr read-out system used for the CTB can be found in [24]. Similarly to the detector set-up and read-out, the Data-Acquisition system (TDAQ) software in operation for the CTB data taking was an early version of the packages developed for

2010 JINST 5 P11006

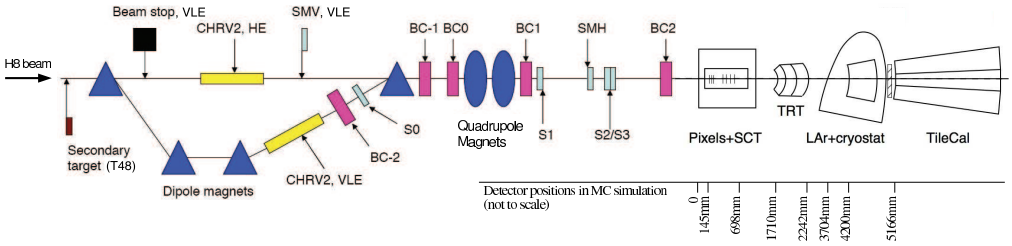

Figure 4. Outline of the beam line instrumentation. [15]. The straight line represents the high energy beam line that was used for the data analyzed in this paper. The acronyms are explained in the text.

ATLAS [25].

Previous stand-alone test-beam campaigns had been monitored and analysed using specific software. For this campaign, the C++ reconstruction software in the Athena framework, up to then only used for Monte Carlo simulation based studies [26], has been adapted to process the data from the 2004 CTB. The experience from the 2004 CTB has been invaluable in the development of ATLAS software used in data recording of events from cosmic rays hitting the detector since 2006 and in LHC collisions.

2.3 Beam lines set-up and instrumentation

The CERN H8 beam line provides hadrons, electrons or muons with momenta from 1 GeV/c to 350 GeV/c. The H8 beam is created by extracting 400 GeV/c protons from the SPS towards the North Area experimental zone. From the primary target (T4, beryllium up to 300 mm in length), the secondary beam had momenta between 9 GeV/c to 350 GeV/c. We call this the High Energy (HE) beam line. A secondary filter target (8 or 16 mm of lead for an electron beam) was introduced to produce a "pure" electron beam. The beam can also be diverted onto an additional target (T48) further downstream, close to the experiment to provide momenta from 1 GeV/c to 9 GeV/c. This is called the Very Low Energy (VLE) beam line.

Figure 4 shows the beam line instrumentation for the HE and the VLE beam lines [15]. Three Čerenkov counters were used on the H8 beam line, CHRV1 was furthest upstream, and the other two were placed about 1 m upstream of the last bending magnet of the VLE spectrometer (CHRV2), one on HE beam line for momenta > 9 GeV/c and the other one on the path of the particles in the VLE beam line. Five beam chambers (BC-2, BC-1, BC0, BC1, and BC2) were used to define the beam profile. A beam stop was inserted after the first bending magnet of the VLE spectrometer and the scintillator SMV behind served as a muon veto. The scintillators S1, S2 and S3 were used for the main trigger, SMH (scintillator with a hole of diameter 3.4 cm) was used in anti-coincidence to veto the muon halo of the beam.

The beam momentum measurement at the CTB is described in detail in [14]. The absolute energy scale of the electromagnetic LAr barrel calorimeter has been determined by means of selected electron runs (not listed in table 1) with a nominal beam momentum of 180 GeV/c and without magnetic field in the MBPS magnet. This scale has been used for the entire CTB. It depends on the LAr temperature which was measured to be 89.7 ± 0.1 K. A comparison between the measured visible energy in a 3×3 cluster (see section 3.3.2 for a description of the clustering) and

2010 JINST 5 P11006

Table 1. Run number, nominal beam momentum, estimated average beam momentum, beam spread, nominal η impact position, current in the MBPS magnet that provides the field for the inner detector and the total number of events taken for the data samples before and after cuts and the number of events after cuts for the Monte Carlo simulation used in this analysis.

Run number	$p_{beam}^{nominal}$ (GeV/c)	$< p_{beam} >$ (GeV/c)	$\sigma(p_{beam})$ (GeV/c)	$\eta^{nominal}$	MBPS current (A)	Events Data	Events Data (after cuts)	Events MC (after cuts)
2102399	100	99.80 ± 0.11	0.24	0.45	-850	200000	19075	55665
2102400	50	50.29 ± 0.10	0.12	0.45	-850	200000	19723	56151
2102413	20	20.16 ± 0.09	0.05	0.45	-850	70000	6583	41600
2102452	80	80.0 ± 0.10	0.19	0.45	-850	200000	8180	57473

the simulated one yielded the absolute energy scale of the calorimeter that is used throughout this paper. Details on the runs used and the method applied to extract the energy scale are described in [14]. The uncertainty on the obtained absolute energy scale has been estimated to be 0.7 %. It accounts for the HE spectrometer current error for these runs (~ 0.04 %); the absolute scale for the CTB ($25\%/p_{\text{beam}} \oplus 0.5\% = 0.52\%$ for $p_{beam} = 180$ GeV/c) and the detector response uniformity (< 0.4 %, uniformity, see [14] for details). These three components have been added in quadrature.

3 Energy measurement with the Liquid Argon calorimeter

After a brief description of the data samples (section 3.1) and the event selection (section 3.2), the way the energy deposited in a single calorimeter cell is measured and how clusters are formed out of these cells is recapitulated in section 3.3 . This is followed by a comparison of the Monte Carlo simulation to data (section 3.4). Finally a Monte Carlo simulation based calibration procedure for the cluster energy is presented in section 3.5 and applied to data in section 3.6 in order to extract the linearity and resolution for the liquid argon calorimeter in the presence of a magnetic field in the Inner Detector.

3.1 Data samples

The data samples that were taken during the CTB 2004 and used for the analysis in this paper are listed in table 1. The average beam momentum, denoted $< p_{beam} >$, and the beam spread, denoted $\sigma(p_{beam})$, were computed for each run using the collimator settings and the currents from the beam momentum selection spectrometer as described in [14].

3.2 Event selection

This section describes the event selection procedure for the CTB 2004. Section 3.2.1 is devoted to particle identification for electrons, section 3.2.2 describes the requirements concerning the beam quality and section 3.2.3 deals with detector imperfections. Finally section 3.2.4 discusses the quality requirements for reconstructed electron-like objects.

3.2.1 Particle identification

The purpose of the procedures described in this subsection is to select only events for the analysis that are triggered from an electron from the beam entering the calorimeter. Requirements concern-

2010 JINST 5 P11006

ing measurement variables from the beam line instrumentation present only in the data samples are only applied there. Requirements that involve measurement variables from the calorimeters or the inner detector are applied both to the data and to the simulation samples in order to avoid introducing any bias. When cuts were used only on data, it is explicitly stated.

The following requirements have to be met for an event to be accepted:

1. Less than 700 MeV is deposited in the first tile calorimeter layer. The purpose of this requirement is to reject pions.

2. Less than one percent of the energy deposited in the calorimeters is deposited in the tile calorimeter. The purpose of this requirement is to reject pions.

3. There must be at least 20 hits in the TRT. The purpose of this requirement is to be sure to have a good track in the TRT.

4. TRT High Level Hit Probability[8] > 0.15: The purpose of this requirement is to reject pions and muons . This requirement is applied only to the data samples, since the TRT High Level Hit Probability is not correctly modeled in the simulation, and only electrons have been simulated.

5. Trigger from the trigger scintillators S1$\wedge$S2: This requirement guarantees that only beam particle triggered events are considered and not random triggers that were injected to measure pedestal levels. Since the trigger scintillators are not simulated, the requirement is applied only to the data samples.

6. Muon halo veto scintillator (SMH) < 460 ADC: The purpose of this requirement is to reject muons. Since the muon halo veto scintillator is not simulated, the requirement is applied only to the data samples.

7. Cherenkov counter CHRV2,HE > 650 ADC: The purpose of this requirement is to reject pions for the run at 20 GeV/c nominal beam momentum. Since the cherenkov counter is not simulated, the requirement is applied only to the data samples.

3.2.2 Beam quality

Two additional cuts are applied to the data to ensure that only particles from the central part of the beam and no particles from the beam halo are used.

1. The x values measured by the beam chambers BC-1 and BC0 are linearly correlated since the setup is rigid and there is no magnetic field in the flight path between these two beam chambers. The same is true for y values. The left figures of figure 5 show the distributions for x and y. A line is fitted to each of the distributions and the orthogonal distances ($\Delta x_{\text{BC-1}}$ and $\Delta y_{\text{BC-1}}$) are shown in the right figures of figure 5. Gaussians are fitted to the orthogonal distance distributions and 3 times the σ of a Gaussian is defined as the largest allowed absolute orthogonal distance. The x and y distributions and the corresponding orthogonal distance distributions with these cuts applied are shown in figure 6.

[8] The TRT High Level Hit probability is explained in section 5.

2010 JINST 5 P11006

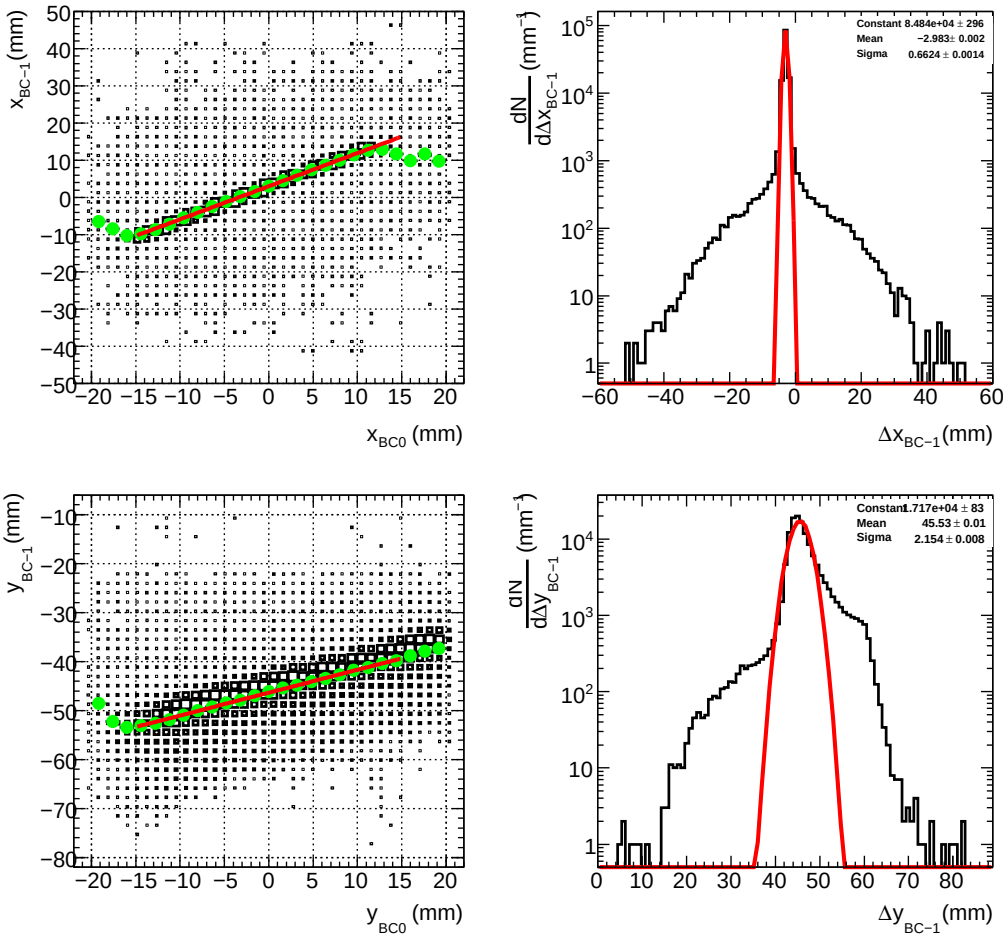

Figure 5. Beam chambers BC-1 vs. BC0 x (top left) and y (bottom left) measurements with fitted line. Distribution of the orthogonal distances ($\Delta x_{\text{BC-1}}$ and $\Delta y_{\text{BC-1}}$) from this line for x (top right) and y (bottom right) values together with a Gaussian fitted to the core of the distribution.

Table 2. Allowed ranges for the x and y values (denoted $BC1_x$ and $BC1_y$) of beam chamber BC1 for all beam momenta.

$p_{beam}^{nominal}$ (GeV/c)	(min,max) $BC1_x$ (mm)	(min,max) $BC1_y$ (mm)
20	$(-15,+7)$	$(-13,+12)$
50	$(-15,+5)$	$(-15,+15)$
80	$(-5,+7)$	$(-10,+10)$
100	$(-15,+7)$	$(-15,+15)$

2. The x and y values (denoted $BC1_x$ and $BC1_y$) of beam chamber BC1 are restricted to ranges where the total visible energy in the electromagnetic calorimeter is flat with respect to $BC1_x$ and $BC1_y$. The intervals used are given in table 2.

2010 JINST 5 P11006

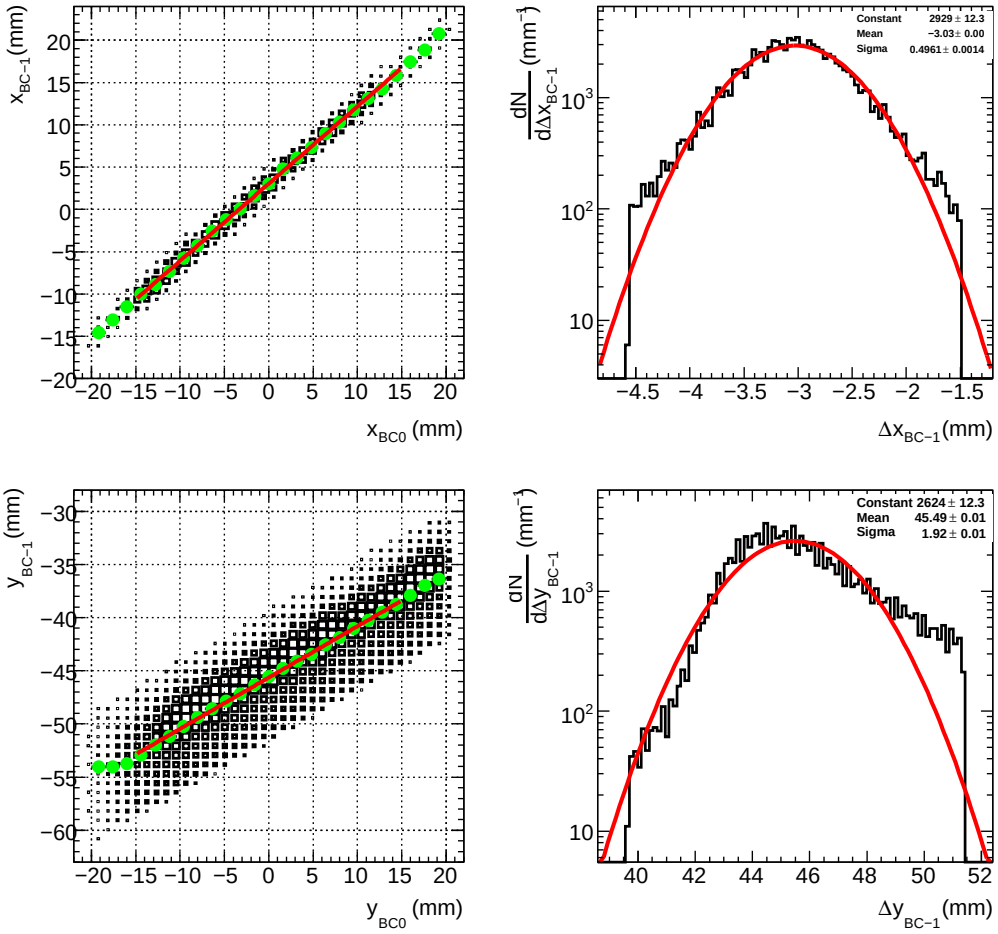

Figure 6. Beam chambers BC-1 vs. BC0 x (top left) and y (bottom left) measurements with fitted line with 3σ cut applied. Distribution of the orthogonal distances ($\Delta x_{\text{BC-1}}$ and $\Delta y_{\text{BC-1}}$) from this line for x (top right) and y (bottom right) values together with a Gaussian fitted to the core of the distribution.

3.2.3 Detector imperfections

This subsection describes the procedures to discard events that have been affected by detector imperfections.

Coherent noise in the presampler. In order to reject events with coherent noise in the presampler layer of the LAr calorimeter, the distribution of the presampler cell energies of all cells outside the region where the beam hits the calorimeter is considered, i.e. $|\eta_{cell} - \eta_{beam}| > 0.2$. If there is no coherent noise present, this distribution is a Gaussian with mean equal to 0 and an rms equal to the average noise of the cells. Let n_{PS}^{+} denote the number of presampler cells with positive energy and n_{PS}^{-} the number of presampler cells with negative energy. An event is rejected if $\left|\frac{n_{PS}^{+}-n_{PS}^{-}}{n_{PS}^{+}+n_{PS}^{-}}\right| > 0.6$. Since the coherent noise is not simulated this cut is only applied to the data samples. Less than 0.2% of the events are rejected by this cut.

Shaper problem. The four cells at $0 < \varphi_{cell} < 0.1$, $\eta_{cell} = 0.3875$ in the middle layer of the LAr calorimeter suffered from an unstable signal shaper. The stochastic distortion of the signal shape introduced a variation of the order of 3% for the gain values. Although the effect on the reconstructed cluster energy is $\ll 1\%$, all events with clusters that contain any of these cells are discarded. In order not to introduce a bias, this cut is applied both to the data samples and to the simulation samples.

3.2.4 Quality of reconstructed objects

The purpose of the requirements described in this subsection is to select events that have a reconstructed electron-like object. This object consists of a cluster in the electromagnetic calorimeter and a track in the Inner Detector that is geometrically matched to the cluster.

Track to cluster matching. A track[9] in the Inner Detector can be extrapolated to the LAr calorimeter and the η and φ coordinates of this extrapolation, denoted η_{Track} and φ_{Track} are compared with the η and φ coordinates computed for the clusters in the calorimeter, denoted $\eta_{Cluster}$ and $\varphi_{Cluster}$. In order for a track to be matched to a cluster the following two conditions are imposed

- $|\varphi_{Track} - \varphi_{Cluster}| < 0.05$ rad,
- $|\eta_{Track} - \eta_{Cluster}| < 0.01$.

An event is accepted for the analysis if there is at least one matched track-cluster combination.

Track quality. At least 2 hits in the Pixel detector for the matched track are required. This requirement ensures an acceptable track quality.

3.3 Energy measurement

The calibration of the energy measurement of the LAr calorimeter consists of two consecutive steps. First the raw signal (in ADC counts) for each cell is converted into the deposited energy in the cell. This step is denoted as *electronic calibration* and briefly discussed in section 3.3.1. During the second step clusters are formed out of calorimeter cells and an estimate of the initial energy of the impinging particle associated with the cluster is computed. The cluster formation algorithm is briefly described in section 3.3.2 and section 3.5 is devoted to a Monte Carlo simulation based procedure for computing the estimate for the initial energy of the particle.

3.3.1 Electronic calibration

A very detailed discussion of the electronic calibration and cell energy reconstruction for the LAr EMB calorimeter is given in [24].

The signals that are induced by the drifting electrons in the liquid argon gaps of the calorimeter are amplified, shaped and then digitized at a sampling rate of 40 MHz in one of the three available gain channels. Since the particles in the testbeam (unlike in the LHC) do not arrive in phase with the 40 MHz clock, the phase is measured for each event by a scintillator in the beam line. This measured event phase is then used to select the correct set of optimal filtering constants. The sets

[9] The track reconstruction for the CTB 2004 is described in section 4.1.

2010 JINST 5 P11006

of optimal filtering constants had been prepared previously for all different event phases (1 set per 1 ns). In the CTB 2004 setup six samples are digitized. From these six samples five samples s_i closest to the signal peak are chosen and the signal amplitude ADC_{peak} is computed by the *Optimal Filtering Method* [27]

$$ADC_{peak} = \sum_{i=1}^{5} a_i \left(s_i - p\right), \tag{3.1}$$

where a_i are the optimal filtering coefficients that are computed from the predicted ionization pulses obtained using the technique described in [28] and p is the pedestal value which is the mean of the signal values generated by the electronic noise that is measured in dedicated calibration runs.

From the signal amplitude ADC_{peak} the cell energy E_{cell} is computed by

$$E_{\text{cell}} = F_{DAC\rightarrow\mu A} F_{\mu A\rightarrow \text{MeV}} \frac{1}{\frac{\text{M}^{Phys}}{\text{M}^{Cal}}} \sum_{i=1,2} R_i \left[ADC_{peak}\right]^i, \tag{3.2}$$

where the factors R_i model the electronic gain with a second order polynomial, converting the ADC_{peak} amplitude into the equivalent current units (*DAC*). The constant factor $\text{M}^{Phys}/\text{M}^{Cal}$ takes the difference between the amplitudes of a calibration and an ionization signal of the same current for the electronic gain into account [28–31]. The constants $F_{DAC\rightarrow\mu A}$ and $F_{\mu A\rightarrow \text{MeV}}$ finally transform the current (*DAC*) into energy (MeV). The details of the computation and validation of all the calibration constants used in eq. (3.1) and eq. (3.2) are described in [24].

The extraction of the $F_{\mu A\rightarrow \text{MeV}}$ conversion factor determines the absolute energy scale of the calorimeter and is extracted by comparing the energy response in selected runs with MC simulations (see more detailed description in section 2.3 and [14]).

3.3.2 Cluster building

In order to reduce the noise contribution to the energy measurement, a finite number of cells is used to calculate the energy. The process of choosing which cells are used is called *cluster building*. Several methods exist [32], e.g. topological clustering and sliding window clustering. In the analysis here the standard ATLAS clustering [32] is used. For electrons, this means that in order to find the seed position for the cluster, a window of 5×5 middle cells ($\eta \times \varphi$ extension) is slid across the calorimeter and the energy content in these 25 middle cells is computed. The position of the central cell of the 5×5 window with the highest energy content is then used as seed position for the cluster. This seed position is propagated to the other layers of the calorimeter. For each layer, the cells contained in windows centered at the given seed position for the layer belong to the cluster. The size of the window is different for the various layers, e.g. for the middle layer the size is 3×7.

A 3×3 cluster has been used to extract the absolute energy scale of the electromagnetic LAr barrel calorimeter from selected electron runs (not listed in table 1) with a nominal beam momentum of 180 GeV/c and without magnetic field in the MBPS magnet. Details can be found in [14].

3.4 Monte Carlo simulation and comparison to data

After a description of the Monte Carlo simulation setup in section 3.4.1, the results of the Monte Carlo simulation are compared to data taken in the CTB 2004. This comparison is performed for the

2010 JINST 5 P11006

energy response for the different layers of the calorimeter (subsection 3.4.2) and the development of the electromagnetic shower (section 3.4.3).

Since the calibration procedure (section 3.5) relies on Monte Carlo simulation a sufficiently good agreement between the Monte Carlo simulation and the data is necessary to achieve the required level of accuracy for the electron energy measurement. For the required linearity of 0.5% the agreement between the Monte Carlo simulation and the data for the sum of the visible energies of all cells in a cluster also has to be at the level of 0.5%.

3.4.1 Monte Carlo simulation of the Combined Test Beam 2004

The response of the detector setup of the Combined Test Beam 2004 to the various beam particles is simulated using the GEANT4 toolkit [33]. GEANT4 uses Monte Carlo methods to simulate the physics processes when particles pass through matter. The QGSP-EMV physics list was used to parameterize these physics processes. The details of the geometric description of the Combined Test Beam 2004 in GEANT4 are described in [34]. The simulated energy deposits are reconstructed with the same software as the data. This is all done inside the ATLAS offline software framework ATHENA, release 12.0.95.

The far upstream material (section 2) is taken into account by introducing a piece of aluminum with the equivalent thickness of 15% of a radiation length placed directly downstream of the GEANT4 particle generator. All particles that emerge from the far upstream material are recorded in the simulation and are used to model the effect of the beam line acceptance (section 3.4.1).

One effect that is not modeled in the simulation is the cross talk between strip and middle layers. This cross talk has been measured by analyzing the response of the various cells to calibration pulses [35, 36]. A cross-talk of $X_{\mathrm{mi}\to\mathrm{st}} = 0.05\,\%$ from the middle layer to the strip layer and of $X_{\mathrm{st}\to\mathrm{mi}} = 0.15\,\%$ from the strip layer to the middle layer have been obtained (peak-to-peak values). They are accounted for after the energy reconstruction by redistributing $8 \cdot X_{\mathrm{mi}\to\mathrm{st}} \cdot E_{\mathrm{Middle}}$ from the middle layer energy[10] to the strip layer energy[11] and $X_{\mathrm{st}\to\mathrm{mi}} \cdot E_{\mathrm{Strips}}$ from the strip layer energy to the middle layer energy.

The simulated electron momentum that is used in the Monte Carlo simulation is the nominal beam momentum $p_{beam}^{nominal}$ for the given run (table 1). Since the average beam momentum $< p_{beam} >$ is not identical to the nominal beam momentum $p_{beam}^{nominal}$ all energies in the Monte Carlo simulation are scaled by $< p_{beam} > / p_{beam}^{nominal}$. This is justified because the nonlinearities of the detector response are negligible for such scaling factors very close to unity for the investigated beam momentum range. The beam spread $\sigma(p_{beam})$ for the given run (table 1) was also not simulated and therefore has to be subtracted for the Monte Carlo simulation to data comparison of the resolution.

The beam profiles change with the beam energy due to modifications in the beam optics. Consequently, in order to guarantee the best agreement between data and MC, the beam profiles have been matched run-by-run: in the "standalone period" and the "calorimeter and TRT period" the MC beam profiles are generated as wide flat distributions in the (η, ϕ) plane, whereas in the "fully combined period" they are generated to match the profiles measured in the SCT and Pixel detectors. For all periods the events are then re-weighted in order to obtain the best match between the (η, ϕ) distributions obtained in MC and in the data in the calorimeter.

[10] The sum of the energies of all cells of a given layer is denoted as its layer energy.

[11] Each middle cell has 8 adjacent strip cells.

2010 JINST 5 P11006

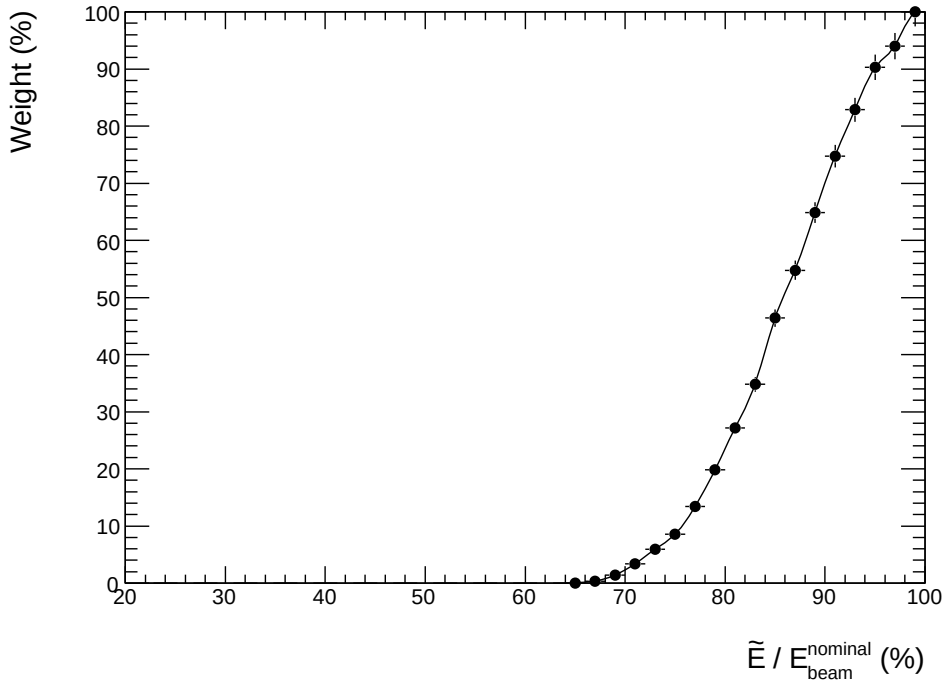

Figure 7. Beam line acceptance weight function.

Beam line acceptance. Particles which loose a significant amount of energy in the beam line will have a smaller probability to reach the trigger scintillators. Since the beam line was not modeled in the Monte Carlo simulation, a weighting scheme is employed to simulate the acceptance of the beam line. In the simulation a detector is placed directly after the far upstream material (see section 2 and section 3.4.1). For each event the ratio of the energy of the most energetic particle $\tilde{E}$ measured by this detector and the nominal beam energy, i.e. $\tilde{E}/E_{beam}^{nominal}$, is used to compute a weight from the weighting curve shown in figure 7. This weight is attributed to all measurement variables of the event. The weighting curve has been obtained by a dedicated beam line simulation beforehand [37]. The application of the beam line acceptance weight has no significant impact on the calorimeter measurements, but is needed for a correct description of the tail of the momentum measurement in the inner detector (see figure 8).

3.4.2 Energy response

The Monte Carlo simulation to data comparisons for a beam momentum of 50 GeV/c for the reconstructed presampler layer energies E_{PS}, for the reconstructed strip layer energies E_{strips}, for the reconstructed middle layer energies E_{Middle} and for the reconstructed back layer energies E_{Back} are shown in figure 9. The agreement concerning the shapes of the distributions is good in general.

The Monte Carlo simulation to data comparisons of the visible energy E_{Vis} which is the sum of all layer energies is presented in figure 10 for all beam momenta. The shape agreement is best at $p_{beam} = 20$ GeV/c and deteriorates with increasing beam momentum. One cause for this discrepancy is the fact that the beam spread $\sigma(p_{beam})$ for the given run (table 1) was not simulated and the impact of the beam spread is larger for higher beam momenta since the relative resolution

2010 JINST 5 P11006

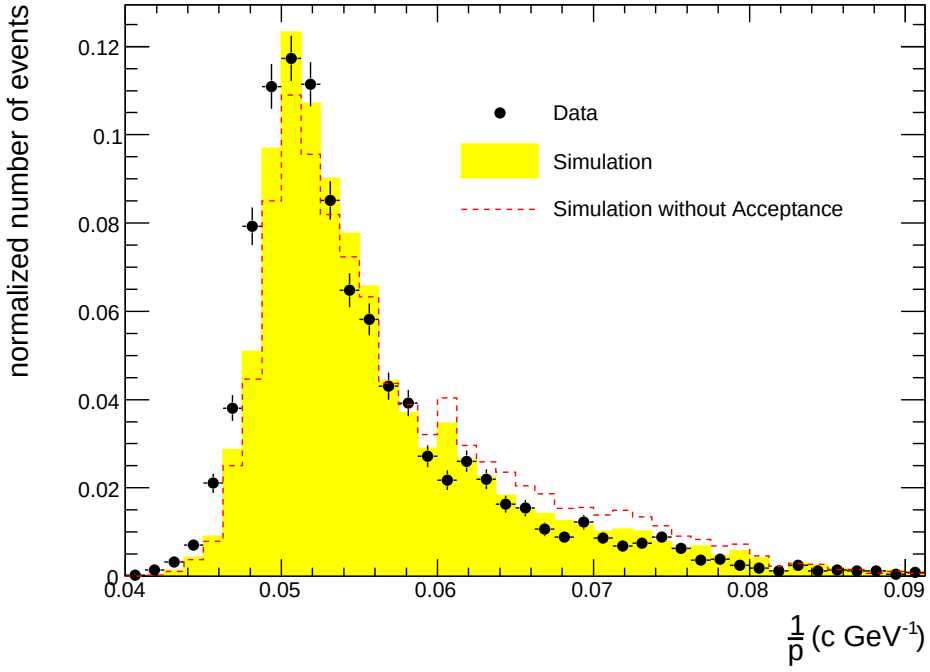

Figure 8. The distribution of $1/p$ measured with the silicon detector (3 pixel layers and 4 SCT layers) for a beam momentum of $p_{beam} = 20\,\mathrm{GeV/c}$. The solid circles are the data, the shaded area represents the simulation including the beam acceptance, the dashed line the simulation without the beam acceptance. The remaining discrepancy between the Monte Carlo simulation including the beam acceptance and the data comes from a slight misalignment of the Inner Detector.

improves whereas the relative beam spread is constant with beam momentum. In addition, the tails towards lower energies are larger in data than in the Monte Carlo simulation. The same behaviour has been found for runs of the CTB 2004 without magnetic field [14, 38]. The reason for this is that the beam line is not modeled in the Monte Carlo simulation and the beam line acceptance weighting does only approximate the effect of the beam line. In order to quantify this effect, the visible energy E_{Vis} distributions are fitted with Crystal Ball functions[12] and the *tail fraction* is defined as the fraction of events with a visible energy E_{Vis} below the mean $\mu_{E_{Vis}}$ of the fitted Crystal Ball function minus two standard deviations $\sigma_{E_{Vis}}$ of the fitted Crystal Ball function. The tail fraction for Monte Carlo simulation and data is shown in table 3 for all beam momenta. Note that for a Gaussian distribution the tail fraction would be 2.3%.

The ratio of the peak $\mu_{E_{Vis}^{data}}$ for the data and the peak $\mu_{E_{Vis}^{MC}}$ for the Monte Carlo simulation is shown in figure 11 for all beam momenta. The deviation of $\mu_{E_{calib}^{data}}/\mu_{E_{calib}^{MC}}$ from 1 is compatible with the energy scale uncertainty and the error bars. The main contributions to the error bars are the beam momentum uncertainty (data only) and the statistical errors.

[12]The definition of the Crystal Ball function is given in section 7.1, eq. (7.5).

2010 JINST 5 P11006

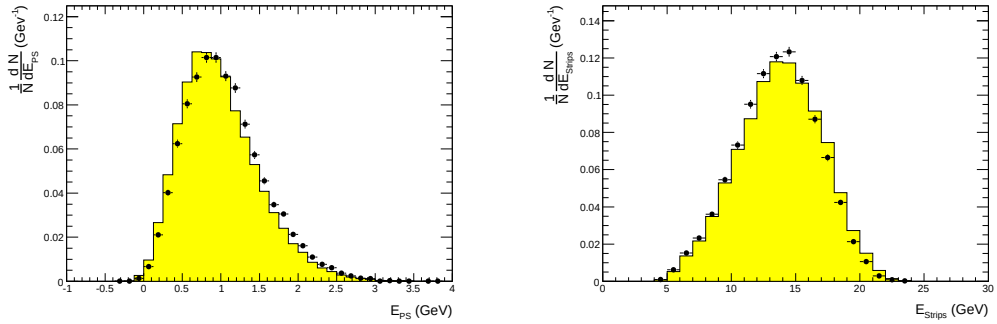

(a) Presampler (b) Strip layer

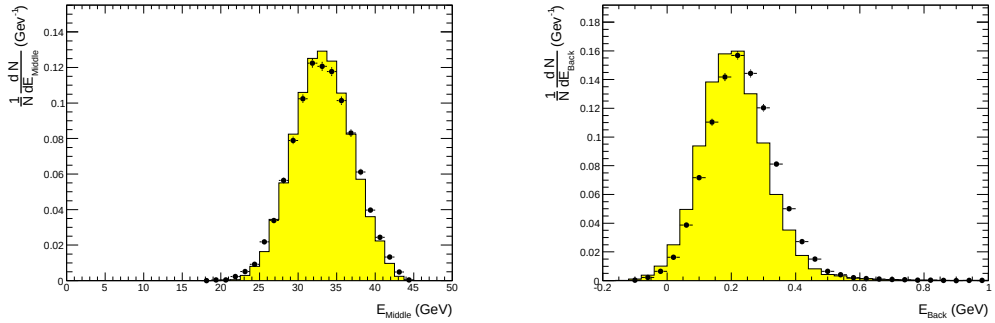

(c) Middle layer (d) Back layer

Figure 9. Energy deposit in all layers for $p_{beam} = 50\,\mathrm{GeV/c}$. Shaded area: Monte Carlo simulation; dots: data.

Table 3. Tail fraction (defined in the text) for Monte Carlo simulation and data for all beam momenta.

$p_{beam}^{nominal}$ (GeV/c)	Tail fraction Data (%)	Tail fraction Monte Carlo simulation (%)
20	16.0(6)	10.8(2)
50	16.0(3)	11.9(2)
80	16.2(5)	8.5(1)
100	14.4(3)	6.4(1)

3.4.3 Shower development

For the comparison of the longitudinal shower development two quantities are studied. Since in both quantities reconstructed energies appear in the numerator as well as in the denominator, they are independent of the global energy scale. The first quantity is the shower depth X_{mean} defined as the energy weighted average layer depth of all accordion layers by

$$X_{mean} = \frac{E_{Strips}X_{Strips} + E_{Middle}X_{Middle} + E_{Back}X_{Back}}{E_{Strips} + E_{Middle} + E_{Back}}, \tag{3.3}$$

2010 JINST 5 P11006

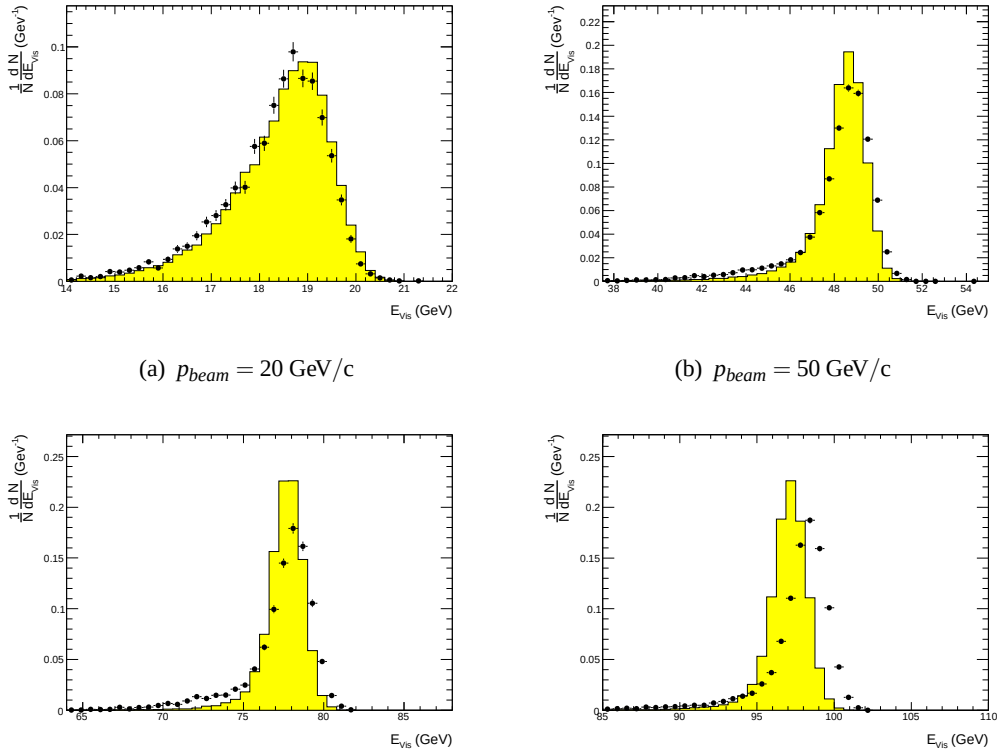

(a) $p_{beam} = 20$ GeV/c

(b) $p_{beam} = 50$ GeV/c

(c) $p_{beam} = 80$ GeV/c

(d) $p_{beam} = 100$ GeV/c

Figure 10. Total LAr EM calorimeter response E_{Vis} (sum of the accordion compartments plus presampler layer) for all beam momenta. Shaded area: Monte Carlo simulation; dots: data.

Table 4. LAr EMB layer boundaries and average depth at the beam impact point ($\eta = 0.442, \varphi = 0$).

Layer	X_{layer}^{start} (X_0)	X_{layer}^{stop} (X_0)	X_{layer} (X_0)
Presampler	1.50	1.78	1.64
Strips	2.18	6.41	4.29
Middle	6.41	25.02	15.71
Back	25.02	26.78	25.90

where $X_{Strips}, X_{Middle}, X_{Back}$ denote the average depth of the corresponding layer in units of radiation lengths (X_0) given in table 4. The Monte Carlo simulation to data comparison is shown in figure 12(a) for $p_{beam} = 50$ GeV/c. Again there is sufficiently good agreement, although the simulated showers tend to be shorter with respect to the data.

The second quantity for the longitudinal shower development is the ratio E_{strips}/E_{middle} of the energies of the strip and middle layers. This ratio is very sensitive to the amount of material in front of the calorimeter. Therefore it can be used to assess the level of accuracy of the material description in the simulation. The Monte Carlo simulation to data comparison is shown in figure 12(b) for $p_{beam} = 50$ GeV/c. The shape agreement is good. Again, the showers start earlier in the Monte

2010 JINST 5 P11006

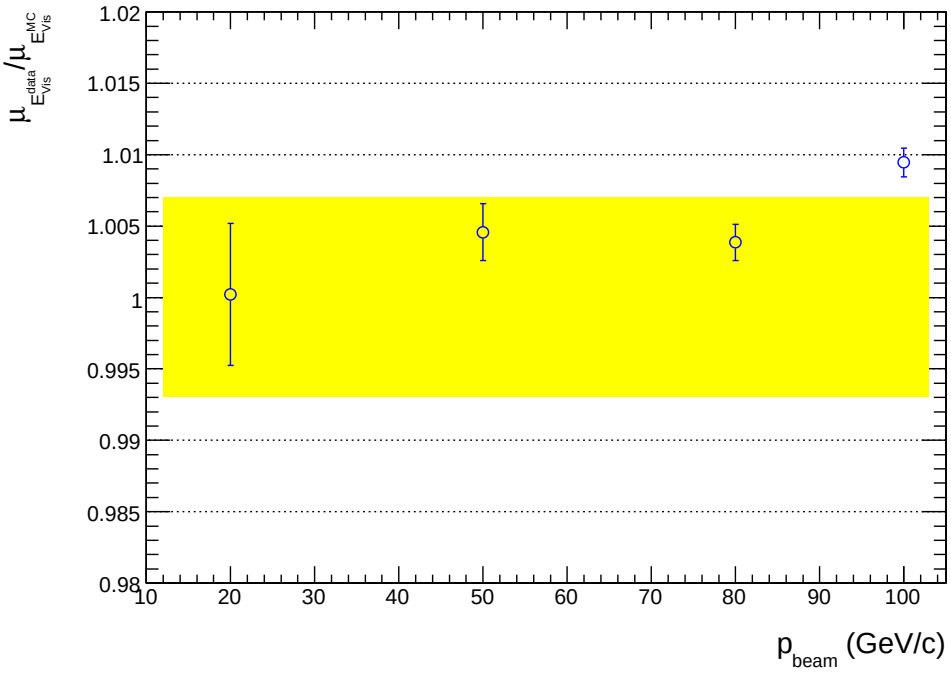

Figure 11. Ratio of the peak $\mu_{E_{Vis}^{data}}$ of the visible energy E_{Vis} for the data and the peak $\mu_{E_{Vis}^{MC}}$ of the visible energy E_{Vis} for the Monte Carlo simulation for all beam momenta. The shaded band represents the energy scale uncertainty for the data.

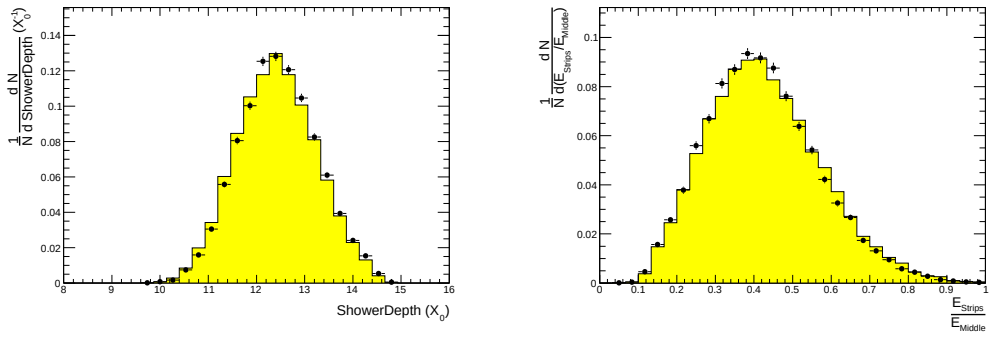

(a) Shower depth

(b) E_{strips}/E_{middle}

Figure 12. Shower depth (left) and the ratio between the energy deposit in the strips layer and in the middle layer (right) for $p_{beam} = 50$ GeV/c. Shaded area: Monte Carlo simulation; dots: data.

Carlo simulation than in data confirming the interpretation of the shower depth distribution in figure 12(a). The Monte Carlo simulation to data comparison for the mean of E_{strips}/E_{middle} for all beam momenta (figure 13) shows that the simulated showers tend to get shorter with respect to the data with increasing beam momentum.

2010 JINST 5 P11006

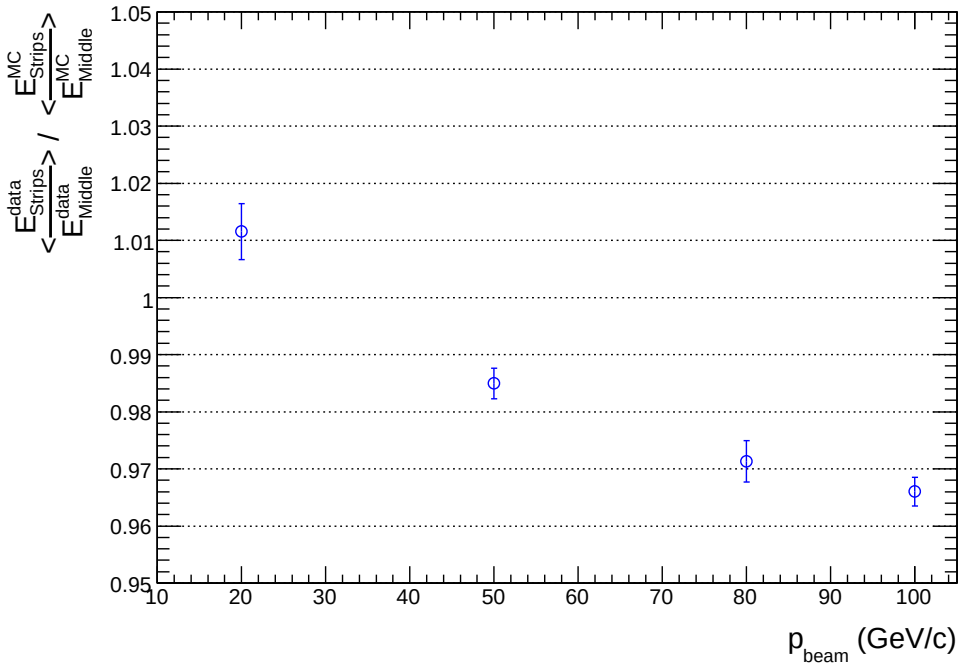

Figure 13. Ratio of the mean of the ratio between the energy deposit in the strips layer and in the middle layer $\left\langle \frac{E^{data}_{strips}}{E^{data}_{middle}} \right\rangle$ for the data and $\left\langle \frac{E^{MC}_{strips}}{E^{MC}_{middle}} \right\rangle$ for the Monte Carlo simulation for all beam momenta.

3.4.4 Systematic uncertainties

The level of accuracy of the Monte Carlo simulation description of the electromagnetic shower development in the LAr calorimeter is affected by uncertainties associated with the geometrical set-up and detector description (thickness of the lead absorbers, the depth of the first layer, the exact amount of material in front of the strip compartment, cables, electronics, the thickness of the cryostat and the amount of LAr in front of the presampler). Similar uncertainties will be an issue for the ATLAS detector at the LHC. Therefore, it is important to investigate them in the controlled test-beam environment. However, the uncertainties associated with the description of the combined test beam set-up itself will not be present in ATLAS. In order to understand the true systematic effects relevant to ATLAS, the combined test beam set-up-related uncertainties must be understood and a procedure developed to isolate them.

The dominant contributions of the total systematic uncertainty are

- Uncertainties in the knowledge of the beam momentum. Although the absolute beam momentum may include large errors, the relative momentum shifts between different nominal beam momenta are considerably smaller and depend on changes in beam conditions (collimator apertures, magnet currents, etc). Their total contribution is generally relatively small at the level of 0.1 % (0.2 % for a beam momentum of 20 GeV/c and below) [14].

- Simulation uncertainties in the description of the electromagnetic shower development by the simulation. Comparisons between `GEANT4.8` and `GEANT4.7` showed small differences

at the level of 1% in the lateral and longitudinal shower development because GEANT 4.8 features an improved description of multiple Coulomb scattering.

- Uncertainties in the Monte Carlo simulation description of the beam line and the description of the cryostat and the calorimeter. The impact of these contributions on the uncertainty of the reconstructed energy is smaller than 0.4 %. However, in terms of linearity, the listed effects have a much larger impact at lower energies than at higher energies; their impact on the linearity for momenta > 20 GeV/c is estimated to be less than 0.1 %. Most of them come from the limited precision of the measurement of some parameters like the beam-line geometry, detector geometry, cross-talk, etc. These uncertainties — except uncertainties of the beam-line description — will also be present for ATLAS and are therefore listed below:
  - Cross-talk in the strip compartment
  - M^{Phys}/M^{Cal} in the strip compartment (see subsection 3.3.1)
  - Cross-talk between the strip and middle compartments
  - Depth of the strip section (boundary between middle and strip compartment)
  - Lead absorber thickness
  - Monte Carlo simulation description of the presampler response
  - Upstream material in the beam line
  - Material in front of the presampler
  - Dead material between the presampler and the strip compartment
  - Simulation of charge collection
  - Monte Carlo simulation description of lateral and longitudinal shower shape

A detailed description of the systematic uncertainties can be found in [14].

3.5 The Calibration Hits Method

In the LAr calorimeter only energy deposits inside the active material of the calorimeter are measured. This implies that certain energy deposits are not measured directly. These are

1. Energy deposited outside the electromagnetic calorimeter: In the Monte Carlo simulation this energy is split into 3 contributions:
   - $E^{true}_{upstreamPS}$: Energy deposited upstream of the presampler, see section 3.5.2.
   - E^{true}_{PS-Acc}: Energy deposited between the presampler and the accordion, see section 3.5.2.
   - $E^{true}_{downstream}$: Energy deposited downstream of the accordion, see section 3.5.4.
2. Energy deposited inside the electromagnetic calorimeter, but outside of the reconstructed cluster: In order to minimize the noise contribution and to be able to measure the energies of several particles simultaneously, clusters of finite size are used for the energy measurement. However, the energy deposits in the calorimeter cells outside the cluster are not taken directly into account and therefore have to be estimated, see section 3.5.3.

2010 JINST 5 P11006

3. Energy deposited inside the reconstructed cluster in the inactive material: Because the LAr EMB calorimeter is a sampling calorimeter and the development and energy deposition of the electromagnetic cascade for an electron is a stochastic process, the ratio of the energy deposits in the active and passive material inside the cluster varies event-by-event and also as a function of the beam momentum. At 0^{th} order this ratio is approximated by a single factor, the *sampling fraction*, which is already applied at the cell reconstruction level. Higher order corrections are presented in subsection 3.5.3.

These energy deposits are recorded as additional hits in the simulation, therefore the name *Calibration Hits Method*.

The idea of this calibration procedure is to estimate these different kinds of energy deposits by means of Monte Carlo simulations and correlate them to measurable quantities, namely the measured cluster presampler energy E_{PS}, the measured cluster accordion energy E_{Acc} which is the sum of the strips, middle and back layer cluster energies,

$$E_{Acc} = E_{Strips} + E_{Middle} + E_{Back}, \tag{3.4}$$

or the shower depth X_{mean}. Therefore quantities for the different energy deposits are defined for each event. These quantities are binned with respect to the measurable quantity that is used to parameterize the energy deposits. For each bin a representative value is computed. Finally a fit to these extracted representative values is made in order to obtain the desired parameterization for the estimate.

The performance of the *Calibration Hits Method* for the Combined Test Beam 2004 for runs without magnetic field in the Inner Detector has already been discussed in [14, 38]. Therefore, the impact of the presence of the magnetic field in the Inner Detector on the performance of the *Calibration Hits Method* will be emphasized.

3.5.1 General strategy for the computation of representative values for distributions

The calibration of the electron energy is performed with respect to the peak position of the calibrated cluster energy. The reason for this choice is to minimize the effect of event selection cuts for physics analyses. These cuts mostly affect events in the tails of the various distributions and the dependence of peak values on these tails is the small. In order to be consistent, the peak position of a distribution is used to characterize its representative value throughout this section.

3.5.2 Estimation of the energy deposited upstream of the accordion

The energy deposited upstream of the accordion consists of the energy deposited upstream of the presampler $E^{true}_{upstreamPS}$, the energy deposited in the presampler E^{true}_{PS} and the energy deposited between the presampler and the accordion E^{true}_{PS-Acc}. For a given beam momentum the sum of these energies, denoted $E^{true}_{upstreamAcc}$ is estimated as a function of the measured presampler energy E_{PS}. For bins of E_{PS} covering the whole energy range of presampler energy measurements, the $E^{true}_{upstreamAcc}$ distributions are accumulated.

For each bin a fit with a Gaussian is performed around the peak and the mean of the Gaussian $\bar{E}^{true}_{upstreamAcc}$ is attributed to the measured presampler energy corresponding to the center of the bin. The resulting profile is plotted in figure 14 for $p_{beam} = 50$ GeV/c.

2010 JINST 5 P11006

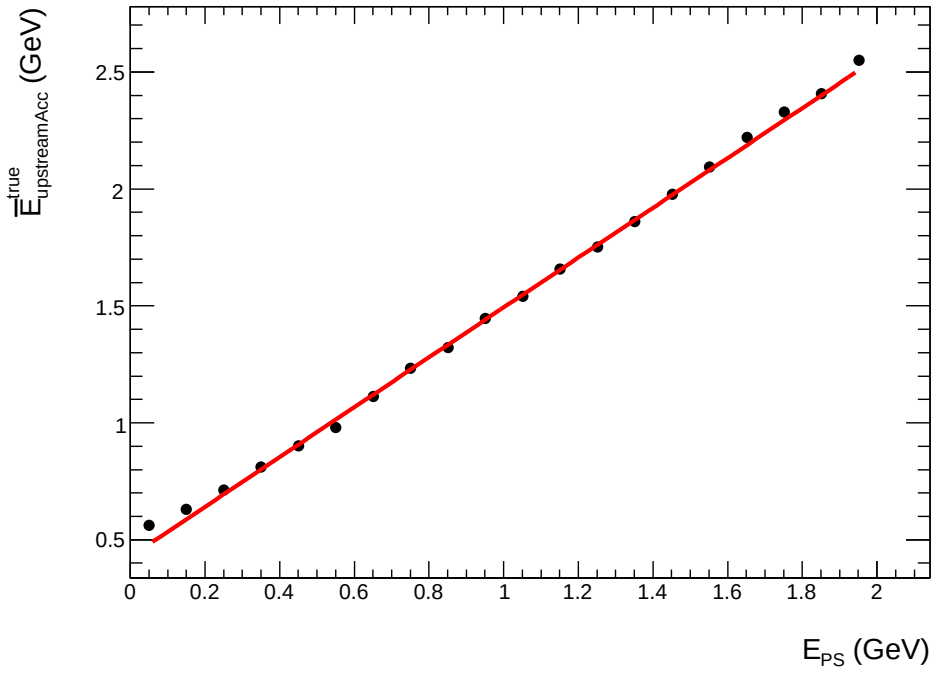

Figure 14. Energy deposited upstream of the accordion as a function of the reconstructed presampler energy for $p_{beam} = 50$ GeV/c. The error bars are within the disks.

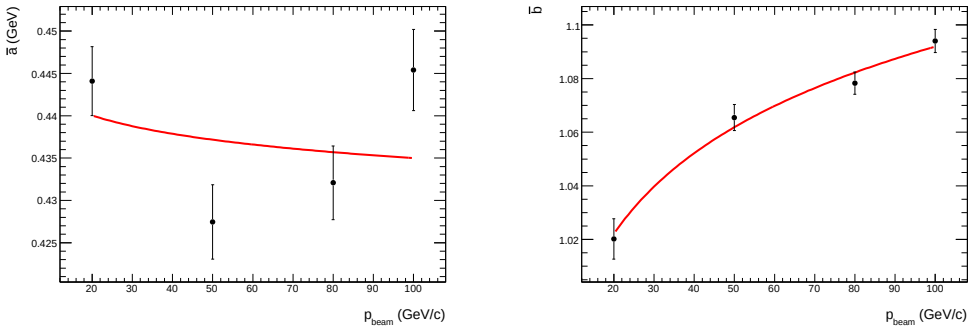

Figure 15. Offset (left) and slope (right) of the estimation of the energy deposited upstream of the accordion (eq. (3.5) and eq. (3.6)).

For each beam momentum a straight line is fitted. The obtained offsets $\bar{a}(p_{beam})$ and slopes $\bar{b}(p_{beam})$ are shown in figure 15. For the runs at the Combined Test Beam 2004 without magnetic field in the Inner Detector the offsets $\bar{a}(p_{beam})$ are a monotonously rising function of p_{beam} [38]. With magnetic field in the Inner Detector, the tracks of the particles with lower momentum are bent more strongly resulting in a smaller impact angle. This leads to an increase of the lengths of the tracks in the cryostat and therefore to an increase of $\bar{a}(p_{beam})$. As a consequence, the obtained offsets $\bar{a}(p_{beam})$ are a nearly constant function of p_{beam} within the errors.

2010 JINST 5 P11006

Next, the offset as a function of the beam momentum is parameterized by fitting

$$\hat{a}(p_{beam}) = a_0 + a_1 \log p_{beam}, \tag{3.5}$$

and the slope by fitting

$$\hat{b}(p_{beam}) = b_0 + b_1 \log p_{beam}, \tag{3.6}$$

with p_{beam} in units of GeV c^{-1} for the logarithms. These are the same parameterizations that have also been used for the runs without magnetic field in the Inner Detector. The slope is very well parameterized and the differences for the offset are at the level of 20 MeV. The fitted values are $a_0 = 0.45(1)$ GeV, $a_1 = -0.003(3)$ GeV, $b_0 = 0.89(2)$ GeV and $b_1 = 0.43(5)$ GeV.

Then for a given event at a given beam momentum the energy deposited upstream of the accordion is estimated by

$$E^{estim}_{upstreamAcc}(E_{PS}, p_{beam}) = \hat{a}(p_{beam}) + \hat{b}(p_{beam})\, E_{PS}. \tag{3.7}$$

In order to determine the particle energy without prior knowledge of the beam momentum, an iterative procedure is applied, see subsection 3.5.5.

3.5.3 Estimation of the energy deposited in the accordion

The energy E^{true}_{Acc} deposited in the accordion can be estimated either as a function of the shower depth or as a function of the beam momentum.

For each event the ratio d of the energy deposited in the accordion and the measured accordion energy (equation (3.4)) is defined by

$$d = \frac{E^{true}_{Acc}}{E_{Acc}}. \tag{3.8}$$

Beam momentum parameterization. For each beam momentum a Gaussian is fitted to the d distribution for the specific beam momentum and the mean of this Gaussian $\bar{d}(p_{beam})$ is extracted and shown in figure 16. Then $\bar{d}(p_{beam})$ is approximated by fitting

$$\hat{d}(p_{beam}) = d_0 + d_1 \log p_{beam} + d_2 \,(\log p_{beam})^2, \tag{3.9}$$

with p_{beam} in units of GeV c^{-1} for the logarithms. The fitted values are $d_0 = 1.262516(15)$, $d_1 = 0.107626(8)$ and $d_2 = 0.011840(1)$.

The values for $\bar{d}$ are close to one since a coarse sampling fraction correction is applied at the cell energy reconstruction ($F_{\mu A\to \mathrm{MeV}}$, see section 3.3.1). It increases with decreasing beam momentum because of two effects: The sampling fraction slightly decreases with decreasing beam momentum [39] and this is not taken into account by the coarse sampling fraction correction mentioned above. In addition, since the electrons are stronger deflected by the magnetic field with decreasing beam momentum, the emitted bremsstrahlung is more likely to be not contained in the cluster which increases the fraction of energy deposited outside the cluster with decreasing beam momentum.

For a given event at a given beam momentum the energy deposited in the accordion is estimated by

$$E^{estim}_{Acc}(E_{Acc}, p_{beam}) = \hat{d}(p_{beam})\, E_{Acc}. \tag{3.10}$$

In order to determine the particle energy without prior knowledge of the beam momentum, an iterative procedure is applied, see subsection 3.5.5.

2010 JINST 5 P11006

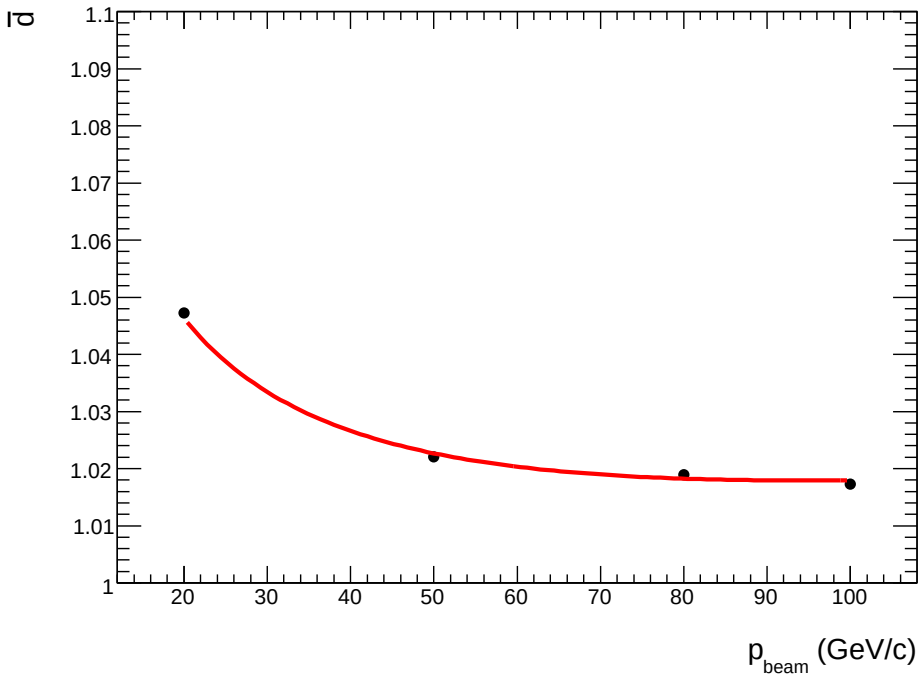

Figure 16. Mean $\bar{d}(p_{beam})$ of the Gaussian fitted to the d distribution (eq. (3.8)) for all beam momenta and its parameterization $\hat{d}(p_{beam})$. The error bars are within the disks.

Shower depth parameterization. The idea of this parameterization is to correct for sampling fraction fluctuations event by event by relating the sampling fraction to the shower depth. Analyses of CTB 2004 data have shown that this method works very well without magnetic field upstream of the calorimeter [14].

For bins of the measured shower depth X_{mean} covering the whole shower depth range, the d distributions are accumulated. For each bin a fit with a Gaussian is performed and the mean of the Gaussian $\bar{d}(X_{mean})$ is attributed to the measured shower depth corresponding to the center of the bin. The resulting profiles for all beam momenta are shown in figure 17.

Figure 17 demonstrates that the parameterization of $\bar{d}(X_{mean})$ as a function of the shower depth does not remove the dependence on the beam momentum. This is contrary to what has been found for the Combined Test Beam 2004 for runs without magnetic field in the Inner Detector [14, 38]. The reason for this discrepancy is that in the presence of the magnetic field the energy deposited inside the electromagnetic calorimeter but outside of the reconstructed cluster relative to the energy of the particle depends on the beam momentum. In figure 18 the mean $\bar{d}_{5x11}(p_{beam})$ dependence for clusters of 5×11 instead of 3×7 middle cells (section 3.3.2) is shown for all beam momenta. These clusters are large enough to contain the whole shower in the calorimeter. The fact that there is no beam momentum dependence for the 5×11 clusters indicates that the 3×7 cluster size together with the magnetic field generates the dependence of $\bar{d}(X_{mean})$ on the beam momentum. Therefore this parameterization is not used for the linearity and resolution measurements in section 3.6.

The same effect is also visible in ATLAS Monte Carlo simulation, although the effect there is

2010 JINST 5 P11006

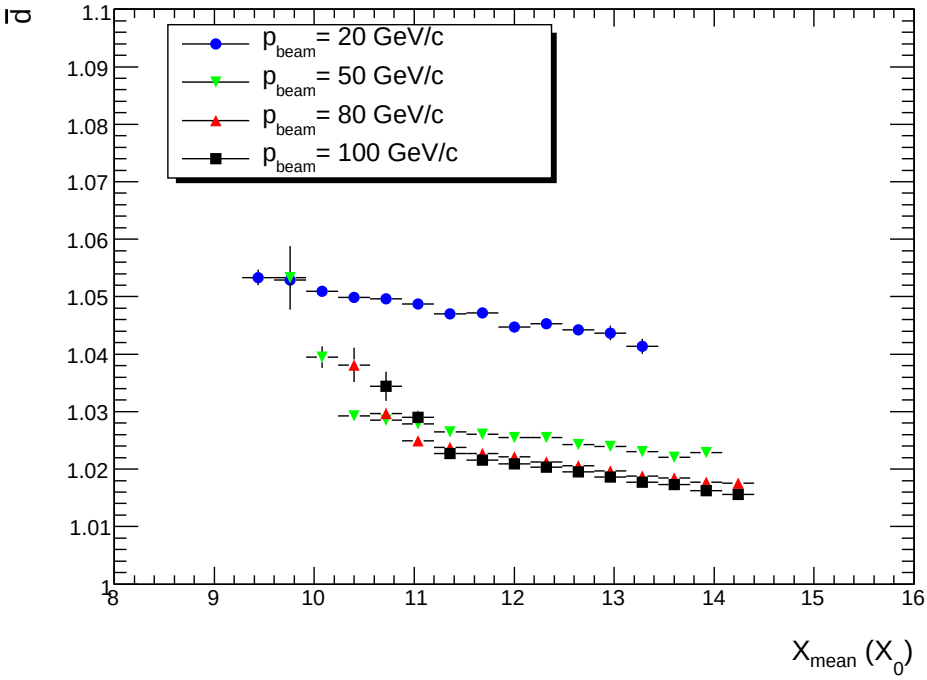

Figure 17. Mean $\bar{d}(p_{beam})$ of the Gaussian fitted to the d distribution (equation (3.8)) as a function of the shower depth X_{mean} for all beam momenta.

so small that the shower depth parameterization is used by default for the electron energy calibration [40]. The reason why this effect is much smaller for the ATLAS detector is that the geometric layout of the CTB 2004 is a bit different from ATLAS, in particular the distances between the inner detector components and the LAr EMB calorimeter are larger for the CTB 2004 setup.

3.5.4 Estimation of the energy deposited downstream of the accordion

The energy $E^{true}_{downstream}$ deposited downstream of the accordion can be estimated either as a function of the shower depth or as a function of the beam momentum.

Beam momentum parameterization. For each beam momentum a Gaussian is fitted to the $E^{true}_{downstream}$ distribution and the mean of the Gaussian $\bar{E}^{true}_{downstream}(p_{beam})$ is obtained and shown in figure 19. Then $\bar{E}^{true}_{downstream}(p_{beam})$ is approximated by fitting

$$E^{estim}_{downstream}(p_{beam}) = \lambda_0\, p_{beam} + \lambda_1\, p^2_{beam}. \tag{3.11}$$

The fitted values are $\lambda_0 = 9(4)\,10^{-4}$ c and $\lambda_1 = 2.3(7)\,10^{-6}\,c^2\,\mathrm{GeV}^{-1}$.

In order to determine the particle energy without prior knowledge of the beam momentum, an iterative procedure is applied, see section 3.5.5.

Shower depth parameterization. For each event the ratio of the energy deposited downstream of the accordion and the measured accordion energy which is the sum of the measured strips,

2010 JINST 5 P11006

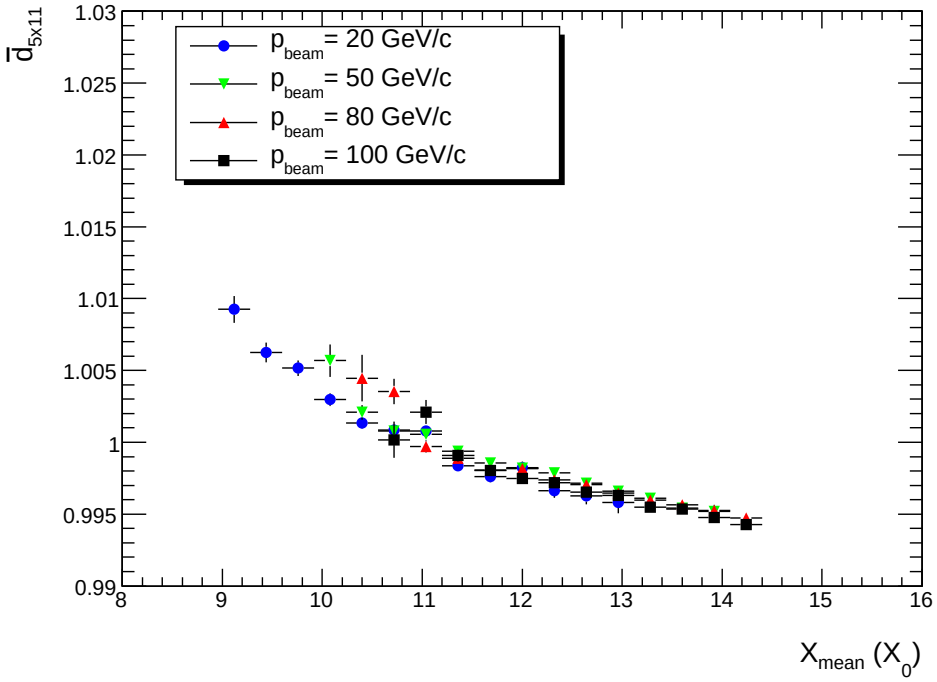

Figure 18. Mean $\bar{d}_{5x11}(p_{beam})$ of the Gaussian fitted to the d distribution (equation (3.8)) for 5×11 clusters as a function of the shower depth X_{mean} for all beam momenta.

middle and back layer energies is defined by

$$\lambda = \frac{E^{true}_{downstream}}{E_{Acc}}. \tag{3.12}$$

For bins of the measured shower depth X_{mean} covering the whole shower depth range, the λ distributions are accumulated. For each bin a fit with a Gaussian is performed and the mean of the Gaussian $\bar{\lambda}(X_{mean})$ is attributed to the measured shower depth corresponding to the center of the bin. The resulting profiles for all beam momenta are plotted in figure 20.

Figure 20 shows that the parameterization of the ratio of energy deposited downstream of the accordion and the measured accordion energy does not completely remove the dependence on the beam momentum. The remaining differences are at the half permille level.

For the reasons shown in section 3.5.3, this parameterization is not used for the linearity and resolution measurements in section 3.6.

3.5.5 Iterative procedure

An iterative procedure is applied to compute the calibrated cluster energy. Starting value for the estimate for the calibrated cluster energy is the visible energy. In each iteration step the estimated calibrated cluster energy from the previous step together with

$$E^2 = p^2 c^2 + m^2 c^4 \tag{3.13}$$

2010 JINST 5 P11006

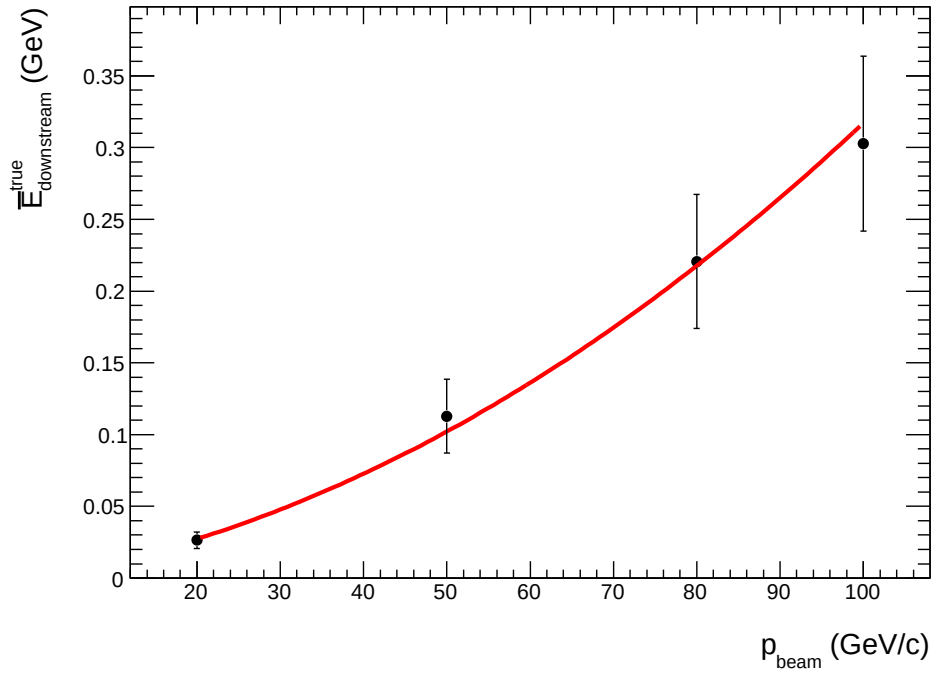

Figure 19. Mean of the energy deposited downstream of the accordion for all beam momenta and its parameterization $E^{estim}_{downstream}(p_{beam})$ (eq. (3.11)).

is used to estimate the proper beam/particle momentum to select the new estimation coefficients. Here the knowledge that electrons have been selected from the beam is used to justify the neglect of the rest mass term contribution to the particle energy.[13] The selected estimation coefficients are then used to compute a new estimate for the calibrated cluster energy.

Beam momentum parameterization. Using the beam momentum parameterizations for the energy E^{estim}_{Acc} deposited in the accordion and the energy $E^{estim}_{downstream}$ deposited downstream of the accordion, the iterative procedure is given by:

$$\begin{aligned}
E^0_{Calib} &= E_{PS} + E_{Acc} \\
p^0 &= \frac{E^0_{Calib}}{c} \\
&\vdots \\
E^k_{Calib} &= E^{estim}_{upstreamAcc}(E_{PS}, p^{k-1}) + E^{estim}_{Acc}(E_{Acc}, p^{k-1}) \\
&\quad + E^{estim}_{downstream}(p^{k-1}) \\
&= \hat{a}(p^{k-1}) + \hat{b}(p^{k-1})\,E_{PS} + \hat{d}(p^{k-1})\,E_{Acc} \\
&\quad + E^{estim}_{downstream}(p^{k-1}) \quad k > 0 \\
p^k &= \frac{E^k_{Calib}}{c} \quad k > 0
\end{aligned} \tag{3.14}$$

[13] The rest mass of an electron is $m_e = 511\,\mathrm{keV/c}$. The investigated beam momenta are $> 10\,\mathrm{GeV/c}$.

2010 JINST 5 P11006

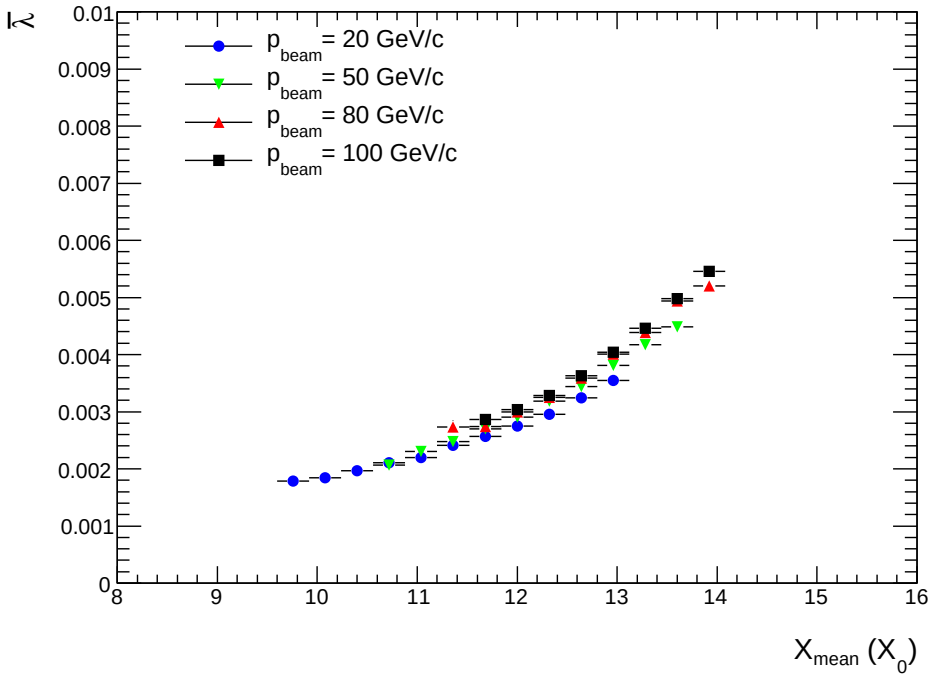

Figure 20. Mean $\bar{\lambda}(p_{beam})$ of the Gaussian fitted to the λ distribution (equation (3.12)) as a function of the shower depth X_{mean} for all beam momenta.

where p^k is the k-th estimation of the particle momentum and E^k_{Calib} is the k-th estimation of the particle energy. $E^{estim}_{upstreamAcc}(E_{PS}, p^{k-1}) = \hat{a}(p^{k-1}) + \hat{b}(p^{k-1})E_{PS}$ is used to estimate the energy deposited upstream of the accordion and $E^{estim}_{Acc}(E_{Acc}, p^{k-1}) = \hat{d}(p^{k-1})E_{Acc}$ to estimate the energy deposited in the accordion.

This iteration procedure is executed until the relative difference between the two consecutive E_{Calib} values $|E^k_{Calib} - E^{k-1}_{Calib}|$ is smaller than 10^{-6}. On average 3 iterations are required to meet this termination condition.

3.6 Linearity and resolution

The calibrated cluster energies are computed using the iteration scheme for the beam momentum parameterization (eq. (3.14)). The Monte Carlo simulation to data comparison is shown in figure 21 for all beam momenta. The shape agreement for calibrated cluster energy distributions is similar to the shape agreement for the visible energy distributions described in section 3.4.2. This means that the shape agreement is best at $p_{beam} = 20$ GeV/c and deteriorates with increasing beam momentum due to the beam spread that has not been simulated and due to low energy tails larger in data than in the Monte Carlo simulation. These low energy tails are mainly due to the fact that a priori the beam particles are simulated without taking into account any losses along the beam line. The correction introduced in section 3.4.1 only describes this effect in an approximate manner.

The calibrated cluster energy distributions are fitted with Crystal Ball functions[14] and the mean

[14]The definition of the Crystal Ball function is given in section 7.1, eq. (7.5).

2010 JINST 5 P11006

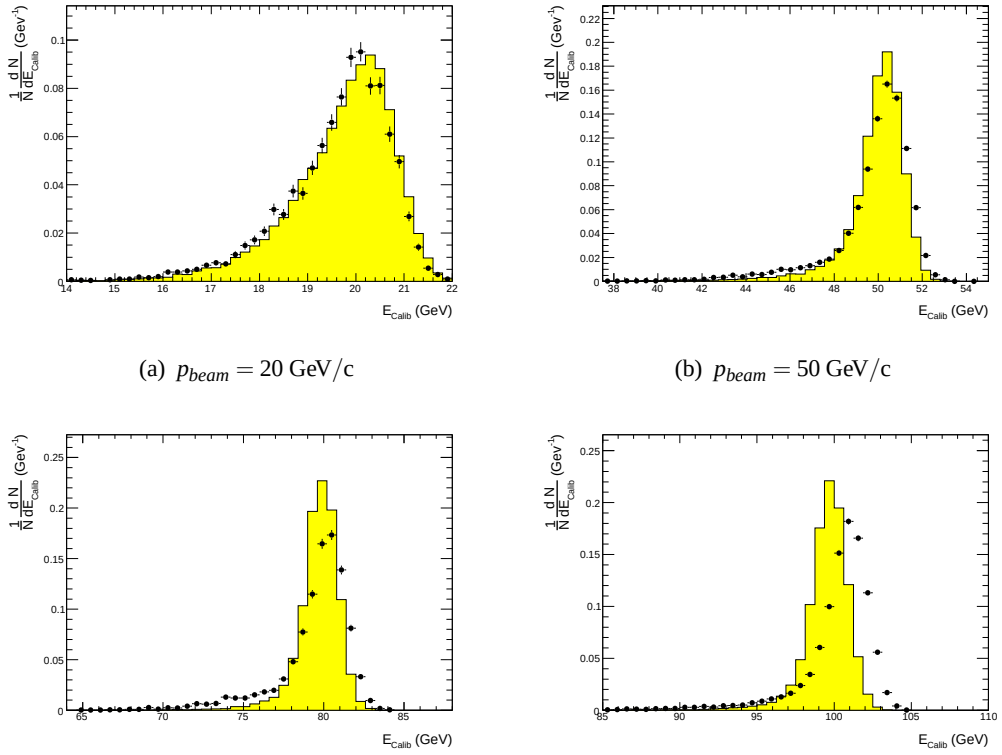

(a) $p_{beam} = 20$ GeV/c (b) $p_{beam} = 50$ GeV/c

(c) $p_{beam} = 80$ GeV/c (d) $p_{beam} = 100$ GeV/c

Figure 21. Calibrated energy for all beam momenta. Shaded area: Monte Carlo simulation; dots: data.

$\mu_{E_{calib}}$ and the sigma $\sigma_{E_{Calib}}$ of these Crystal Ball functions divided by $E_{beam} = p_{beam} \cdot c$ are plotted in figure 22 and figure 23 to assess the linearity and resolution.

In figure 22 the deviation of $\mu_{E_{calib}}/E_{beam}$ from 1 is within the energy scale uncertainty and the error bars. The main contributions to the errors bars are the beam momentum uncertainty (data only) and the statistical errors. The square root of the mean squared deviation of $\mu_{E_{calib}}/E_{beam}$ from 1 is 0.1% for the Monte Carlo simulation and 0.6% for the data. For the data this is within the energy scale uncertainty. Adjusting the energy scale, the linearity defined as the unbiased estimate of the standard deviation of $\mu_{E_{calib}}/E_{beam}$ is 0.1% for the Monte Carlo simulation and 0.28% for the data. This is within the estimated systematic uncertainties discussed in section 3.4.4. Therefore the linearity at the CTB 2004 is understood at the level of the estimated systematic uncertainties.

The resolution shown in figure 23 is described by

$$\frac{\sigma_{E_{Calib}}(E_{beam})}{E_{beam}} = \frac{a}{\sqrt{E_{beam}}} \oplus \frac{b}{E_{beam}} \oplus c \tag{3.15}$$

where the first term in the quadratic sum is the stochastic term, the second the noise term and the third the local constant term. Since the beam spread $\sigma(p_{beam})$ (table 1) was not simulated, it have been subtracted quadratically for every measurement point for Data in figure 23 before. In addition, since the noise of the read-out electronics was measured regularly during the whole

2010 JINST 5 P11006

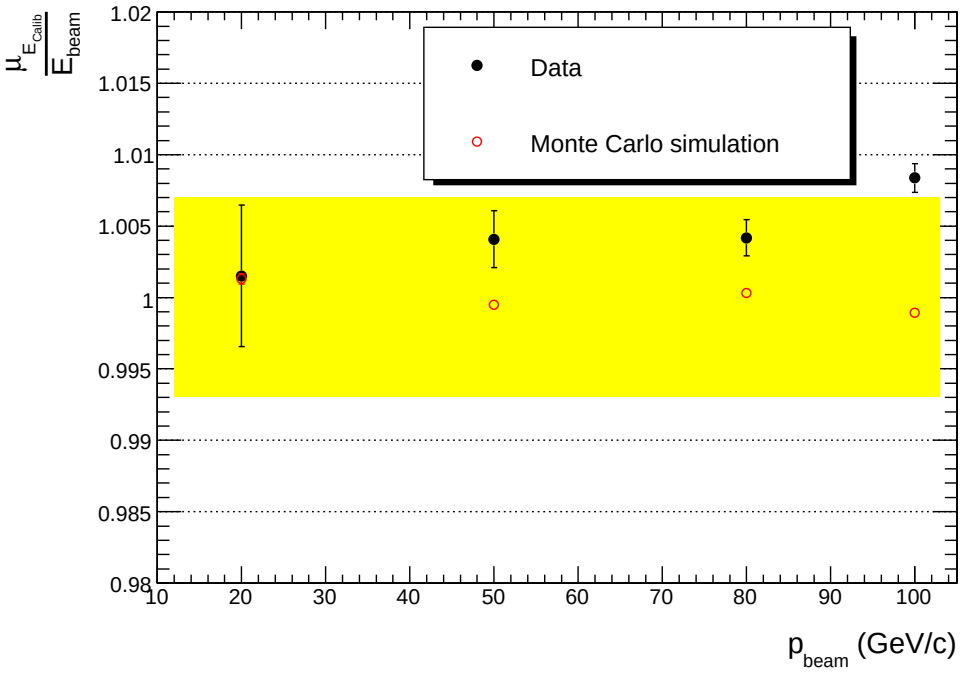

Figure 22. Linearity for Monte Carlo simulation and data. The shaded band representes the energy scale uncertainty for the data.

CTB 2004 data taking period by taking dedicated calibration runs, the noise values for the 3x7 clusters have also been subtracted quadratically for every measurement point for Data in figure 23 before. They have been computed for each run by averaging the noise values for the clusters over events that have been triggered randomly. The noise value of a given cluster was computed as the quadratic sum of the noise values of all cells in the cluster in their chosen read out gain for the given event. The noise value of a given cell in a given read out gain was taken from the previously mentioned calibration runs. The noise values are shown in table 5. The noise increases slightly with increasing beam momentum because more cells are read out in medium gain than in high gain due to the higher energy deposits and because the noise for the medium gain is higher than for the high gain. The reason for this difference in the noise values of a cell for the various gains is that the noise is first amplified with different gain factors but then digitized with a constant ADC resolution. Afterwards the gain dependent $F_{DAC\rightarrow\mu A} \cdot F_{\mu A\rightarrow \mathrm{MeV}}$ factor (see section 3.3.1) is applied to adjust the mean values of the noise distributions for the different gains. The net result of this procedure on the standard deviation of the noise distribution of a given cell which is the noise value of the given cell is the small gain dependence.

The error bars for the resolution shown in figure 23 are dominated by the systematic error of the fit of the calibrated cluster energy distributions from figure 21. The error bars have been estimated to be the difference of the standard deviations obtained with three different models: A Gaussian fitted to the peak part of the distribution, a Crystal Ball function fitted to the distribution and an exponential function convoluted with a Gaussian (defined by equation (7.3)) fitted to the distribution.

2010 JINST 5 P11006

Table 5. Noise values for the 3x7 clusters for all beam momenta.

Run number	$p_{beam}^{nominal}$ (GeV/c)	Noise (MeV)
2102399	100	209.7
2102400	50	207.4
2102413	20	207.4
2102452	80	207.9

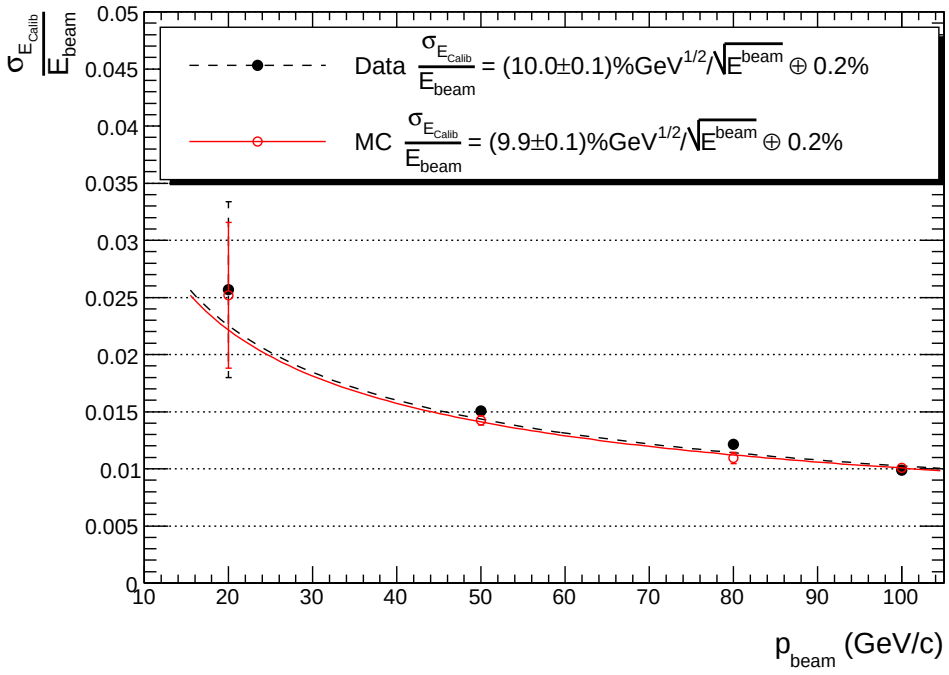

Figure 23. Relative energy resolution for Monte Carlo simulation and data for all beam momenta after subtraction of the beam spread and the noise. The error bars are dominated by the systematic error of the fit of the calibrated cluster energy distributions and are explained in the text.

The fit to extract a is done with $b = 0$ and $c = 0.2\%$ whose value is known from previous test beams. The value for a extracted by the fit is $(9.9 \pm 0.1)\%$ GeV$^{1/2}$ for Monte Carlo simulation and $(10.0 \pm 0.1)\%$ GeV$^{1/2}$ for data which is compatible with previous test beam results without magnetic field. It is the first measurement of a for the ATLAS LAr calorimeter with particles traversing a magnetic field similar as for ATLAS data taking at the LHC. However, the resolution for beam momenta of 50 GeV/c and 80 GeV/c is too small in the Monte Carlo simulation.

4 Momentum measurement with the Inner Detector

This section presents the performance of the momentum measurement for electrons with the ATLAS Inner Detector in the ATLAS Combined Test Beam 2004. The track reconstruction is

2010 JINST 5 P11006

described in section 4.1. This is followed by a comparison of the Monte Carlo simulation to data (section 4.2). The data samples and the event selection were the same as in section 3.

4.1 Track reconstruction

The track reconstruction algorithms for the CTB 2004 have been implemented in the CTB-Tracking ('Cosmics + TestBeam') package. This package provides a pattern recognition that works without a vertex constraint which is an ideal approach for the testbeam and is also needed for other situations, e.g. reconstructing cosmic or beam halo events. Details can be found in [41].

Tracks in the Inner Detector are reconstructed in three consecutive steps. In the pre-processing step, the raw data from the Pixel and SCT detectors are converted into clusters and the SCT clusters are then transformed into space-points. Furthermore, the TRT raw timing information is, based on a calibration obtained from data, first corrected for an offset with respect to the expected time of a signal for particles passing through the middle of the straw, and then the remaining delay caused by drift time is converted into a drift radius. At the track-finding step track candidates are identified using different tracking strategies. Fake tracks among these track candidates are rejected by applying quality cuts, e.g. on the number of associated clusters or the number of holes per track (a hole is defined as a silicon sensor crossed by a track without generating any associated cluster). The remaining track candidates are the reconstructed tracks for the given event. The track parameters are determined by global χ^2 minimization of the residuals (i.e. the difference between the measurement position and the position as predicted by the track), and their errors. During the final post-processing stage photon conversions and secondary vertices are reconstructed. At the CTB this final step is of minor importance except for photon conversion studies.

In a homogeneous magnetic field the sagitta of a curved track is directly proportional to $1/p$ and without bremsstrahlung events would be distributed like a Gaussian. The resolution of the inverse transverse momentum $1/p_T$ (which is equal to the inverse momentum in the CTB) can be expressed as a function of p_T:

$$\sigma_{1/p_T}(p_T) = \sigma_{1/p_T}(\infty) \left(1 \oplus \frac{p_T^X}{p_T}\right), \tag{4.1}$$

where $\sigma_{1/p_T}(\infty)$ is the asymptotic resolution expected at infinite momentum and p_T^X is a constant representing the value of p_T, for which the contribution of the intrinsic and multiple-scattering terms to the resolution are equal. Therefore the inverse momentum $1/p$ measured by the Inner Detector is used in section 4.2 to assess the quality of the description of the data by the Monte Carlo simulation. It is normalized to the beam momentum p_{beam}, i.e. p_{beam}/p is shown.

4.2 Monte Carlo simulation and comparison with data

The ratio p_{beam}/p of the beam momentum and the momentum measured by the Inner Detector is shown in figure 24 for all beam momenta and compared to Monte Carlo simulation.

The agreement of the description of the tails of the distribution is sufficiently good, but the scale agreement is not better than a few percent because of residual misalignment between the various Inner Detector components that could not be resolved [42].

2010 JINST 5 P11006

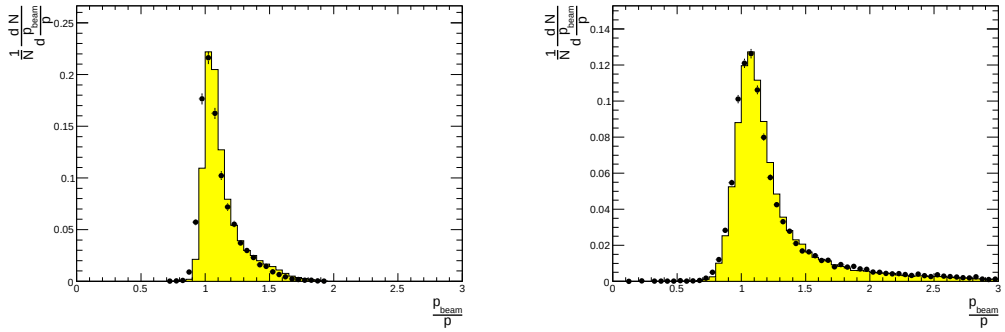

(a) $p_{beam} = 20$ GeV/c

(b) $p_{beam} = 50$ GeV/c

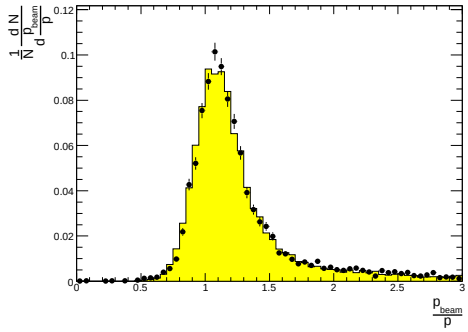

(c) $p_{beam} = 80$ GeV/c

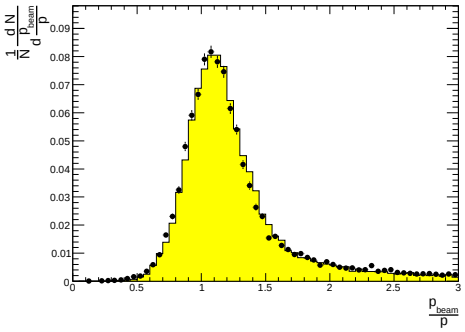

(d) $p_{beam} = 100$ GeV/c

Figure 24. Ratio p_{beam}/p of the beam momentum and the momentum measured by the Inner Detector for various beam momenta. Shaded area: Monte Carlo simulation; dots: data.

5 Particle identification with the Transition Radiation Tracker

This section presents the electron identification (ePID) with the TRT. After a short introduction to particle identification with the TRT in section 5.1, the data samples used for this analysis are discussed in section 5.2. Section 5.3 presents methods used for ePID in the TRT, and finally the measurement of the transition radiation onset from data is discussed in section 5.4.

5.1 Introduction to particle identification with the Transition Radiation Tracker

The TRT is a straw tube tracker with ePID capabilities mainly through detection of transition radiation photons created in the radiator between the straws. The detector is situated in front of the EM calorimeter and is described in detail in [3].

The output of the TRT is 27 bits per straw — 24 low threshold (LT) bits and 3 high threshold (HT) bit spanning 75ns. An illustration of a regular pulse along with its resulting bit output is shown in figure 25.

The number of HT hits are mainly the result of transition radiation (TR) photons, created when charged particles with high gamma factors pass the radiator material[15] between the straws.

[15] Material with rapidly changing dielectric constant (filt structure), creating TR through interference.

2010 JINST 5 P11006

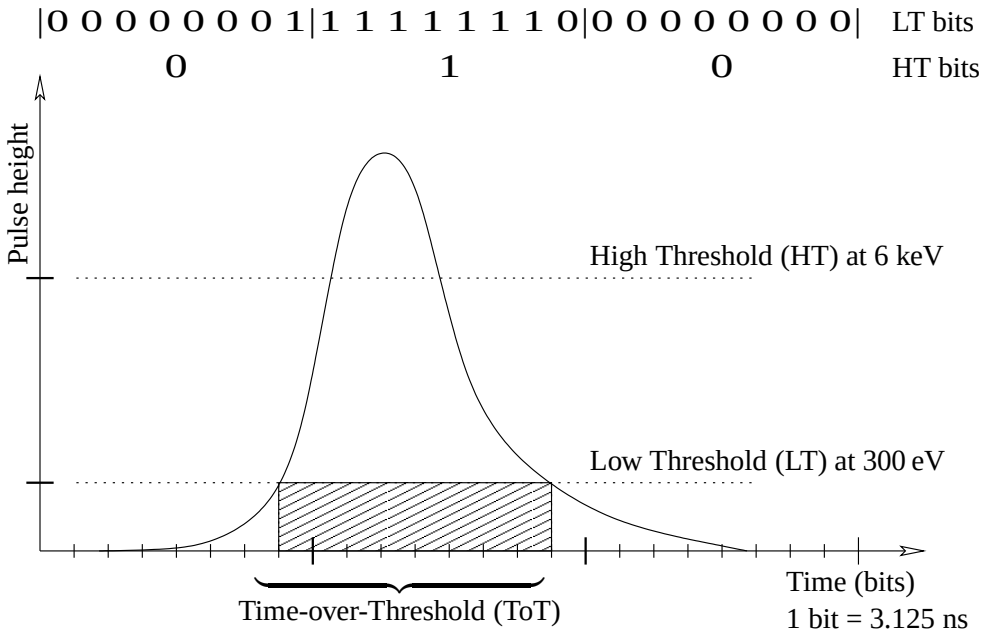

Figure 25. Example of a regular TRT pulse including its LT and HT bit response.

At the energies of the final state particles at LHC, essentially only electrons have such high gamma factors, and thus a HT hit signifies an electron.

The number of LT hits refers to the number of straw hits assigned to a specific track. In principle some straws could be crossed without a LT hit, but this fraction is very low, and will not have any significant influence on the results. For each LT hit, the number of bits set between the first bin (leading edge) and the last bin (trailing edge) yields the Time-over-Threshold (ToT). Since electrons ionize more than pions given a certain path length in the straw, a longer ToT signifies an electron. However, since the difference in dE/dx between electrons and pions vanishes at high energy, the ToT variable is expected to give better separation at low energy.

The separation between electrons and hadrons, mostly pions[16] presented in the following is based primarily on the HT information while the ToT information provides secondary separation most notably at lower energies. The optimization has been done to maximize the pion rejection (defined as $R_\pi = 1/\varepsilon_\pi$, where ε_π is the pion efficiency) at 90% electron efficiency.

The algorithm should also be efficient at finding (possibly soft) electrons in jets for b-quark tagging, which again requires good e/π separation. Here the TRT plays a central role.

5.2 The combined test beam data

5.2.1 Data samples

In order to get the best knowledge of the energy sensitivity of the e/π separation, the whole beam momentum range from 2 to 180 GeV/c was used. For each beam momentum, only runs without B-field and without additional material were used, though the results were not much affected by B-field and material. In addition, muon runs at 150 and 350 GeV/c were added to the data set

[16]Here and in the following, "pions" will be used as a generic word for "hadrons".

Table 6. Table showing all used runs, with their run-number, beam momentum in GeV/c, B-field in T, average number of LT hits, number of events N_{run}, number of events after selection N_{cuts} and numbers of pions, electrons, and muons (N_π, N_e, N_μ).

Run	$p_{beam}^{nominal}$ (GeV/c)	$B(T)$	⟨LT hits⟩	N_{run}	N_{cuts}	N_π	N_e	N_μ
2102115	2	0.00	36.38±0.03	50000	25105	3178	15755	157
2102098	3	0.00	37.17±0.03	50000	26873	5547	16684	0
2102097	5	0.00	37.41±0.03	50000	32316	12092	14190	0
2102103	9	0.00	37.44±0.02	50000	39649	14134	8369	113
2102397	20	0.00	32.83±0.02	50000	41500	2378	31817	271
2102410	50	0.00	33.75±0.02	50000	39815	6105	27254	12
2102454	80	0.00	34.38±0.02	50000	39156	6989	24891	33
2102398	100	0.00	33.89±0.02	40000	32031	8017	16520	509
2102433	150	0.16	36.10±0.02	27219	24683	414	0	21590
2102434	150	0.16	35.78±0.02	29486	26922	2919	0	21300
2102461	180	0.00	33.95±0.02	50000	44097	20683	6090	2439
2102730	350	0.16	35.42±0.01	50000	48589	61	0	46029
2102731	350	0.16	34.57±0.02	30494	29543	47	0	27932
2102728	350	1.40	34.57±0.02	46416	45098	62	0	42671

for the measurement of the TR onset (see section 5.4). These runs had non-zero B-field. During the data taking period two TRT geometry configurations were used, coinciding with the choice of beam momentum, such that at low beam energy (2, 3, 5, and 9 GeV/c) the lower three modules of the TRT were centered to the beam, while at high beam energy (20, 50, 80, 100, and 180 GeV/c) the three upper ones were aligned.

The complete list of runs used in this analysis, including their beam momentum p_{beam} in GeV/c, B-field in T, material status M, average number of LT hits, number of events in file N_{file} and after cuts N_{cuts}, and estimated statistics for each particle sample is presented in table 6.

5.2.2 Data quality

To ensure single high quality TRT tracks with no interference from other effects, events were required to have exactly one global track (i.e. a track seen and matched between the Pixel detector, the SCT, and the TRT) with at least 20 hits in the TRT. In addition a quality assurance is applied to each TRT straw, requiring that at least 100 identified electrons and pions passed through that straw, that the probability for an electron to make a HT hit (p_e^{HT}) is at least 50% higher than the same for a pion (p_π^{HT}), and that the latter is below 12.5% to avoid noisy straws. Straws that do not pass these cuts (6.1%) are removed from the track, and the requirement of at least 20 hits on track is repeated, excluding about 2% of the tracks.

5.2.3 Electron and pion samples

To obtain large clean samples of electrons and pions separately, a Cherenkov counter[17] and the ATLAS calorimeters were used for discrimination.

[17] This detector is only part of the CTB setup, not of the ATLAS detector.

Table 7. Electron and pion contaminations for the non-TRT separation requirements at beam momenta of 2, 3, 5, 9, 20, 50, 80, 100, and 180 GeV/c, respectively. An entry of 0.1×10^{-6} indicates that the contamination is at or below this level.

$p_{beam}^{nominal}$ (GeV/c)	2	3	5	9	20	50	80	100	180
e contamination in π sample (10^{-6})	8.4	2.1	0.2	0.1	0.1	0.1	0.1	0.1	0.1
π contamination in e sample (10^{-6})	17.1	9.5	4.1	0.1	0.1	1.4	1.9	1.9	0.2

The fraction of energy deposited in the first sampling and the entire cluster in the Liquid Argon calorimeter, provides very good separation. Additional information is provided by the Cherenkov counter at lower beam momenta (2-20 GeV/c) and the energy fraction in the Tile calorimeter at higher beam momenta (20-180 GeV/c). Finally, the muon system provides a muon tag, such that also clean samples of muons are available for the TR onset analysis.

The selections were obtained through an iterative process, where each variable is considered in turn, while applying the separating requirements to all the other detectors. This optimisation was performed at all beam energies, as most separation requirements are momentum dependent. For the study of the TRT ePID, reasonably large samples (> 1000 events) are needed, while at the same time good purities ($< 0.2\%$ contamination) are maintained. Generally, contaminations were much smaller, see table 7. It was checked that possible correlations would not affect the results significantly.

5.3 Particle identification methods

5.3.1 The high threshold method

The occurrence of a HT hit in a straw signifies transition radiation (TR), which, in the given momentum range, is essentially only emitted by electrons . However, HT hits can also be produced by other particles, mostly because of Landau fluctuations in the dE/dx and/or δ-rays (atomic electrons knocked out), which as a result decreases the separation. Given knowledge of the electron and pion HT hit probabilities, $p^e_{\mathrm{HT,i}}$ and $p^\pi_{\mathrm{HT,i}}$, these can be used to calculate the probability for a track to originate from an electron as follows:

$$p^e_{\mathrm{HT}} = \frac{\prod_i p^e_{\mathrm{HT,i}}}{\sum_{j=e,\pi} \prod_i p^j_{\mathrm{HT,i}}}, \tag{5.1}$$

where the product of probabilities is normalised to the probability of all possible particle types (in this analysis only pions and electrons). It has been checked that each straw can be considered an independent detector, and thus there is no correlation between straws.

The electron and pion HT hit probabilities used in the likelihood have been determined as averages for each straw and at each beam momentum. This method includes the variations with depth into the TRT observed. Also variations with distance from the track to the anode have been determined, but these are not used in the likelihood, as they are purely geometrical, and do not provide additional separation. An example of the HT distribution of likelihoods at 9 GeV/c is shown in figure 26.

2010 JINST 5 P11006

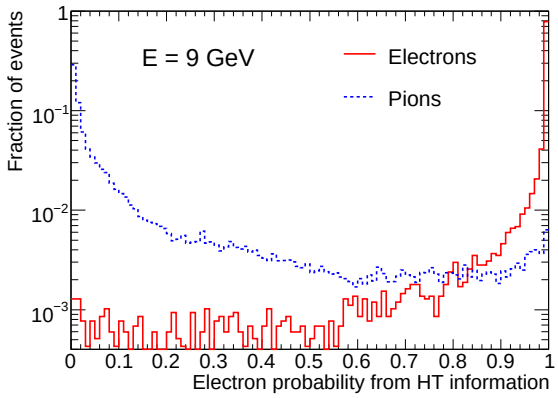

Figure 26. Distribution of likelihoods obtained from the HT information for electrons (solid) and pions (dashed) at 9 GeV/c.

Finally, the distribution of HT hits on the track (i.e. whether they occur randomly distributed or not) has been considered using the Wald-Wolfowitz run test [43]. No significant deviations from independent behavior was found.

5.3.2 The time-over-threshold method

In addition to the HT information, one can consider taking the ToT information into account as well, and especially at low momenta this is expected to increase the separation.

The ToT is very dependent on the distance r from the track to the anode (this is the information used by the tracking algorithms), and thus this geometrical effect has to be taken into account when considering the ToT for ePID. Also, while the ToT momentum dependence is not very pronounced for electrons, it does change with momentum for pions due to the stronger momentum dependence of dE/dx for pions. The larger the momentum, the closer dE/dx for pions gets to dE/dx of electrons, which thus in turn diminishes the separation between the two, using ToT information.

Given the ToT and the distance from the track to the anode r, a likelihood ratio similar to that of the HT is calculated as follows:

$$p^e_{\mathrm{ToT}} = \frac{\prod_{i,noHT} p^e_{\mathrm{ToT,i}}}{\sum_{j=e,\pi} \prod_{i,noHT} p^j_{\mathrm{ToT,i}}}, \tag{5.2}$$

wherein the product of probabilities is normalised to the probability of all possible particle types (pions and electrons). The probabilities p^e_{ToT} and p^π_{ToT} are determined as a function of ToT and r for each beam momentum averaged over all straws (to increase statistics).

Anticipating the combination of the HT and ToT information, the HT hits are excluded from the ToT likelihood to minimize the correlation between the two. It has been checked that the ToT information of the straws with HT hits do not carry any significant additional separation. An example of the distribution of likelihoods obtained with the ToT method not using HT hits at 9 GeV/c is shown in figure 27.

2010 JINST 5 P11006

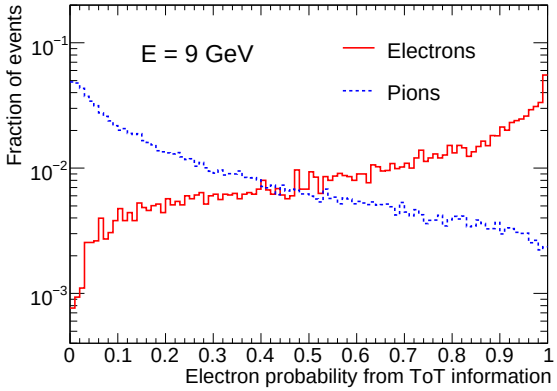

Figure 27. Distribution of likelihoods obtained from the ToT information for electrons (solid) and pions (dashed) at 9 GeV/c.

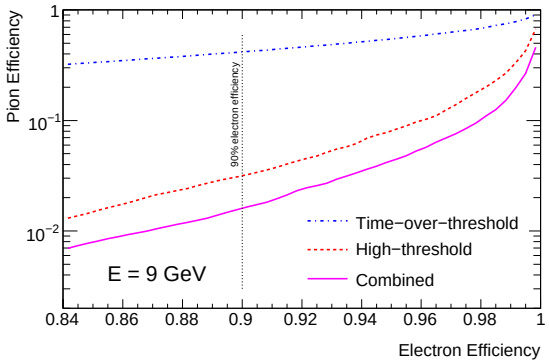

Figure 28. π-efficiency versus e-efficiency for ToT methods at 9 GeV/c.

5.3.3 Combined method

Having obtained separating methods using both the HT and the ToT information, a combination of these is considered to achieve the best pion rejection possible. It was checked that the correlation between the two were below 20% at all energies, and therefore the two variables are combined as follows:

$$p^e_{\text{all}} = \frac{p^e_{\text{HT}} p^e_{\text{ToT}}}{\sum_{j=e,\pi} p^j_{\text{HT}} p^j_{\text{ToT}}}. \tag{5.3}$$

The e/π separation performance resulting from this combination can be seen along with the separate HT and ToT performances in figure 28 at 9 GeV/c, which shows the π-efficiency as a function of e-efficiency. As can be seen from the figure, the HT information provides the bulk of the separation, while the ToT information gives a significant addition, as also seen in the combined performance, which is most performant.

2010 JINST 5 P11006

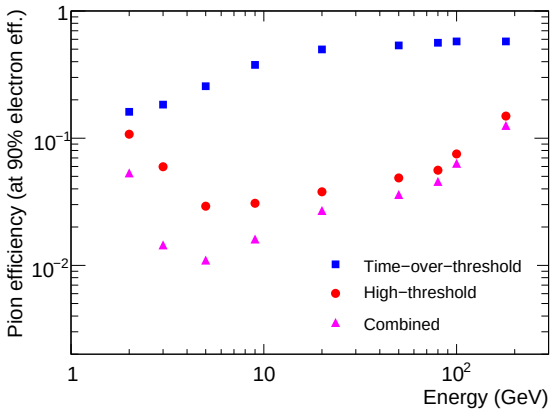

Figure 29. π-efficiency at 90% e-efficiency as a function of beam energy.

The algorithms for e/π separation were applied at all beam momenta, and using the pion efficiency at 90% electron efficiency (indicated by a vertical dashed black line in figure 28) as a figure of merit, the separation as a function of beam energy is shown in figure 29. As can be seen, the optimal e/π separation for the TRT is in the range 3-30 GeV/c, where it rejects more than 97% of pions while retaining 90% of electrons. The rejection is less outside this range, but still quite significant. The reason for this structure is related to the onset of TR for pions and electrons (see section 5.4). At low beam momentum the TR emittance of electrons has not reached its maximum yet, and at high beam momentum pions start to emit TR as well.

5.4 Measurement of the high threshold onset

Using the data and selection described in previous sections along with 5 muon runs at 150 and 350 GeV/c (see table 6), the TR dependence on the γ factor was measured. Since the TRT barrel radiator material is irregular, reliable calculations of the TR build-up are hard and need verification and/or tuning from data.

5.4.1 Procedure and error evaluation

For each run and particle type (π, e, μ) the HT probability was determined along with its (almost negligible) statistical error. These values were then combined into an average for each beam momentum and particle type, using the RMS between runs as a measure of the uncertainty due to variations in running conditions. The systematic error from the straw quality requirement is determined by applying two alternative selections, and the RMS of the variation is considered a systematic error.

At low γ factors (< 500), the HT probabilities are expected to be near constant (and low), since these probabilities are the result of the Landau tail of the dE/dx. However, due to the two different geometry configurations at low and high energy (see section 5.2), the HT probability changes and a correction has to be made. The correction is calculated by comparing the average HT probability (from 5 values) for pions and muons at low beam momenta (2-9 GeV/c) with that (from 3 values) at high beam momenta (20-50 GeV/c), where no change is expected. The averages $\langle p_{\mathrm{HT}}^{\pi+\mu}(\text{low } E)\rangle =$

2010 JINST 5 P11006

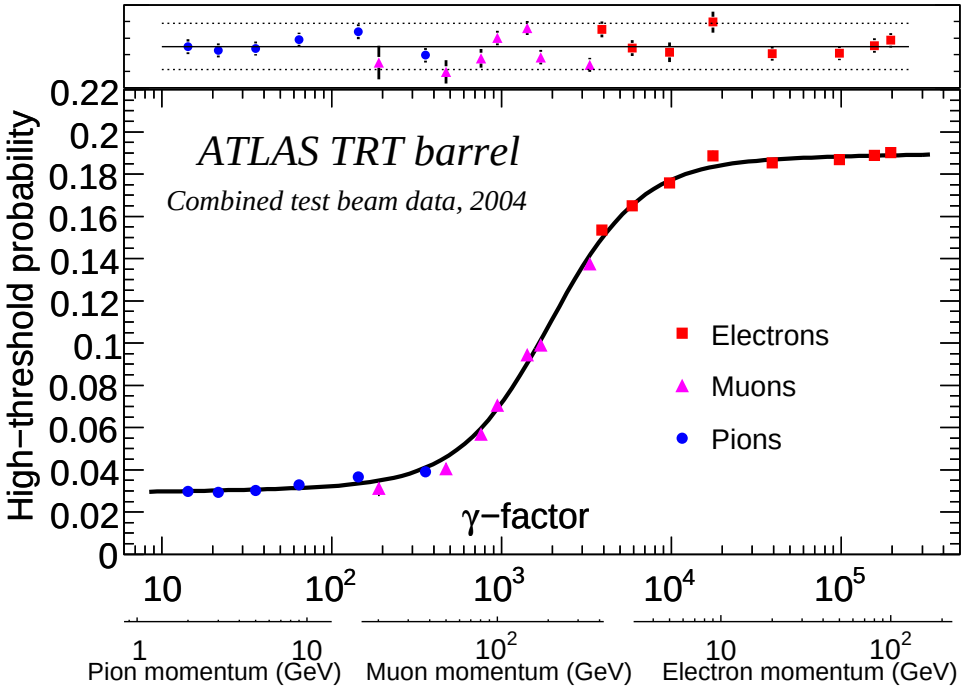

Figure 30. HT Probability as a function of γ factor for electrons (squares), muons (triangles) and pions (circles) in the beam energy range 2-350 GeV/c. The curve is a fit with a generic function, and the fit residuals are shown in the top plot, where the two dashed lines represent ± 0.005.

0.0402 and $\langle p_{\mathrm{HT}}^{\pi+\mu}(\text{high } E)\rangle = 0.0350$ compared to the overall average of $\langle p_{\mathrm{HT}}^{\pi+\mu}(\text{all } E)\rangle = 0.0383$ yield corrections of -0.0020 and 0.0033 at low and high beam momenta, respectively. Half of the corrections are used as a systematic error.

5.4.2 Results

The final values and their uncertainties are fitted with a generic function of $log_{10}\gamma$ consisting of a first degree polynomial and a sigmoid function:

$$p_{\mathrm{HT}}(\gamma) = c_0 + c_1 \log_{10}\gamma + \frac{c_2}{1.0 + \exp(-(\log_{10}\gamma - c_3)/c_4)} \tag{5.4}$$

with $\gamma \in [1, 500000]$. The result, along with the data points and the fitted function, can be seen in figure 30.

As figure 30 shows, the fit describes the data well. In γ regions in figure 30 where the values for the different particle types overlap, the HT probability does not seem to depend on the particle type, but only on the γ factor, as expected.

While the HT onset starts at about $\gamma \sim 1000$, it does not reach its maximum until $\gamma \sim 15000$. Likewise, even at high beam momenta pions do not emit much TR, and can thus be separated from electrons up to momenta of 150-200 GeV/c. Finally, and perhaps most importantly, this measurement enables a precise tuning of the TRT simulation.

2010 JINST 5 P11006

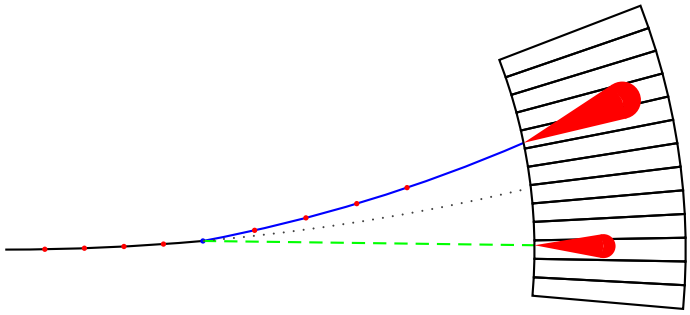

Figure 31. Sketch of an event with large bremsstrahlung emission. The solid line is the track of the electron, the dashed line the emitted bremsstrahlung photon and the dotted line the track of the electron if no bremsstrahlung had been emitted. The electromagnetic showers in the calorimeter are also shown. They are usually reconstructed in a single cluster except for large bremsstrahlung emission. The energy-weighted barycenter of the photon-electron system is the same as that of an electron without bremsstrahlung emission.

6 Bremsstrahlungs recovery using the Liquid Argon calorimeter

A common problem for a tracking detector in a magnetic field is that for electrons the emission of bremsstrahlung during the passage through the tracker might lead to an underestimation of the initial momentum of the electron.

The purpose of the presented algorithm, denoted bremsstrahlungs recovery, is to correct for momentum underestimation for electrons due to bremsstrahlung in the ATLAS Inner Detector using the electromagnetic calorimeter. At momenta lower than 20 GeV/c, the momentum underestimation can be corrected using only the Inner Detector hit pattern. Examples are DNA (Dynamic Noise Adjustment) [44] which is a Kalman fitter where the noise is adjusted to take the effects from bremsstrahlung emission into account and the Gaussian-Sum filter [45] where the Bethe-Heitler distribution of the bremsstrahlungs loss is modeled by a weighted sum of Gaussian distributions. At higher momenta, as the electron trajectory curvature is less pronounced, the combination of the Inner Detector information with that of the electromagnetic calorimeter is needed to correct the momentum underestimation.

The idea behind the bremsstrahlungs recovery with the electromagnetic calorimeter is based on the following: In the simplest case of single photon emission, the barycenter of the cluster of the photon and the one of the electron after bremsstrahlung in the calorimeter coincides with the position of the ideal electron without any bremsstrahlung activity. This is illustrated in figure 31. This observation holds true also for any number of photons as long as the energy deposits from the photons and electrons are fully reconstructed by the calorimeter cluster.

In ATLAS, given the standard size of the electromagnetic cluster ($\Delta\eta \times \Delta\phi = 3 \times 7$ in the LAr middle cell unit), most of the time the energy deposits for the photon and electron are collected in the same reconstructed cluster. In the standard ATLAS electron reconstruction a cluster and a track that geometrically matches this cluster are grouped together into an electron candidate object, therefore only one single cluster can be provided to the bremsstrahlungs recovery algorithm. In a dedicated electron reconstruction for the combined test-beam which allows more than one cluster to be associated with a track, the barycenter of the clusters can be used in the bremsstrahlung recovery algorithm.

2010 JINST 5 P11006

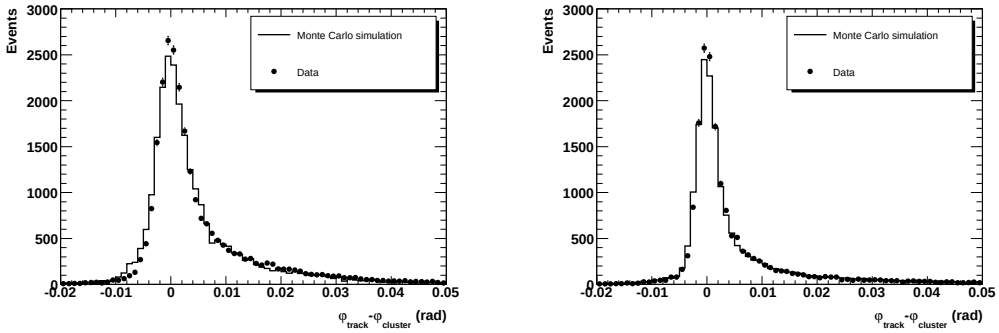

(a) $p_{beam} = 20\,\mathrm{GeV/c}$ (b) $p_{beam} = 50\,\mathrm{GeV/c}$

Figure 32. Distributions of $X_{Brem} = \varphi_{track} - \varphi_{cluster}$, i.e. the distance in φ between the extrapolated track and the calorimeter cluster, for various beam momenta.

In the CTB the Transition Radiation Tracker (TRT) is placed outside the magnet unlike in the ATLAS configuration. Therefore in the CTB only bremsstrahlung occurrences in the precision layers (Pixels and SCT) lead to momentum underestimation. The alignment between the electromagnetic calorimeter and the Inner Detector was crucial for this step and had to be adjusted following a dedicated study using pion tracks, i.e. particle tracks with negligible bremsstrahlung activity. In addition, while the Pixels and SCT modules alignment is final, the TRT has not been completely aligned. Consequently, only the tracks reconstructed exclusively from Pixel and SCT hits will be considered in this analysis.

Given a reconstructed track and cluster, the bremsstrahlungs recovery is implemented in the following way: A track hit is chosen as a hypothetical point of bremsstrahlung emission. Then the track hits in the track hit collection that are closer to the interaction vertex than the hypothetical point of bremsstrahlung emission are refitted. This refitted track is extrapolated to the calorimeter and its distance to the cluster is computed. This distance is minimized by varying the chosen hypothetical point of bremsstrahlung emission yielding the computed point of bremsstrahlung emission. Note that this stage the cluster position, itself a point in the three dimensional space, is used only as a reference to the refitted track extrapolation but not in the refitting procedure itself. If the computed point of bremsstrahlung emission is found to be either in the Pixel layers or in the first SCT layer, an additional step in the track fitting procedure is carried out in order to improve the tracking resolution: This additional track refit is performed on the combination of the hit collection of the track part close to the interaction vertex and the cluster position. Finally, the refitted track associated with the computed point of bremsstrahlung emission is used to estimate the inverse momentum of the initial electron.

6.1 Results with combined test beam data

The data samples used in the analysis are from run 2102446 for $p_{beam} = 20\,\mathrm{GeV/c}$ and from run 2102400 for $p_{beam} = 50\,\mathrm{GeV/c}$.

The performance of the bremsstrahlungs recovery algorithm is investigated for different samples of events. First, samples of events with large bremsstrahlung emission are discussed. Next,

2010 JINST 5 P11006

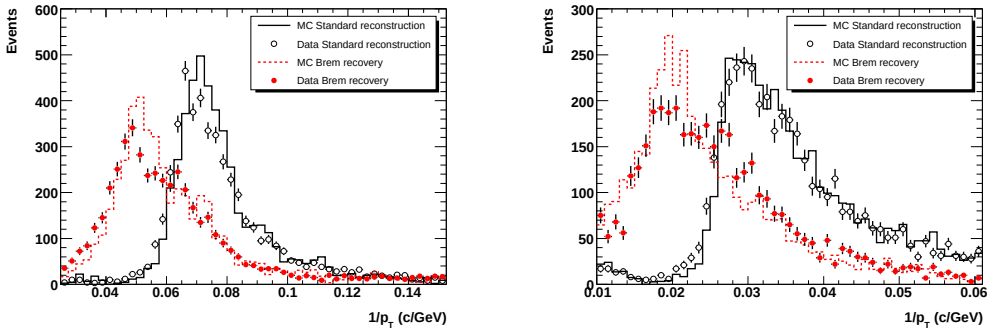

(a) $p_{beam} = 20\,\mathrm{GeV/c}$ (b) $p_{beam} = 50\,\mathrm{GeV/c}$

Figure 33. Distributions of reconstructed and corrected $1/p_T$ for large X_{Brem} events for various beam momenta.

the performance is evaluated on samples of events with more than one reconstructed cluster in the calorimeter. Finally, the performance of the bremsstrahlungs recovery algorithm is discussed for all events.

The detailed comparisons with CTB data necessitates a measure of bremsstrahlung activity applicable to both, data and Monte Carlo simulation. A natural quantity is the distance in φ between the extrapolated track and the calorimeter cluster, denoted $X_{Brem} = \varphi_{track} - \varphi_{cluster}$. The cluster position is relatively stable under bremsstrahlung (it usually collects most of the energy of the photon and electron showers) while the track curvature becomes more pronounced in the case of energy loss due to bremsstrahlung. A larger X_{Brem} means larger bremsstrahlung activity in the Inner Detector. Figure 32 shows the distribution of X_{Brem} for $p_{beam} = 20\,\mathrm{GeV/c}$ and $p_{beam} = 50\,\mathrm{GeV/c}$ with the characteristic long asymmetric tails due to bremsstrahlung.

In order to investigate the impact of the bremsstrahlungs recovery algorithm on events with large bremsstrahlung emission, the 12% of events with largest X_{Brem} are selected and denoted *large* X_{Brem} events. For $p_{beam} = 20\,\mathrm{GeV/c}$ the corresponding cut is $X_{Brem} \geq 10\,\mathrm{mrad}$ and for $p_{beam} = 50\,\mathrm{GeV/c}$ the corresponding cut is $X_{Brem} \geq 5\,\mathrm{mrad}$. Figure 33 shows the distributions of $1/p_T$ before and after bremsstrahlungs recovery for large X_{Brem} events.

For large X_{Brem} events the position of the peak of the reconstructed $1/p_T$ distribution using the standard reconstruction is closely related to the X_{Brem} cut. The magnet used in the combined test-beam had a bending power of 1.52 Tm. Without bremsstrahlung, a $p_{beam} = 50\,\mathrm{GeV/c}$ electron is bent in φ by 9.1 mrad after crossing the Inner Detector. For an X_{Brem} value of 5 mrad and assuming that the cluster collects all the energy which means that the $\varphi_{cluster}$ is the same as without bremsstrahlung, φ_{track} is actually 14.1 mrad. This corresponds to a reconstructed $1/p_T$ of about $0.03\,\mathrm{GeV^{-1}c}$ as shown by the peak in the reconstructed $1/p_T$ distribution for p_{beam}=50 GeV/c for the standard reconstruction in figure 33(b). With bremsstrahlung recovery, the $1/p_T$ peak is around $0.02\,\mathrm{GeV^{-1}c}$ as expected.

For a low momentum beam like $p_{beam} = 20\,\mathrm{GeV/c}$, if the bremsstrahlung occurs strongly and early enough, the electron will be sufficiently bent by the magnetic field so that its cluster and that of the photon are reconstructed separately in the calorimeter. Figure 34 shows the distribution of

2010 JINST 5 P11006

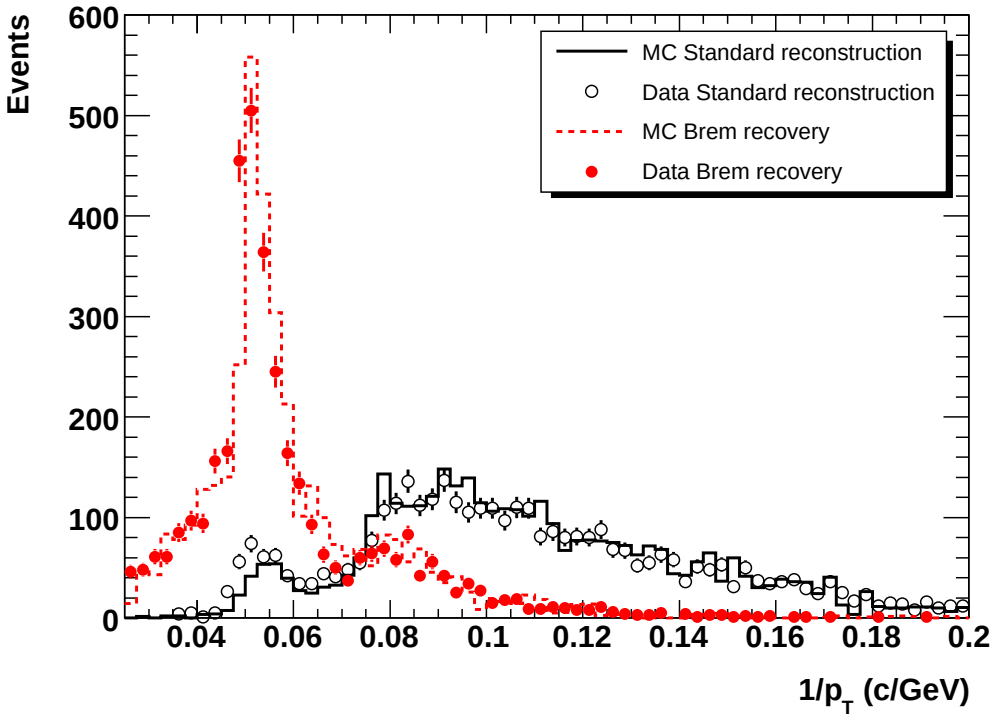

Figure 34. Distributions of reconstructed and corrected $1/p_T$ for $p_{beam} = 20\,\mathrm{GeV/c}$ for events with at least 2 reconstructed clusters.

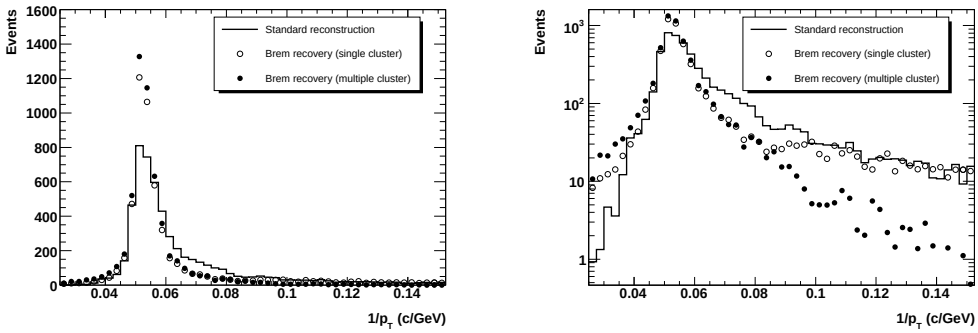

(a) (b) log scale

Figure 35. Distributions of $1/p_T$ for the standard reconstruction, for the reconstruction with bremsstrahlungs recovery using a single cluster and for the reconstruction with bremsstrahlungs recovery using a combination of multiple clusters for Monte Carlo simulation for $p_{beam} = 20\,\mathrm{GeV/c}$.

$1/p_T$ before and after bremsstrahlungs recovery for events having at least two reconstructed 3×7 clusters for $p_{beam} = 20\,\mathrm{GeV/c}$. The reconstructed $1/p_T$ exhibits a double-peak structure. The small peak around $0.05\,\mathrm{GeV}^{-1}\mathrm{c}$ represents events that do not have significant bremsstrahlung and the second cluster is made essentially of noise. The fraction of these events is quite small, about

2010 JINST 5 P11006

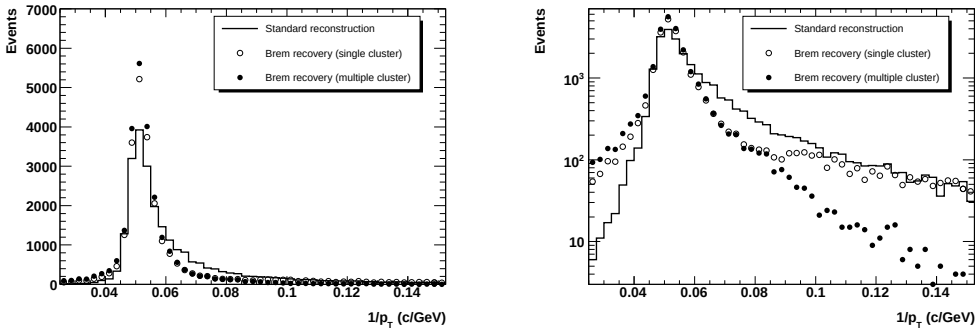

(a) (b) log scale

Figure 36. Distributions of $1/p_T$ for the standard reconstruction, for the reconstruction with bremsstrahlungs recovery using a single cluster and for the reconstruction with bremsstrahlungs recovery using a combination of multiple clusters for data for $p_{beam} = 20\,\mathrm{GeV/c}$.

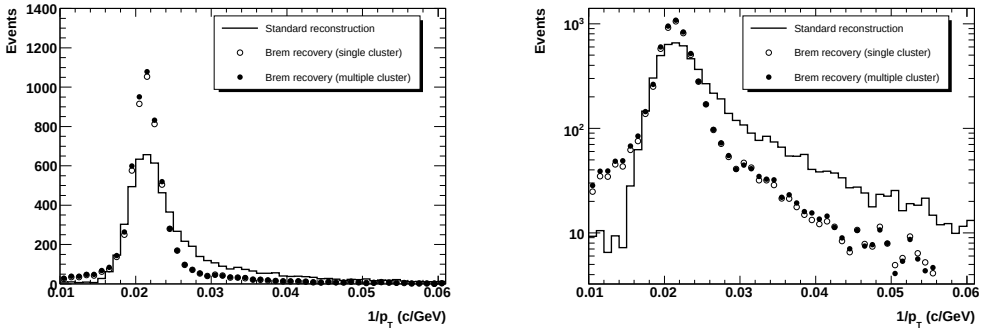

(a) (b) log scale

Figure 37. Distributions of $1/p_T$ for the standard reconstruction, for the reconstruction with bremsstrahlungs recovery using a single cluster and for the reconstruction with bremsstrahlungs recovery using a combination of multiple clusters for Monte Carlo simulation for $p_{beam} = 50\,\mathrm{GeV/c}$.

Table 8. Tail fractions of $1/p_T$ before and after the bremsstrahlung correction using a single cluster or a combination of multiple clusters. The quoted errors are statistical only.

$p_{beam}^{nominal}$ (GeV/c)	Sample	Tail fraction Standard reconstruction	Tail fraction Brem recovery (single cluster)	Tail fraction Brem recovery (multiple clusters)
20 GeV/c	Data	0.090 ± 0.001	0.078 ± 0.001	0.012 ± 0.000
	Monte Carlo	0.098 ± 0.001	0.093 ± 0.001	0.015 ± 0.000
50 GeV/c	Data	0.091 ± 0.001	0.034 ± 0.000	0.034 ± 0.000
	Monte Carlo	0.097 ± 0.001	0.031 ± 0.000	0.028 ± 0.000

300 events in 40,000 events in total. The much broader peak around $0.09\,\mathrm{GeV}^{-1}\mathrm{c}$ represents events with bremsstrahlung carrying around 50% of the original electron energy. It can be seen clearly

2010 JINST 5 P11006

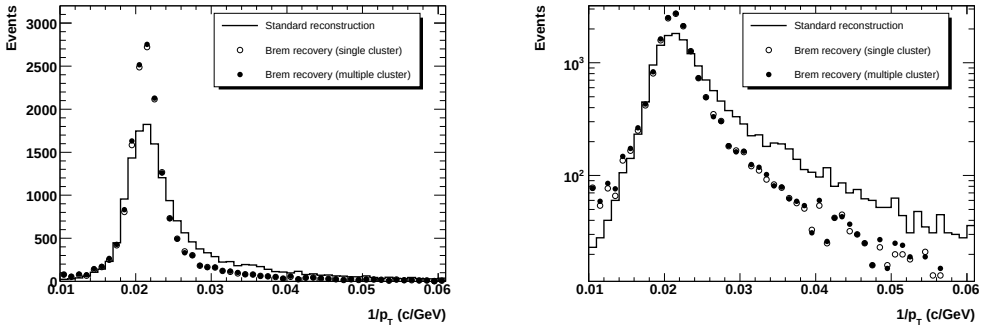

(a) (b) log scale

Figure 38. Distributions of $1/p_T$ for the standard reconstruction, for the reconstruction with bremsstrahlungs recovery using a single cluster and for the reconstruction with bremsstrahlungs recovery using a combination of multiple clusters for data for $p_{beam} = 50\,\mathrm{GeV/c}$.

that the correction permits to recover the original electron energy.

Overall, in both cases of large X_{Brem} and multiple cluster events, there is a good agreement to the level of $1-2\%$ between the data and the Monte Carlo simulation.

Figure 35, figure 36, figure 37 and figure 38 show the distribution of $1/p_T$ before and after bremsstrahlungs recovery for all electrons. The bremsstrahlungs recovery is performed by using the single $\Delta\eta \times \Delta\phi = 3 \times 7$ cluster matching to the original track and by combining multiple 3×7 clusters. These figures show that the bremsstrahlungs recovery reduces the tails of the $1/p_T$ distributions significantly, for the Monte Carlo simulation as well as for the data. In addition, for $p_{beam} = 20\,\mathrm{GeV/c}$ the combination of multiple calorimeter clusters decreases the tails compared to the single cluster method because for events with large bremsstrahlung emission the energy deposition for the photon may not be sufficiently contained in the single cluster associated with the electron. Therefore the position of the single cluster is far from the barycenter of the combination of the cluster of the photon and the one of the electron yielding a performance of the single cluster method comparable to the standard reconstruction for events with large bremsstrahlung emission.

In order to quantify the recovery power, a new figure of merit, the *tail fraction*, is introduced. It is defined as the fraction of events with $1/p_T$ above twice the nominal beam momentum value, i.e. $> 2/p_{T,beam}^{nominal}$. The tail fractions before and after the bremsstrahlung correction using single or multiple 3×7 clusters for $p_{beam} = 20\,\mathrm{GeV/c}$ and $p_{beam} = 50\,\mathrm{GeV/c}$ are summarized in table 8 demonstrating the improvements due to the bremsstrahlungs recovery algorithm.

7 Intercalibration with E/p

This section presents a method to intercalibrate the energy scale of the electromagnetic calorimeter and the momentum scale of the Inner Detector. The intercalibration is performed by investigating the ratio E/p for electrons, i.e. the ratio of the energy E measured by the electromagnetic calorimeter and the momentum p measured by the Inner Detector.

2010 JINST 5 P11006

Ideally the ratio E/p is expected to be 1 (in units of c) for relativistic electrons measured by the Inner Detector and the electromagnetic calorimeter. However, due to the fact that each of the detectors has its intrinsic measurement resolution, in reality the ratio E/p will be a distribution that depends strongly on the detector response functions (and their correlation) of the Inner Detector and the electromagnetic calorimeter.

The key concept of this intercalibration method is to extract information for the detector response functions, such as e.g. their scale, of the electromagnetic calorimeter, i.e. E/p_{beam}, and of the Inner Detector, i.e. p_{beam}/p, from a fit to the E/p distribution. In order to be able to achieve this, the E/p distribution has to be parameterized through the two individual detector response functions E/p_{beam} and p_{beam}/p. Since E/p_{beam} and p_{beam}/p describe not necessarily uncorrelated random variables, their correlation also has to be taken into account for the E/p parameterization. Since the knowledge of the true momentum of the particles, i.e. p_{beam}, is necessary to obtain a description of this correlation and this knowledge will not be available for ATLAS, the correlation is computed for Monte Carlo simulation.

The E/p parameterization is fitted to the observed E/p distribution and since it is built upon the individual detector response functions, the fit parameters obtained from the E/p fit reflect the properties of the individual response functions. This section is devoted to the extraction of the relative scale of the two individual response functions. Since in ATLAS the momentum scale of the Inner Detector is determined by the magnetic field that has been measured very precisely [46], the relative scale can be used to transform the momentum scale into the absolute energy scale of the electromagnetic calorimeter.

For each beam momentum p_{beam} the intercalibration is done in the following steps:

1. Derive parameterizations for the E/p_{beam} and p_{beam}/p distributions. For this step, the knowledge of the beam momentum is necessary.

2. E/p is modeled by convoluting E/p_{beam} and p_{beam}/p. This can be done by treating E/p_{beam} and p_{beam}/p as independent random variables or by taking their correlation into account. The knowledge of the beam momentum is used for the description of the correlation. It has been shown that for ATLAS, where single momentum datasets will not be available, the correlations for the corresponding p_T distributions can be extracted using Monte Carlo simulations and successfully applied to data [47].

3. The parameterization for E/p is fitted to the observed E/p distribution. All parameters except a relative scale parameter are kept fixed to their values obtained in step 1.

The modeling of the E/p distribution is described in section 7.1. The details of the relative scale extraction procedure are described in section 7.2 and results for combined test beam data and Monte Carlo simulation are shown in section 7.4.

7.1 Modeling the detector response functions

One way of modeling the E/p_{beam} distribution is to parameterize the energy loss in front of the calorimeter and fold it with a generic Gaussian detector resolution. One can make the following

2010 JINST 5 P11006

exponential ansatz to model the beam energy minus the energy lost upstream of the calorimeter normalized to the beam energy

$$f_e(\varepsilon;\tau_E,E_0) := \frac{1}{\tau_E E_0\,(e^{\tau_E}-1)} e^{\frac{\varepsilon}{\tau_E E_0}}, \varepsilon < E_0 \tag{7.1}$$

where E_0 is a scale parameter and τ_E describes the tail towards lower energies.

Next the generic detector resolution (without upstream material) can be modeled with a Gaussian with standard deviation σ_E:

$$D(x;\sigma_E) := \frac{1}{\sqrt{2\pi}\sigma_E} e^{\frac{-x^2}{2\sigma_E^2}} \tag{7.2}$$

Convoluting eq. (7.1) and eq. (7.2) to get the energy response of the calorimeter leads to

$$\begin{aligned} E(\varepsilon;\tau_E,E_0,\sigma_E) = & \int_0^{E_0} f_e(x;\tau_E,E_0)\, D(\varepsilon-x;\sigma_E)\, dx \\ = & \frac{e^{\frac{2\varepsilon E_0\tau_E+\sigma_E^2}{2{E_0}^2{\tau_E}^2}} \left(\mathrm{Erf}\left[\frac{\varepsilon E_0\tau_E+{\sigma_E}^2}{\sqrt{2}E_0\tau_E\sigma_E}\right]-\mathrm{Erf}\left[\frac{\varepsilon E_0\tau_E-{E_0}^2\tau_E+{\sigma_E}^2}{\sqrt{2}E_0\tau_E\sigma_E}\right]\right)}{2\left(e^{\frac{1}{\tau_E}}-1\right)E_0\tau_E}, \end{aligned} \tag{7.3}$$

where $\mathrm{Erf}(x)$ denotes the Gaussian error function defined by

$$\mathrm{Erf}(x) = \int_0^x e^{-t^2}\, dt. \tag{7.4}$$

The parameters τ_E, E_0, σ_E depend on the beam momentum p_{beam} and denote the tail, the scale and the width of the distribution. The position of the peak of the distribution $E(\varepsilon;\tau_E,E_0,\sigma_E)$, denoted μ_e is a function of the parameters τ_E, E_0, σ_E, i.e. $\mu_e = \mu_e(\tau_E,E_0,\sigma_E)$.

This parameterization is capable of describing the effect of additional material in front of the electromagnetic calorimeter. Since additional material should not affect the intrinsic detector resolution, only the parameter τ_E should change. For a beam momentum of 20 GeV/c additional material equivalent to 10% of a radiation length was placed between the Pixel detector and the SCT and additional 20% between the SCT and the TRT. The E/p_{beam} distribution without (solid line) and with (dashed line) this additional material in the Inner Detector is shown in figure 39 together with the corresponding fits with the convolution model. The obtained parameters are given in table 9. The two values of E_0 (with and without additional material) are compatible within the error bars, whereas μ_e is as expected slightly lower for the run with additional material. There is some correlation between the resolution σ_E and the tail parameter τ_E. The difference of the resolution σ_E for the different material description is of the order of 3 standard deviations, but the tail parameter τ_E is approximately 7.5 standard deviations larger for the geometry description with additional material demonstrating the sensitivity of this parameter to additional material in front of the electromagnetic calorimeter. It has been shown in Monte Carlo simulations for the ATLAS detector that the tail parameter τ_E can be extracted from the E/p distribution [47].

Although the convolution model describes the E/p_{beam} distributions at $p_{beam} = 20$ GeV/c very well, the Crystal Ball model presented below describes the E/p_{beam} distributions far better at beam

2010 JINST 5 P11006

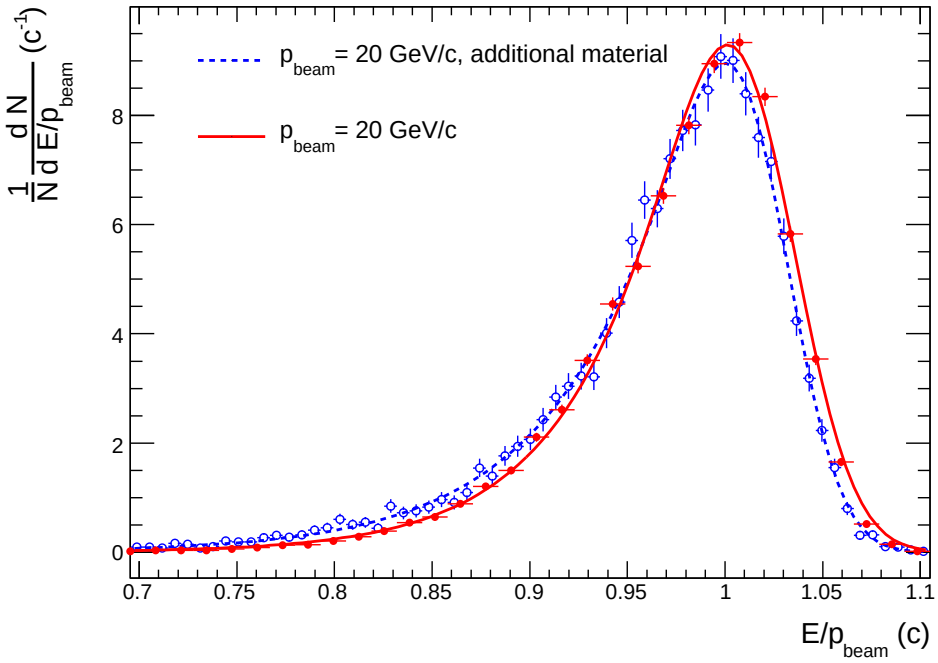

Figure 39. The E/p_{beam} distribution for a beam momentum of $p_{beam} = 20$ GeV/c fitted with the convolution model (equation (7.3)) without (solid line) and with (dashed line) additional material in the Inner Detector.

Table 9. The parameter values for the convolution model (eq. (7.3)) obtained from a fit to the E/p_{beam} distribution for a beam momentum of $p_{beam} = 20$ GeV/c without (*nominal*) and with additional material in the Inner Detector.

material	τ_E (10^{-2})	σ_E (10^{-2})	E_0	$\mu_e(\tau_E, E_0, \sigma_E)$
nominal	4.84(6)	2.66(7)	1.0275(4)	1.0013(5)
additional	5.78(11)	2.32(9)	1.0267(7)	1.0003(7)

momenta above 20 GeV/c. The Crystal Ball model is therefore used for the combined test beam 2004 for E/p_{beam} distributions for the sake of consistency (see figure 21).

The Crystal Ball function [48], named after the Crystal Ball Collaboration, is a probability density function commonly used to model various processes in high energy physics. It consists of a Gaussian core part and a power-law low-end tail below a certain threshold. These two parts are spliced together (via the coefficients A and B) in such a way that the function and its first derivative are both continuous. The Crystal Ball function f_{CB} is given by

$$f_{CB}(x;\alpha,n,\mu,\sigma) = N \cdot \begin{cases} \exp(-\frac{(x-\mu)^2}{2\sigma^2}) & \text{for } \frac{x-\mu}{\sigma} > -\alpha \\ A \cdot (B - \frac{x-\mu}{\sigma})^{-n} & \text{for } \frac{x-\mu}{\sigma} \leq -\alpha \end{cases} \tag{7.5}$$

2010 JINST 5 P11006

where

$$A = \left(\frac{n}{|\alpha|}\right)^n \cdot \exp\left(-\frac{|\alpha|^2}{2}\right)$$
$$B = \frac{n}{|\alpha|} - |\alpha| \,. \tag{7.6}$$

N is a normalization factor and α, n, μ and σ are parameters.

The model for the E/p_{beam} distribution, denoted $E(\varepsilon;\alpha_\varepsilon,n_\varepsilon,\mu_\varepsilon,\sigma_\varepsilon)$, is given by

$$E(\varepsilon;\alpha_\varepsilon,n_\varepsilon,\mu_\varepsilon,\sigma_\varepsilon) = c\, f_{CB}(\varepsilon;\alpha_\varepsilon,n_\varepsilon,\mu_\varepsilon\sigma_\varepsilon), \tag{7.7}$$

where $\varepsilon = E/p_{beam}$. The parameters $\alpha_\varepsilon, n_\varepsilon, \mu_\varepsilon, \sigma_\varepsilon$ depend on the beam momentum p_{beam}.

The p_{beam}/p distribution also is modeled using a Crystal Ball function that is mirrored at $x = \mu$ which is

$$f_{mirror}(x;\alpha,n,\mu,\sigma) = f_{CB}(\mu-(x-\mu);\alpha,n,\mu,\sigma) = f_{CB}(2\mu-x;\alpha,n,\mu,\sigma) \tag{7.8}$$

with the Crystal Ball function defined in eq. (7.5) and eq. (7.6).

The model for the p_{beam}/p distribution, denoted $Q(q;\alpha_q,n_q,\mu_q,\sigma_q)$, is given by

$$Q(q;\alpha_q,n_q,\mu_q,\sigma_q) = f_{mirror}(q;\alpha_q,n_q,\mu_q,\sigma_q), \tag{7.9}$$

where $q = p_{beam}/p$.

Treating the measurement variables ε and q as random variables, the distribution R of the product $r = \varepsilon \cdot q$, which describes the ratio E/p, is given by

$$R(r) = \int_{-\infty}^{\infty} f_{(E,Q)}\left(\frac{r}{w}, w\right)\frac{1}{w}\, dw, \tag{7.10}$$

where $f_{(E,Q)}(\varepsilon,q)$ denotes the joint distribution of ε and q. Using the parameterizations $E(\varepsilon;\alpha_\varepsilon,n_\varepsilon,\mu_\varepsilon,\sigma_\varepsilon)$ and $Q(q;\alpha_q,n_q,\mu_q,\sigma_q)$ for ε (eq. (7.7)) and q (eq. (7.9)) and the fact that $E(\varepsilon)$ and $Q(q)$ are always positive, the joint distribution can be rewritten as

$$f_{(E,Q)}(\varepsilon,q;\alpha_\varepsilon,n_\varepsilon,\mu_\varepsilon,\sigma_\varepsilon,\alpha_q,n_q,\mu_q,\sigma_q) = E(\varepsilon;\alpha_\varepsilon,n_\varepsilon,\mu_\varepsilon,\sigma_\varepsilon)\cdot Q(q;\alpha_q,n_q,\mu_q,\sigma_q)\cdot C(\varepsilon,q), \tag{7.11}$$

where $C(\varepsilon,q)$ describes the correlation between ε and q. No correlation would be equivalent to $C(\varepsilon,q) = 1$. Inserting eq. (7.11) into eq. (7.10) leads to

$$R(r;\alpha_\varepsilon,n_\varepsilon,\mu_\varepsilon,\sigma_\varepsilon,\alpha_q,n_q,\mu_q,\sigma_q) = \int_{-\infty}^{\infty} E(\frac{r}{w};\alpha_\varepsilon,n_\varepsilon,\mu_\varepsilon,\sigma_\varepsilon)\, Q(w;\alpha_q,n_q,\mu_q,\sigma_q) C(\frac{r}{w},w)\frac{1}{w}\, dw \tag{7.12}$$

Two ways of dealing with the correlation between ε and q are considered in the following.

No correlation. It is assumed that there is no correlation between ε and q, i.e. ε and q are independent random variables. For the modeling this means $C(\varepsilon,q) = 1$ in equation (7.12). This should be the case for high energy electrons where the impact of bremsstrahlung on the momentum measurement is small. Later it will be shown that the correlation between ε and q has to be taken into account in order to achieve a precision for the relative scale at the 0.5% level.

2010 JINST 5 P11006

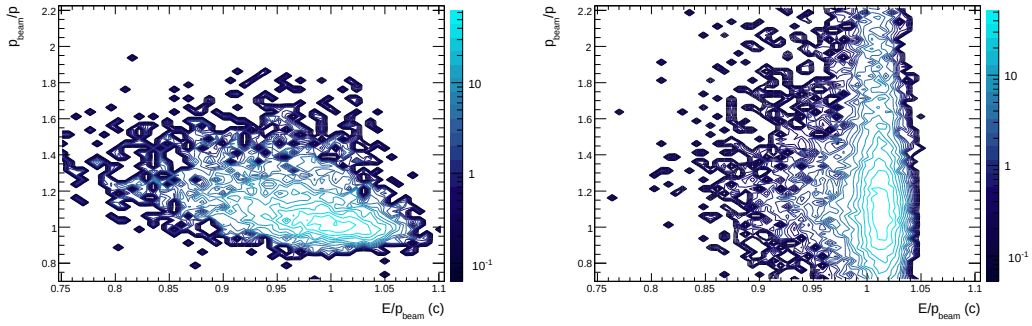

(a) $p_{beam} = 20$ GeV/c (b) $p_{beam} = 100$ GeV/c

Figure 40. The joint distribution $f_{(E,Q)}(\varepsilon, q)$ (eq. (7.10)) for CTB data for $p_{beam} = 20$ GeV/c and $p_{beam} = 100$ GeV/c.

Correlation obtained from Monte Carlo simulation. The continous function $C(\varepsilon, q)$ in eq. (7.11) can be approximated by discrete values for bins in ε and q. $C(\varepsilon, q)$ is determined from Monte Carlo simulations by performing the division

$$C(\varepsilon, q) = \frac{f_{(E,Q)}(\varepsilon, q)}{E(\varepsilon)\, Q(q)} \tag{7.13}$$

bin-wise. In order to be able to compute $C(\varepsilon, q)$ the knowledge of the beam momentum is necessary, but since the computation is performed bin-wise it is independent of the choice of the parameterizations for $E(\varepsilon)$ and $Q(q)$.

The joint distributions $f_{(E,Q)}(\varepsilon, q)$ of ε and q for CTB data are shown for $p_{beam} = 20$ GeV/c and for $p_{beam} = 100$ GeV/c in figure 40, the correlation function $C(\varepsilon, q)$ extracted from Monte Carlo simulations together with its projection onto the E/p_{beam} axis for $p_{beam} = 20$ GeV/c in figure 41 and for $p_{beam} = 100$ GeV/c in figure 42. For $p_{beam} = 20$ GeV/c the correlation factor $C(\varepsilon, q)$ derived from Monte Carlo simulation shows a gradient in the upper-left direction in the parameter space resulting in a slope in the projection onto the E/p_{beam} axis in figure 41(a). This gradient becomes smaller for $p_{beam} = 50$ GeV/c and vanishes for $p_{beam} = 80$ GeV/c and $p_{beam} = 100$ GeV/c making the projection onto the E/p_{beam} axis in figure 42(a) constant within errors.

7.2 Scale factor extraction procedure

This procedure is applied for each beam momentum p_{beam} separately. The parameters $\hat{\alpha}_\varepsilon, \hat{n}_\varepsilon, \hat{\mu}_\varepsilon, \hat{\sigma}_\varepsilon$ are obtained by fitting the Crystal Ball parameterization $E(\varepsilon; \alpha_\varepsilon, n_\varepsilon, \mu_\varepsilon, \sigma_\varepsilon)$ (eq. (7.7)) to the E/p_{beam} distribution. The parameters $\hat{\alpha}_q, \hat{n}_q, \hat{\mu}_q, \hat{\sigma}_q$ are computed by fitting the mirror Crystal Ball parameterization $Q(q; \alpha_q, n_q, \mu_q, \sigma_q)$ (eq. (7.9)) to the p_{beam}/p distribution. Then the scale parameter $\bar{\mu}_\varepsilon$ for the E/p_{beam} distribution is calculated by fitting $R(r; \hat{\alpha}_\varepsilon, \hat{n}_\varepsilon, \bar{\mu}_\varepsilon, \hat{\sigma}_\varepsilon, \hat{\alpha}_q, \hat{n}_q, \hat{\mu}_q, \hat{\sigma}_q)$ (eq. (7.12)) to the E/p distribution. In this fit only the $\bar{\mu}_\varepsilon$ parameter is allowed to vary. The other parameters $\hat{\alpha}_\varepsilon, \hat{n}_\varepsilon, \hat{\sigma}_\varepsilon, \hat{\alpha}_q, \hat{n}_q, \hat{\mu}_q, \hat{\sigma}_q$ are fixed to the values obtained by the E/p_{beam} and p_{beam}/p fits, respectively. The relative scale factor is then defined by the ratio $\bar{\mu}_\varepsilon/\hat{\mu}_\varepsilon$.

2010 JINST 5 P11006

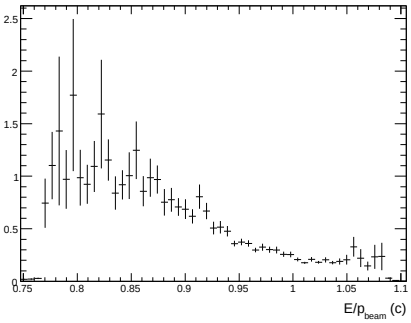

(a) Projection of $C(\varepsilon,q)$ for $p_{beam} = 20$ GeV/c

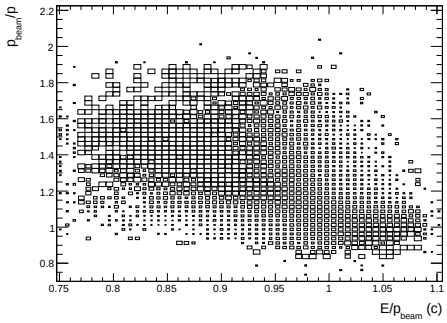

(b) $C(\varepsilon,q)$ for $p_{beam} = 20$ GeV/c

Figure 41. Correlation factor $C(\varepsilon,q)$ (eq. (7.13)) derived from Monte Carlo simulation (41(b)) and its projection onto the E/p_{beam} axis (41(a)) for $p_{beam} = 20$ GeV/c.

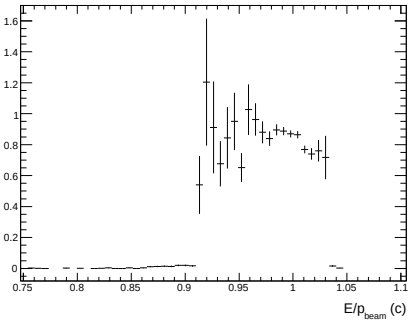

(a) Projection of $C(\varepsilon,q)$ for $p_{beam} = 100$ GeV/c

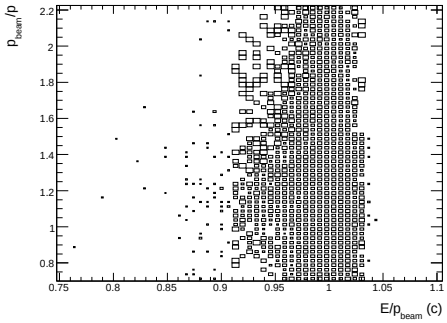

(b) $C(\varepsilon,q)$ for $p_{beam} = 100$ GeV/c

Figure 42. Correlation factor $C(\varepsilon,q)$ (eq. (7.13)) derived from Monte Carlo simulation (42(b)) and its projection onto the E/p_{beam} axis (42(a)) for $p_{beam} = 100$ GeV/c.

This procedure is based on the assumption that the relative scale factor is close to 1 and therefore the effect of the scaling of the parameters $\hat{\alpha}_\varepsilon, \hat{n}_\varepsilon, \hat{\sigma}_\varepsilon$ is negligible. Otherwise they would have to be scaled accordingly.

7.3 Estimation of systematic errors

The procedure to extract the relative scale factor between the energy scale of the electromagnetic calorimeter and the momentum scale of the inner detector has been validated using a dedicated Monte Carlo simulation. The systematic error due to the scale extraction procedure is found to be below 1 permil [47].

7.4 Results

The E/p_{beam} distribution with the fitted $E(\varepsilon;\hat{\alpha}_\varepsilon,\hat{n}_\varepsilon,\hat{\mu}_\varepsilon,\hat{\sigma}_\varepsilon)$ model, the p_{beam}/p distribution with the fitted $Q(q;\hat{\alpha}_q,\hat{n}_q,\hat{\mu}_q,\hat{\sigma}_q)$ model and the E/p_{beam} distribution fitted with

2010 JINST 5 P11006

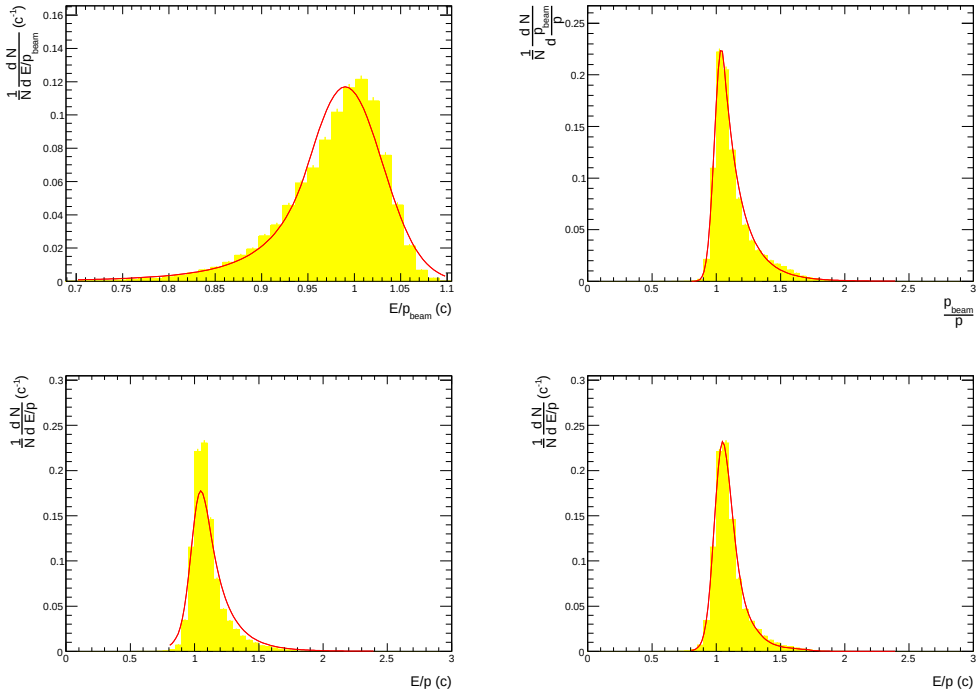

Figure 43. Monte Carlo simulation: The E/p_{beam} distribution with the fitted $E(\varepsilon;\hat{\alpha}_\varepsilon,\hat{n}_\varepsilon,\hat{\mu}_\varepsilon,\hat{\sigma}_\varepsilon)$ model (top left), the p_{beam}/p distribution with the fitted $Q(q;\hat{\alpha}_q,\hat{n}_q,\hat{\mu}_q,\hat{\sigma}_q)$ model (top right) and the E/p distribution fitted with $R(r;\hat{\alpha}_\varepsilon,\hat{n}_\varepsilon,\bar{\mu}_\varepsilon,\hat{\sigma}_\varepsilon,\hat{\alpha}_q,\hat{n}_q,\hat{\mu}_q,\hat{\sigma}_q)$ without (bottom left) and with (bottom right) Monte Carlo simulation correlation modeling for Monte Carlo simulation for $p_{beam} = 20$ GeV/c.

$R(r;\hat{\alpha}_\varepsilon,\hat{n}_\varepsilon,\bar{\mu}_\varepsilon,\hat{\sigma}_\varepsilon,\hat{\alpha}_q,\hat{n}_q,\hat{\mu}_q,\hat{\sigma}_q)$ without and with Monte Carlo simulation correlation modeling are shown in figure 43 (Monte Carlo simulation) and figure 44 (data) for p_{beam}=20 GeV/c. The number of events after all cuts is given in table 1.

Figures 43 and 44 show that for $p_{beam} = 20$ GeV/c the modeling of the correlation between ε and q is needed to improve the description of the shape of the E/p distributions. The E/p distribution for data for $p_{beam} = 20$ GeV/c is not perfectly described by applying the correlation obtained from the Monte Carlo simulation implying that the correlation is larger in data than in the Monte Carlo simulation.

The relative scale factor $\bar{\mu}_\varepsilon/\hat{\mu}_\varepsilon$ without and with Monte Carlo simulation correlation modeling is shown in figure 45 for all beam momenta. A value of 1 is expected for all beam momenta. For $p_{beam} = 80$ GeV/c and higher the modeling of the correlation between ε and q does not improve the relative scale factor. For $p_{beam} = 50$ GeV/c and specially for $p_{beam} = 20$ GeV/c the modeling of the correlation between ε and q brings the relative scale factor down to the 2 respectively 5 permill level. Within the available statistics, the uncertainties on the relative scale factor are comparable with the expectation from the dedicated validation Monte Carlo simulation model.

This demonstrates that for the CTB 2004 a Monte Carlo simulation correlation modeling can be used to extract the relative scale factor $\bar{\mu}_\varepsilon/\hat{\mu}_\varepsilon$ from the data and therefore a similar approach

2010 JINST 5 P11006

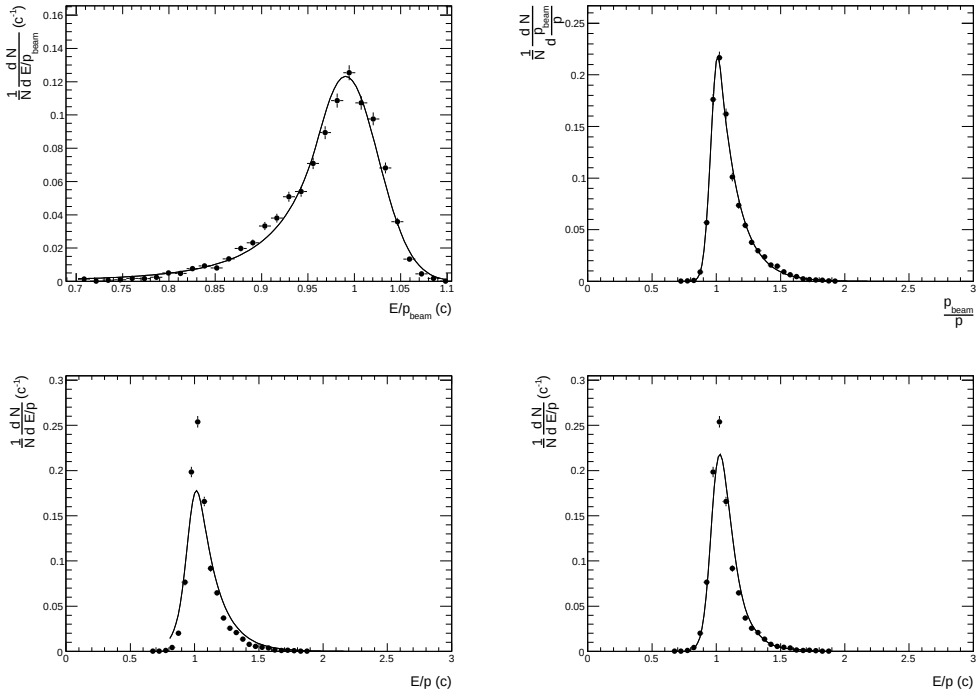

Figure 44. CTB data: The E/p_{beam} distribution with the fitted $E(\varepsilon;\hat{\alpha}_\varepsilon,\hat{n}_\varepsilon,\hat{\mu}_\varepsilon,\hat{\sigma}_\varepsilon)$ model (top left), the p_{beam}/p distribution with the fitted $Q(q;\hat{\alpha}_q,\hat{n}_q,\hat{\mu}_q,\hat{\sigma}_q)$ model (top right) and the E/p distribution fitted with $R(r;\hat{\alpha}_\varepsilon,\hat{n}_\varepsilon,\bar{\mu}_\varepsilon,\hat{\sigma}_\varepsilon,\hat{\alpha}_q,\hat{n}_q,\hat{\mu}_q,\hat{\sigma}_q)$ without (bottom left) and with (bottom right) Monte Carlo simulation correlation modeling for CTB data for $p_{beam} = 20$ GeV/c.

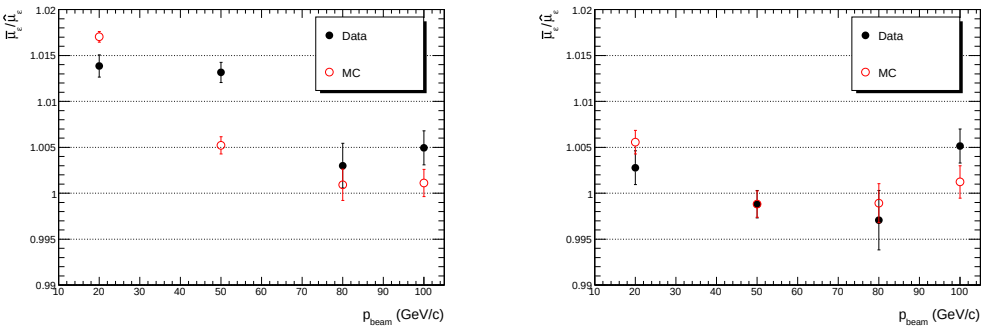

(a) without correlation (b) with correlation

Figure 45. The relative scale factor $\bar{\mu}_\varepsilon/\hat{\mu}_\varepsilon$ extracted from the E/p distributions without (figure 45(a)) and with (figure 45(b)) correlation weighting for Monte Carlo simulation and data for all beam momenta.

will be used for ATLAS. The description of the correlation should be easier for ATLAS since the material distribution upstream of the electromagnetic calorimeter is much better understood for ATLAS than for the CTB 2004 due to the presence of the far upstream material at the CTB 2004.

2010 JINST 5 P11006

8 Conclusions

The combined performance for electrons of a barrel segment of the ATLAS detector has been evaluated in the 2004 combined test-beam in conditions close to those expected in ATLAS. Read-out electronics and data acquisition were early versions of those used in ATLAS.

It has been shown that the Monte Carlo simulation describes well all important distributions of measured variables for the Inner Detector and the LAr calorimeter with the presence of a magnetic field in the Inner Detector.

The calibration of the energy measurement for electrons with the presence of a magnetic field has been investigated and the differences with respect to the calibration without magnetic field have been analyzed. The parameterization of the energy deposit in the calorimeter as a function of the shower depth cannot be used at the 2004 combined test-beam due to the larger out-of-cluster energy deposits at lower beam momenta which stem from the larger distances between the Inner Detector and the calorimeter set-up. The linearity obtained is 0.28% for the momentum range of 20 to 100 GeV/c which is within the estimated systematic uncertainties coming from statistics and from the beam energies. The stochastic term of the energy resolution is $(10.0 \pm 0.1)\%$ GeV$^{1/2}$, with an average electronic noise term of about 208 MeV. This is compatible with previous test beam results without magnetic field and fulfills the physics requirements for the ATLAS LAr calorimeter. The 2004 combined test-beam showed that the calibration procedure of the ATLAS electromagnetic calorimeter for electrons works as expected in very realistic conditions.

A probability based approach for the particle identification with the Transition Radiation Tracker has been applied for both High Threshold (HT) hits and Time-over-Threshold (ToT) information. For HT information, the probability based particle identification gives a pion rejection factor of 9 to 40 depending on the particle momentum at 90% electron efficiency. This is an improvement of 13% to 30% compared to using only the number of HT hits as separation criteria. Furthermore, including the ToT information increases the rejection power to 25 to 70, mostly at low momenta as expected. In addition, the onset of transition radiation has been measured in a data-driven way using the variety of momenta and particle types at the 2004 combined test-beam which is crucial for tuning the Monte Carlo simulation of the transition radiation.

The bremsstrahlung recovery algorithm using the calorimeter has been investigated using Monte Carlo simulation for the 2004 combined test-beam setup. It has been demonstrated that the correction algorithm is able to recover the initial electron momentum, even in extreme situations where the photon and electron clusters are reconstructed separately in the calorimeter, by removing the bremsstrahlung tail in the $1/p_{\mathrm{T}}$ distribution. A detailed comparison of performance with 2004 combined test-beam data shows an agreement with the Monte Carlo simulation at the level of 1–2%.

It has been demonstrated that the E/p parameterization based on a Monte Carlo simulation correlation modeling can be used to extract the electromagnetic scale from data with a precision of better than 0.5% with the available statistics.

These combined performance studies at the 2004 combined test-beam give strong evidence that the performance of the ATLAS detector for electrons will be within the requirements imposed by the ATLAS physics program.

2010 JINST 5 P11006

Acknowledgments

We are grateful to our colleagues from the accelerator department for the support in running the H8 beam line. We are indebted to our technicians and engineers for their contribution to the construction, testing and the operation of the detector modules, cooling systems and electronics. Those of us from non-member states wish to thank CERN for its hospitality.

References

[1] G. Aad et al., *ATLAS pixel detector electronics and sensors*, 2008 *JINST* **3** P07007.

[2] A. Abdesselam et al., *The barrel modules of the ATLAS semiconductor tracker*, *Nucl. Instrum. Meth.* **A 568** (2006) 642.

[3] ATLAS TRT collaboration, E. Abat et al., *The ATLAS TRT barrel detector*, 2008 *JINST* **3** P02014.

[4] T. Ludlam et al., *Particle identification by electron cluster detection of transition radiation photons*, *Nucl. Instrum. Meth.* **180** (1981) 413.

[5] V.A. Polychronakos et al., *Integrated High-Rate Transition Radiation Detector and Tracking Chamber for the LHC*, CERN-DRDC-90-38.DRDC/P8 (1990).

[6] RD3 collaboration, B. Aubert et al., *Performance of a liquid argon electromagnetic calorimeter with an 'accordion' geometry*, *Nucl. Instrum. Meth.* **A 309** (1991) 438.

[7] The ATLAS collaboration, *ATLAS Technical Proposal for a General-Purpose pp Experiment at the Large Hadron Collider at CERN*, Technical Report CERN-LHCC-94-43 (1994).

[8] ATLAS collaboration, G. Aad et al., *The ATLAS Experiment at the CERN Large Hadron Collider*, 2008 *JINST* **3** S08003.

[9] R. Wigmans, *Calorimetry*, Oxford University Press, Oxford U.K. (2000).

[10] The ATLAS collaboration, *Liquid Argon Calorimeter Technical Design Report*, Technical Report CERN-LHCC-96-041 (1996).

[11] The ATLAS collaboration, *Calorimeter Performance Technical Design Report*, Technical Report CERN-LHCC-96-040 (1996).

[12] ATLAS Electromagnetic Barrel Calorimeter collaboration, M. Aharrouche et al., *Energy linearity and resolution of the ATLAS electromagnetic barrel calorimeter in an electron test- beam*, *Nucl. Instrum. Meth.* **A 568** (2006) 601.

[13] J. Colas et al., *Response Uniformity of the ATLAS Liquid Argon Electromagnetic Calorimeter*, *Nucl. Instrum. Meth.* **A 582** (2007) 429.

[14] M. Aharrouche et al., *Measurement of the response of the ATLAS liquid argon barrel calorimeter to electrons at the 2004 combined test- beam*, *Nucl. Instrum. Meth.* **A 614** (2010) 400.

[15] B. Di Girolamo et al. *Beamline instrumentation in the 2004 combined ATLAS testbeam*, *ATLAS Internal Note*, ATLAS-TECH-PUB-2005-001 (2005).

[16] ATLAS Electromagnetic Barrel Liquid Argon Calorimeter Group collaboration, B. Aubert et al., *Construction, assembly and tests of the ATLAS electromagnetic barrel calorimeter*, *Nucl. Instrum. Meth.* **A 558** (2006) 388.

[17] J. Abdallah et al. *Design, Construction and Installation of the ATLAS Hadronic Barrel Scintillator-Tile Calorimeter*, ATL-TILECAL-PUB-2008-001 (2008).

2010 JINST 5 P11006

[18] F. Bauer et al., *Large-scale production of monitored drift tube chambers for the ATLAS muon spectrometer*, *Nucl. Instrum. Meth.* **A 518** (2004) 69.

[19] A. Ahmad et al., *Alignment of the Pixel and SCT Modules for the 2004 ATLAS Combined Test Beam*, 2008 *JINST* **3** P09004.

[20] N.J. Buchanan et al., *ATLAS liquid argon calorimeter front end electronics*, 2008 *JINST* **3** P09003.

[21] J. Colas et al., *Electronics calibration board for the ATLAS liquid argon calorimeters*, *Nucl. Instrum. Meth.* **A 593** (2008) 269.

[22] A. Artamonov et al., *The ATLAS forward calorimeters*, 2008 *JINST* **3** P02010.

[23] LIQUID ARGON BACK END ELECTRONICS collaboration, A. Bazan et al., *ATLAS liquid argon calorimeter back end electronics*, 2007 *JINST* **2** P06002.

[24] M. Aleksa et al., *ATLAS Combined Testbeam: computation and validation of the electronic calibration constants for the electromagnetic calorimeter*, *ATLAS Internal Note*, ATL-LARG-PUB-2006-003 (2006).

[25] S. Gadomski et al., *Deployment and use of the ATLAS DAQ in the combined test beam*, *IEEE Trans. Nucl. Sci.* **53** (2006) 2156.

[26] The ATLAS collaboration, *ATLAS Computing TDR*, Technical Report CERN-LHCC-2005-022 (2005).

[27] W.E. Cleland and E.G. Stern, *Signal processing considerations for liquid ionization calorimeter in a high rate environment*, *Nucl. Instrum. Meth.* **A 338** (1994) 467.

[28] D. Banfi, M. Delmastro and M. Fanti, *Cell response equalisation of the ATLAS electromagnetic calorimeter without the direct knowledge of the ionisation signals*, 2006 *JINST* **1** P08001.

[29] L. Neukermans, P.Perrodo and R. Zitoun, *Understanding the electromagnetic barrel pulse shapes and the absolute electronic calibration*, ATLAS Internal Note ATL-LARG-2001-008 (2001).

[30] M. Citterio, M. Delmastro and M. Fanti, *A study of the electrical properties and of the signal shapes in the ATLAS Liquid ARgon Accordion Calorimeter using a hardware model*, *ATLAS Internal Note* ATL-LARG-2001-018 (2001).

[31] D. Prieur, *Using Time Convolution Method to compute Optimal Filtering Coefficients for LARG electromagnetic calorimeter*, ATLAS Internal Note ATL-LARG-2005-001 (2005).

[32] W. Lampl et al. *Calorimeter Clustering Algorithms: Description and Performance*, Technical Report ATL-LARG-PUB-2008-002, ATL-COM-LARG-2008-003 (2008).

[33] GEANT4 collaboration, S. Agostinelli et al., *GEANT4: a simulation toolkit*, *Nucl. Instrum. Meth.* **A 506** (2003) 250.

[34] B. Di Girolamo, M. Gallas and T. Koffas, *2004 ATLAS Barrel Combined Test Beam Layout*, *ATLAS EDMS Note*, ATC-TT-IN-0001 (2005).

[35] F. Hubaut, B. Laforge, D. Lacour, F. Orsini, *Test beam Measurement of the Cross-talk in the EM Barrel Module 0*, ATLAS Internal Note ATL-LARG-2000-007 (2000).

[36] F. Hubaut, *Crosstalk Measurements in the EM Barrel Module 0 from 99', May 00' and July 00' Beam Tests*, ATLAS Internal Note ATL-LARG-2000-009 (2000).

[37] M. Boonekamp, Private communication.

[38] M. Delmastro, M. Aleksa, T. Carli, R. Froeschl, I. Wingerter-Seez, *Response of the ATLAS Liquid Argon Electromagnetic Barrel Calorimeter to Very Low Energy Electrons at the 2004 ATLAS Combined Test-Beam*, ATLAS Internal Note ATL-COM-LARG-2009-014 (2009).

2010 JINST 5 P11006

[39] W. Lampl, *Optimizing the Energy Measurement of the ATLAS Electromagnetic Calorimeter*, PhD thesis, Vienna University of Technology (2006) CERN-THESIS-2006-002, Presented on 18 Jan 2006

[40] D. Banfi, L. Carminati and L. Mandelli, *Calibration of the ATLAS electromagnetic calorimeter using calibration hits*, ATLAS Note ATL-LARG-PUB-2007-012 (2007).

[41] T.G. Cornelissen et al., *Track Fitting in the ATLAS Experiment*, PhD thesis, Univ. Amsterdam (2006) CERN-THESIS-2006-072, Presented on 12 Dec 2006.

[42] T. Koffas and T. Vu Anh, Private communication.

[43] A Wald and J Wolfowitz, *On a test whether two samples are from the same population*, *Ann. Math Statist.* **11** (1940) 147.

[44] V Kartvelishvili, *Electron bremstrahlung recovery in ATLAS tracking using Dynamic Noise Adjustment*, PoS(ACAT)046.

[45] T Atkinson, *Reconstruction of electrons with the Gaussian-Sum filter in the ATLAS Inner Detector*, *52nd IEEE Nuclear Science Symposium and Medical Imaging Conference*, pages 148–152 (2005).

[46] M. Aleksa et al., *Measurement of the ATLAS solenoid magnetic field*, 2008 *JINST* **3** P04003.

[47] R. Froeschl, *Calibrating the CERN ATLAS Experiment with E/p*, CERN-THESIS-2010-007 PhD thesis, Vienna Tech. University (2009), Presented on 14 Oct 2009.

[48] J.E. Gaiser, *Charmonium Spectroscopy from Radiative Decays of the J/ψ and ψ'*, PhD thesis, SLAC-R-255 (1982), the Crystal Ball function is defined in appendix F, p.178.

2010 JINST 5 P11006